Dynamic Behaviour of Transformer Winding under Short-Circuits

Muhammad Salman Aslam Minhas

A thesis submitted to the Faculty of Engineering, University of the Witwatersrand, Johannesburg, in fulfilment of the requirements for the degree of Doctor of Philosophy.

Johannesburg, November 2007

Declaration

I declare that this thesis is my own, unaided work, except where otherwise acknowledged. It is being submitted for the degree of Doctor of Philosophy in the University of the Witwatersrand, Johannesburg. It has not been submitted before for any degree or examination in any other university.

Signed this ___ day of __________ 20___

____

Muhammad Salman Aslam Minhas.

Abstract

The work presented extends and contributes to the understanding of the dynamic behaviour of large power transformer windings under short circuits. A simple yet accurate method of prediction of electromagnetic forces is developed and used as input to the dynamic mechanical model. This work also explores non-linearity of the pressboard material under dynamic loading and successfully models it to compute characteristics like stress-strain and damping. The results of pressboard model are used in the final model of a full transformer and the simulated predictions compare very favourably with actual measurements. The model proves that for small radial movements, the axial and radial behaviours are independent of each other.

Acknowledgements

A very special thank you to Prof J P Reynders for all his kindness, patience, support and guidance.

An unforgettable thank you to Prof R Iwankiewicz for his guidance and support.

Thank you to Mr Wessel Benecke and Rotek Engineering for supplying the test transformer.

Thank you to Mr Harry Fellows for his support from the workshop in making all the components for the experimental work.

To my dad who raised me to be what I am, who guided and supported me in all my endeavours. To my mum for her unforgettable and unselfish sacrifice to put me through university. To my wife for her ongoing support...

To the Almighty, without whom all the above would just be a passing breeze.

Contents

Declaration **i**

Abstract **ii**

Acknowledgements **iii**

Contents **v**

List of Figures **xi**

List of Tables **xvii**

List of Symbols **xviii**

1 Introduction **1**

2 Electromagnetic forces in transformer windings **4**

2.1 Introduction 4

2.2 Electromagnetic force on a conductor in a magnetic field 5

2.3 Magnetic field in a two-winding transformer 5

2.4 Axial electromagnetic forces 7

2.5 Radial electromagnetic forces 7

3 Prediction of axial electromagnetic forces **9**

3.1 Introduction 9

3.2 Calculation of the axial force 9

3.3 Empirical or approximate methods 10

3.3.1 Indirect measurement of axial force 10

3.3.2 Residual ampere-turn method 15

3.4 Two-dimensional methods 19

3.4.1 Two-dimensional method of images 22

3.4.2 Two-dimensional graphical image method 23

3.5 Calculation using Fourier series 23

3.6 Methods using digital computers 25

3.6.1 Smythe's solution 26

3.6.2 Rabin's Solution 27

3.6.3 Solution by analogue computer 27

3.6.4 Image method with discrete conductors 27

3.6.5 Finite element method (FEM) 30

3.7 Discussion 33

3.8 Conclusion 33

4 Calculation of radial electromagnetic forces in concentric windings **34**

4.1 Introduction 34

4.2 Prediction of radial electromagnetic forces 34

4.3 Elementary methods to calculate radial electromagnetic forces 35

4.4 Forces in the outer winding . . . 36

4.4.1 Hoop stress in disk windings . . . 38

4.5 Forces on the inner winding . . . 38

4.6 Discussion . . . 39

4.7 Conclusion . . . 40

5 Dynamic axial behaviour of transformer windings 41

5.1 Introduction . . . 41

5.2 Axial model of power transformer windings . . . 42

5.3 Dynamic axial model . . . 43

5.4 Implementation of model . . . 47

5.5 Conclusion . . . 48

6 Dynamic radial behaviour of transformer windings 49

6.1 Introduction . . . 49

6.2 Radial behaviour of windings . . . 49

6.3 Radial model of a two-winding transformer . . . 50

6.4 Kinetic energy of inner and outer disks . . . 54

6.5 Strain (potential) energy . . . 59

6.5.1 Potential energy of copper rings . . . 59

6.5.2 Potential energy (PE) stored in pressboard ribs (radial spacers) 62

6.6 Generalized forces in radial direction . . . 67

6.7 Modeling . . . 69

6.8 Conclusion . . . 69

7 Physical properties of pressboard under varying pre-stress 70

7.1 Introduction 70

7.2 Physical properties of transformer board 71

7.3 Dynamic stress-strain test apparatus 71

7.3.1 Displacement and force sensors 72

7.4 Experimental procedure 74

7.5 Results 78

7.5.1 Stress-Strain properties at zero pre-stress 78

7.5.2 Stress-Strain properties at low pre-stress (1.42 N/mm^2) . . . 80

7.5.3 Stress-Strain properties at low to medium pre-stress (4.3 N/mm^2) 81

7.5.4 Stress-Strain properties at medium pre-stress (7.1N/mm^2) . . 82

7.5.5 Stress-Strain properties at medium-high pre-stress (10 N/mm^2) 83

7.5.6 Stress-Strain properties at high pre-stress (14 N/mm^2) 84

7.6 Modeling of experimental set up as spring-mass system 84

7.6.1 Mathematical model 85

7.6.2 Damping 91

7.7 Discussion 92

7.8 Conclusions 93

8 Combined transformer model 94

8.1 Introduction 94

8.2 Components of the model 95

8.2.1 Axial spacers (pressboard) 95

8.2.2 Lumped masses, springs and dashpots 95
8.3 Combined model of a transformer winding 96
8.4 Axial and radial models 96
8.5 Coupled dynamic model 97
8.6 Test transformer 97
8.7 Test setup and procedure 98
8.8 Simulated and measured results 100
8.9 Discussion 105
8.10 Conclusions 108

9 Conclusion and recommendations 109

9.1 Conclusion 109
9.2 Recommendations for further research 110

A Matlab source codes 115

A.1 Input code 115
A.2 Electromagnetic force 121
A.2.1 Smaller routines used in electromagnetic calculation 127
A.3 Code related to axial dynamic behaviour 128
A.4 Code related to radial dynamic behaviour 130
A.4.1 Code used in radial behaviour for position of displacement . . 134

B Simulink models 136

C Test transformer design and dimensions 140

C.1 Test transformer design details 140

List of Figures

2.1 Force exerted on a conductor in magnetic field 5

2.2 Magnetic flux pattern of a two-winding transformer 6

2.3 Axial and radial forces in concentric windings when the windings are axially non-symmetrical 7

2.4 Radial electromagnetic forces in concentric transformer windings with axial symmetry 8

3.1 Method of calculation of radial flux by measurement of volt-per-turn [Waters, 1966] 12

3.2 Axial compression curve for untapped transformer windings [Waters, 1966; Franklin and Franklin, 1983; Waters, 1953] 14

3.3 Determination of residual ampere-turns of winding tapped at top end [Waters, 1966; Franklin and Franklin, 1983] 16

3.4 Arrangement of tappings and resulting residual-ampere-turns 19

3.5 Polar diagram of flux density for the middle limb of a transformer with 10% tapped from the middle of the outer winding [Waters, 1966; Franklin and Franklin, 1983] 20

3.6 Winding representation as infinitely long two-dimensional straight conductor [Waters, 1966; Franklin and Franklin, 1983] 21

3.7 Contiguous winding sections used in axial force calculation and images representing the effect of the core 22

3.8 Two-dimensional representation of transformer windings with images [Waters, 1966] 24

3.9 Idealized core-type transformer with curvature of windings 26

3.10 Discrete image method 28

3.11 System of images in discrete image method for a two-winding transformer 29

3.12 Flow chart of system of the images in discrete image method for a two-winding transformer 31

3.13 Magnetic field in the test transformer under short circuit conditions. 32

3.14 Comparison of results of discrete image method and Finite Element Method for inner winding. 32

3.15 Comparison of results of discrete image method and Finite Element Method for outer winding. 33

4.1 Two-dimension representation of concentric transformer windings for the calculation of radial electromagnetic forces showing axial flux and resulting radial force [Waters, 1966] 35

4.2 Radial electromagnetic forces in concentric transformer windings [Waters, 1966] 36

4.3 Mean hoop stress calculating method [Waters, 1966] 37

4.4 Comparison of results of discrete image method and finite element method for inner winding 40

4.5 Comparison of results of discrete image method and finite element method for outer winding 40

5.1 Physical construction of transformer winding. On the top left, a photo shows the full winding and the right is the magnified section of the winding showing axial spacers. The bottom section of photo shows the duct sticks (ribs). 42

5.2 Lumped mass model of a two-winding transformer 44

5.3 The natural frequencies of test transformer in axial direction 47

6.1 Cross-sectional view of a transformer winding 51

6.2 Radial and circumferential displacements, u and v the inner winding ring. 52

6.3 Simplest mode of vibration 'breathing motion' uniform radial expansion and contraction 52

6.4 Inner and outer winding represented as elastic rings coupled with springs and dashpots 53

6.5 Angular position of core and ribs. The ribs are represented as coupling springs between the core and the inner winding and between the inner and outer winding 63

6.6 The natural frequencies of radial behaviour of test transformer . . . 69

7.1 The picture of the dynamic stress-strain tester 72

7.2 The model of the apparatus used to measure the physical properties of pressboard 73

7.3 Detail drawing of Stress-strain apparatus 75

7.4 Displacement sensor construction 76

7.5 Force sensor construction detail 77

7.6 Applied force, reaction force, resulting displacement, measured stress strain characteristics and fitted stress-strain curve used in 1-mass model calibration at pre-stress value of 0 N/mm^2 79

7.7 Applied force, reaction force, resulting displacement, measured stress strain characteristics and fitted stress-strain curve used in 1-mass model calibration at pre-stress value of 1.42 N/mm^2 80

7.8 Applied force, reaction force, resulting displacement, measured stress strain characteristics and fitted stress-strain curve used in 1-mass model calibration at pre-stress of 4.3 N/mm^2 81

7.9 Applied force, reaction force, resulting displacement, measured stress strain characteristics and fitted stress-strain curve used in 1-mass model calibration at pre-stress of 7.1 N/mm^2 82

7.10 Applied force, reaction force, resulting displacement, measured stress strain characteristics and fitted stress-strain curve used in 1-mass model calibration at pre-stress of 10 N/mm^2 83

7.11 Applied force, reaction force, resulting displacement and measured stress strain characteristics at pre-stress value of 14 N/mm^2 84

7.12 Experimental setup represented as spring-mass system 85

7.13 Comparison of measured and calibrated results from the model at pre-stress of 0 N/mm^2 86

7.14 Comparison of measured and calibrated results from the model at pre-stress of 1.42 N/mm^2 86

7.15 Comparison of measured and calibrated results from the model at pre-stress of 4.3 N/mm^2 87

7.16 Comparison of measured and calibrated results from the model at pre-stress of 7.1 N/mm^2 87

7.17 Comparison of measured and calibrated results from the model at pre-stress of 10 N/mm^2 88

7.18 Comparison of measured and calibrated results from the model at press-stress of 14 N/mm^2 88

7.19 Schematic representation of the stress-strain properties of two non-linear springs in a back to back arrangement 90

7.20 Simulink model of mass-spring system 92

8.1 Components of mechanical model of a transformer 95

8.2 Proposed two-winding dynamic axial model 98

8.3 Dynamic axial and radial models combining technique 99

8.4 The effects of friction on axial motion 100

8.5 The effects of friction on radial motion 100

8.6 The cross-section of the core of the test transformer 101

8.7 The detail of the winding configuration of the test transformer . . . 102

8.8 Single phase two-winding test transformer in experimental setup . . 102

8.9 Comparison between stand-alone axial model and combined model of the test transformer 103

8.10 Single phase two-winding test transformer 103

8.11 Simulated and measured results of axial displacement at a pre-stress of 7.1 N/mm^2 104

8.12 Simulated and measured results of radial displacement at a pre-stress of 7.1 N/mm^2 104

8.13 Simulated and measured results of axial displacement at a pre-stress of 14 N/mm^2 105

8.14 Simulated and measured results of radial displacement at a pre-stress of 14 N/mm^2 105

8.15 Construction of the force and displacement sensors. The force sensor was used to measure the pre-stress and the two displacement sensors were used for axial and radial displacement 107

8.16 The cross-section of the transformer disk showing the profile of the area interfacing with the vertical spacers (pressboard) 107

B.1 Model to simulate axial behaviour of test test transformer implemented in Simulink 136

B.2 Model of the spring used as subsystem in axial model of a winding (Fig B.1) 137

B.3 Axial model of one disk used as a subsystem in the combined Simulink model (Fig B.4) 137

B.4 The representation of the combined model of the test transformer implemented in simulink 138

B.5 Radial model of a set of inner and outer disks of the test transformer 139

C.1 Dimensions of the test transformer 140

C.2 Design sheet of the inner winding of the test transformer 141

C.3 Design sheet of the inner winding of the test transformer 142

List of Tables

3.1 Arrangement of tappings and corresponding values of Λ [Franklin and Franklin, 1983] 19

7.1 Applied pre-stress values. 78

7.2 Damping coefficient at different pre-stress values 91

List of Symbols

$\mathbf{F}$	Force exerted on a conductor in magnetic field
$\mathbf{i}$	Current carried by the conductor in the magnetic field
$\mathbf{B}$	Flux density
D_m	Diameter of the limb of transformer
dx	thickness of the winding element
AT	Ampere-turn
B_r	Redial flux density
I_{sc}	Symmetrical short-circuit current
I_t	Current at which the test is conducted to measure the voltage
a	Fractional difference in winding height
I_t	Test current
I_{sc}	Symmetrical short circuit current
U	Rated apparent power per limb in kVA or radial displacement of outer winding or nominal voltage
P_c	Axial compression force
e_z	Per unit impedance voltage
f	Frequency, Hz
h	Winding height

NI	Ampere turns
l_{eff}	effective length of the path of the radial flux
Λ	Permeance per unit axial length of the limb
P_a	Axial force between two components of a winding
D_m	Mean diameter of the transformer
k	Total winding length occupied by one of the contiguous portion of the winding
d	Radial distance between two portions of one winding
Φ	the angle subtended by end from the position of the winding
ni	AT of one turn of the coil
D_c	Mean diameter of the turn
$r_1;\ r_2$	Distances from the winding ends 3.6
j_d	Current density
j	imaginary operator in complex algebra
$i_1;\ i_2$	current in the inner and outer winding conductor
σ_{mean}	Mean hoop stress at the peak of the first half cycle of current
W_{cu}	I^2R_{dc} loss in the winding in kW at 75^o at full load
p_r	radial force per mm of conductor
A_c	cross sectional area of each conductor
n_c	number of conductors in each disk
D_w	mean diameter of the winding
$\mathbf{x}$	the local displacement of mass
$\mathbf{c}$	damping coefficient

$\mathbf{k}$	spring constant
$\mathbf{x}_{in}$	the local displacement of disk of inner winding
$\mathbf{x}_{ot}$	the local displacement of disk of outer winding
θ	position angle determining the position of the rib
u	radial displacement of inner ring (inner winding)
v	circumferential displacement for inner winding
I_i	moment of inertia of inner ring (inner winding)
I_o	moment of inertia of outer ring (outer winding)
a_o	constant term representing uniform radial vibration
T^i	kinetic energy of the inner ring
T^o	kinetic energy of the outer ring
T	Total kinetic energy of a ring due to flexural vibration
ρ	mass density of copper
A_i	cross-sectional area of the inner ring
A_o	cross-sectional area of the outer ring
$\mathbf{H}$	Matrix related to the kinetic energy of copper ring
E_p	Strain potential energy (PE)
E_p^i	PE of inner ring
E_p^o	PE of outer ring
E_{p-ins}^i	PE of inner insulation rib (between core and inner winding)
E_{p-ins}^o	PE of outer insulation rib (between inner and outer winding)
ε	elasticity of copper conductor

I_i	moment of inertia of the inner ring
$\mathbf{D}$	Matrix related to stain potential energy of the copper ring
$E_{P_{ec}}$	Potential energy due to extension of the ring
$g(x)$	nonlinear stress strain characteristics of pressboard

Chapter 1

Introduction

A power transformer is the single most expensive component in generation, transmission and distribution substations. The importance of the transformer is not only due to its capital cost but the cost of undelivered energy in the event of failure, which makes the financial losses unaffordable. The rapid growth of power systems has given a raise to increased fault levels and the transformers should be able to handle the fault currents to ensure the reliability of the power system.

With growth of the power systems comes not only an increase in the short circuit levels but an increase in the system voltages. The higher voltages necessitate a more complex winding arrangement. There has been a better understanding of material properties in the last 15-20 years. Transformer manufacturers are exploiting this better understanding and produce transformers of smaller size with saving of material and transport costs. Unfortunately, this has lead to both conductor and insulating material operating close to their limits and an increase in failure in the early years of transformer life.

Research on the winding dynamics under short circuit conditions received a lot of attention between 1960 and the late 1970s. Many models were developed [Patel, 1972; Tournier et al., 1964; Madin and Whitaker, 1963b; Watts, 1963] to study the dynamic behaviour. All these models were focused on the axial movements and radial strength was ensured by simple and experience-based rules. All the models treated axial spacers (pressboard) as a linear springs except Patel [1972]. Patel [1972] developed a very detailed axial model which takes into account the non-linearity of the pressboard but neglects hysteresis and damping. He also assumes that pressboard only offers stiffness under compression and expansion comes under zero force. Swihart and Wright [1976] suggested a model of pressboard material. The model was able to predict the non-linear properties of the pressboard with the variation of pre-stress. However, the model was very complex and was not easily implementable in the modeling of large power transformers.

In this thesis, a different approach was used to handle the non-linear behaviour of pressboard. The dynamic stress-strain properties were measured and fed into the mathematical model as a lookup table. The measured properties were simplified to make the model manageable. Also the model presented is more realistic as the axial and radial movements are interlinked.

The objectives of this research are:

- To understand the dynamic stress-strain characteristics of transformer pressboard under varying pre-stress as the strength and stiffness of large windings depend upon the dynamic behaviour of the pressboard. Also to measure these characteristics under dynamic loading.
- To derive a model for oil impregnated pressboard which can be used to simulate the dynamic behaviour under varying pre-stress and transient loading of a transformer. This model will be used to simulate a complete transformer.
- To compare the simulated winding behaviour with the behaviour of an actual winding with a view to assessing the validity of the model.

The structure of the thesis is as follows:

Chapter 2: Electromagnetic forces in transformer windings
A brief description of electromagnetic forces is given; how the electromagnetic forces are experienced in a magnetic field; a brief outline of the forces in a two winding transformer.

Chapter 3: Prediction of axial electromagnetic forces
The available methods of force calculation are described. The most accurate methods are discussed in detail and compared. The method used in the thesis for force prediction is described and compared with finite element method.

Chapter 4: calculation of radial electromagnetic forces in concentric windings
The methods of radial force calculation are briefly described.

Chapter 5: Dynamic axial behaviour of transformer windings

A brief description of existing models is given. The equation of motion was derived for a two concentric winding transformer. The implementation of model in SIMULINK® with non-linear pressboard is given and simulated results are presented.

Chapter 6: Dynamic radial behaviour of transformer windings

The dynamic radial behaviour of concentric windings is discussed with a brief history. The equation of motion is derived and model is implemented in SIMULINK® and the results are described.

Chapter 7: Physical properties of pressboard under varying pre-stress

The chapter gives a brief history of the past research. The design of a dynamic stress-strain characteristics tester is discussed. The stress-strain properties of pressboard were measured and modeled to calibrate the model and to calculate the constants.

Chapter 8: Combined transformer model

Describes the construction of combined transformer model. Coupling of axial and radial behaviour, test setup and test procedure, comparison of simulated and measured results.

Chapter 9: Conclusions

The findings of the thesis and further research is identified.

Additional supporting information is given in the following appendices.

Appendix A: Matlab™ source codes

The MATLAB™ codes to predict oscillating electromagnetic forces are given. The codes to calculate the inputs to the stand-alone and combined SIMULINK® models is also given in this appendix.

Appendix B: Simulink® models

The combined and individual model implementation is presented in this appendix with the detail of main and subsystems.

Appendix C: Test transformer design and dimensions

The brief description of test transformer design.

For convenience of the reader, each chapter and appendix starts with a brief introduction which explains the main areas covered in the chapter or appendix.

Chapter 2

Electromagnetic forces in transformer windings

2.1 Introduction

The determination of forces in the winding of transformers under short-circuit conditions has been a matter of prime interest since the rapid growth in power systems and steady increase in the size of transformers. The work of predicting theses forces accurately has been in progress since early 1920's. The expansion of the power systems and increase in fault levels has made this issue more important than ever and to top it is the complex geometrical arrangements of the windings due to higher transmission voltages. The design and construction of the modern power transformer depends on the accurate prediction of these forces to avoid in-service failures and to reduce the replacement cost and cost of undelivered energy.

The methods available to calculate these forces range from being approximate to relatively more accurate. Approximate electromagnetic force prediction techniques are based on simplified assumptions. However, more accurate methods use more realistic criteria for electromagnetic force calculation.

In this chapter, the nature of the electromagnetic forces in concentric windings of transformers is discussed. The scope of this work is limited to the two-winding core type transformers. The multi windings transformers and shell type are not discussed here. The methods of prediction of electromagnetic forces are discussed in Chapters 3 and 4.

2.2 Electromagnetic force on a conductor in a magnetic field

When a conductor carrying current is placed in a magnetic field, it experiences a force. By 'Ampere's Law', each rectilinear element of conductor of length dl, carrying a current $\mathbf{i}$, in a magnetic field of flux density $\mathbf{B}$, perpendicular to it, is subjected to a force $d\,\mathbf{F}$ as mentioned in Eq 2.1. This force is perpendicular to the plane formed by the magnetic field and elemental conductor (Fig 2.1). Figure 2.1 also show the direction of the force with respect to the magnetic field and direction of the current (Fleming's left hand rule).

$$d\,\mathbf{F} = \mathbf{i} \times \mathbf{B}\ dl \tag{2.1}$$

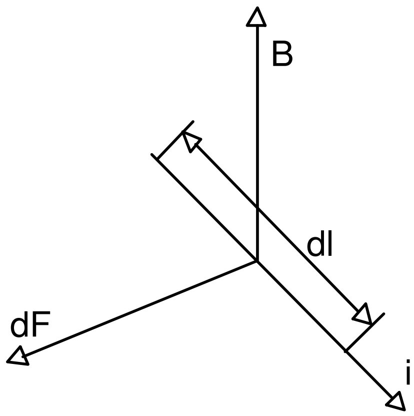

Figure 2.1: Force exerted on a conductor in magnetic field

2.3 Magnetic field in a two-winding transformer

The approximate magnetic field in a simple two-winding transformer is shown in the Fig 2.2. Although the construction of the transformer is the simplest, the field is by no means simple and cannot be calculated by simple methods. However, it is evident that this type of field will produce forces tending to separate the two windings, resulting in an outward force in the outer winding and the force on the inner winding is inward and compressive. If the windings are of the same length and accurately placed so that there is no axial displacement, each winding is subjected to a compressive force (discussed in Section 2.4) and there is no force to move the windings in the axial direction. Since the windings carry large currents in opposite directions (under through faults), any displacement from the precise balance position will lead to a large axial force tending to increase the displacement and produce more asymmetry in the windings. So the windings are designed in such a way that they have opposite radial forces but no unbalanced axial forces which is almost impossible to achieve. In real transformers, the windings can have a small initial displacement from the balanced position due to the construction limitations [Final Report: Cigré Working Group 12-04, 1979].

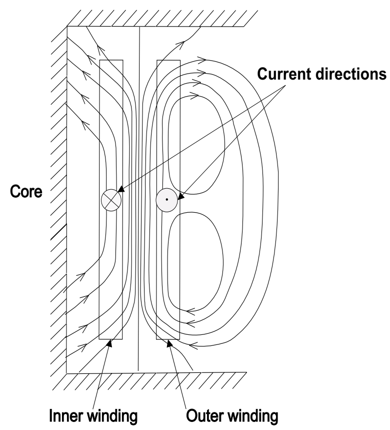

Figure 2.2: Magnetic flux pattern of a two-winding transformer

When a transformer is over-loaded or encounters a through fault, the primary and secondary ampere turns are in opposition with reference to the core, but this effect in the space between the two windings (inter winding duct) is cumulative and gives rise to a magnetic field in the inter-winding space (duct). This cumulative magnetic field causes leakage flux rise (flux linking to the one winding only) and mutual forces between the windings [Norris, 1957]. These forces have two components:

- Repulsive radial forces between inner and outer winding
- Axial forces, which can be further divided into two types,
  - Axial compression; and
  - Unbalanced axial forces due to asymmetry

2.4 Axial electromagnetic forces

The radial component of leakage flux linking the windings towards the ends is mainly responsible for the axial electromagnetic forces. In a transformer, if ampere-turns (AT) are balanced in windings, the axial forces have a compressive nature and tend to squeeze the winding in the middle. In axially symmetrical windings these forces were thought of less or of no importance as the compressive strength of the winding in the axial direction was thought to be much higher than the forces even under severe conditions [Arturi, 1992; Say, 1958; Franklin and Franklin, 1983]. If there is an asymmetry in the winding heights due to the tap position or for some other reasons, the ampere-turn unbalance increases and gives rise to repulsive forces, tending to break the winding apart from the middle. The concept of axial electromagnetic forces is shown in Fig 2.3.

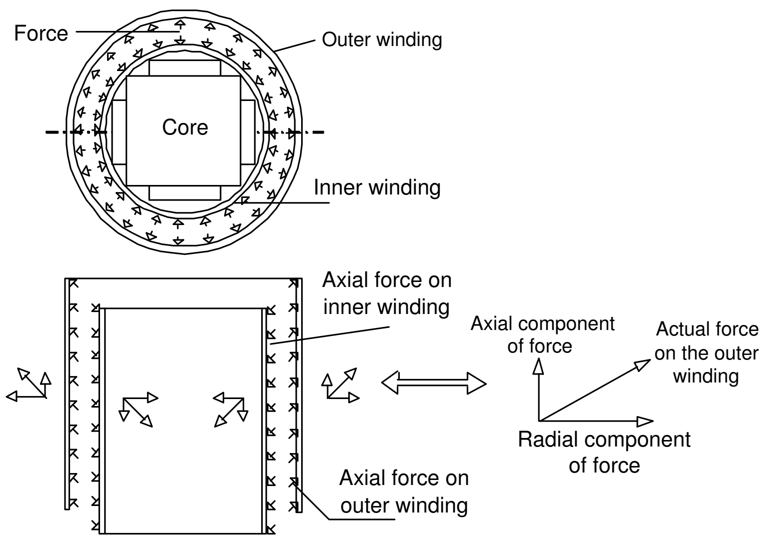

Figure 2.3: Axial and radial forces in concentric windings when the windings are axially non-symmetrical

2.5 Radial electromagnetic forces

In the case of a circular conductor (the winding coil of a transformer) or a coil, the current produces a force uniformly distributed around the periphery unless there is magnetic asymmetry. The radial electromagnetic forces develop when the coil current interacts with the axial component of its own magnetic flux.

In a transformer, the flux interacting with the windings occupies the space between the two windings as shown in Fig 2.2. Consequently, the outer coil is subjected to a pressure to extend the diameter of the coil, but the inner coil is under an external pressure and tends to collapse to the core (Fig 2.4). The circular coils are the preferable choice in a transformer as they are the strongest shape to withstand the radial pressure mechanically [Say, 1958].

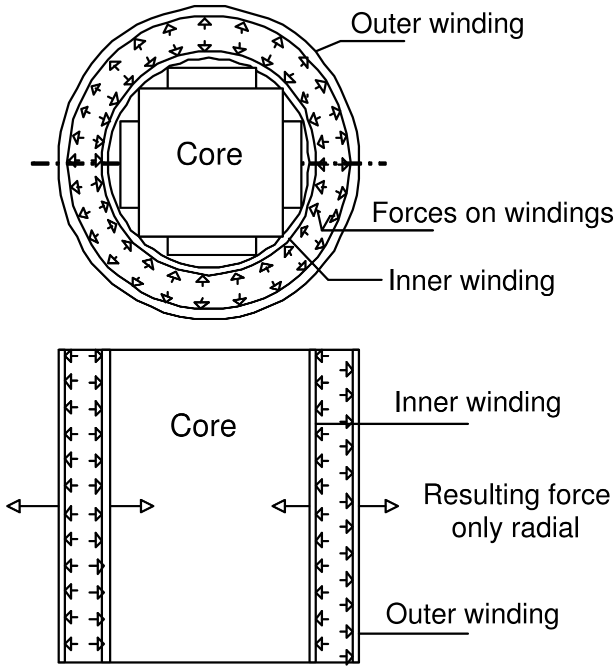

Figure 2.4: Radial electromagnetic forces in concentric transformer windings with axial symmetry

Chapters 3 and 4 deal with calculation of the axial and the radial electromagnetic forces respectively.

Chapter 3

Prediction of axial electromagnetic forces

3.1 Introduction

Forces in an axial direction can destabilize the winding causing a collapse of the winding and fracture or displacement of the end insulation (end ring) or clamping system. Excessive axial forces can be responsible for the bending of the conductor between the axial spacers or by compressing the insulation to such an extent to cause slackness and reduction of pre-stress which can lead to the displacement of spacers and subsequent failure. The destructive nature of these forces has made the problem of calculating the magnitude of the axial force important and has received considerable attention from researchers since the early 1920s.

The precise solution of the radial leakage field and the axial forces in transformer windings have been determined by various authors using a number of methods. These methods are complex and require the use of a computer if results are to be obtained quickly. However, elementary or simplified methods are also available. One of the simple methods, the residual ampere-turn method, gives reliable results. Attempts to produce closer approximations add greatly to the complexity without a corresponding gain in accuracy.

In this chapter, different methods of predicting electromagnetic force and their suitability for use in mechanical behaviour studies are briefly described.

3.2 Calculation of the axial force

The axial component or the forces in a transformer with conventional concentric windings cannot be calculated with high accuracy by elementary methods mainly because the curvature cannot be taken into account without using complex solutions which require the use of a computer. Before computers were available, a great deal of ingenuity was used in devising approximate methods for the calculation of axial forces. Since the rigorous solutions were too complex to be of any practical value, the usual approach was to make simplifying assumption, e.g. each unit length of the circumference of the winding was a portion of an infinitely long straight coil side. This enabled the radial component of the field to be calculated at any point. The effect of curvature was ignored or was taken into account by the use of empirical factors [Waters, 1966]. Measurements have shown that such methods give fairly accurate results in many cases, but the accuracy was poor for complex winding arrangements like single turn or high current windings and complex tapping arrangements. In general, these methods can give the axial force upon the whole winding or on the half or quarter of a winding with good accuracy, but are of little value in calculating the force upon a single coil or conductor, particularly if the winding arrangement is unusual.

However, these approximate methods are of great use to the designers since, they indicate quickly whether or not a given arrangement of windings will result in high axial force etc. In general, the methods used to calculate forces can be divided into following classes [Final Report: Cigré Working Group 12-04, 1979].

- Elementary methods
- Simple formula methods
- Sophisticated or more accurate methods

3.3 Empirical or approximate methods

These methods use empirical formulas to predict forces and are based on simplified theory and assumptions. A correction factor, based on experience or experimental findings, is applied to correct the results. These methods are explained below.

3.3.1 Indirect measurement of axial force

A simple method, developed by the Electrical Research Association (ERA) is explained in the book Franklin and Franklin [1983], for measurement of total axial force on the whole or part of a concentric winding. This method does not indicate how the force is distributed around the circumference of the winding but this is not a major disadvantage as the force along the circumference is not required, instead maximum force is needed.

Axial force calculation from radial flux measurement

If the axial flux linked with each coil of a disc winding at a given current is plotted against the axial position, the resultant curve represents the axial compression of the winding [Franklin and Franklin, 1983; Waters, 1966].

The flux density of the radial component of leakage field is proportional to the derivative of axial flux with distance along the winding. The curve of axial flux plotted against distance thus represents the integration of the radial flux density and gives the compression curve of the winding [Franklin and Franklin, 1983; Waters, 1966].

Volt per turn method

The voltage per turn is a measure of the axial flux. The voltage of each disc coil is measured, and divided by the number of turns in the disk this voltage per turn is plotted against the length of the winding [Waters, 1953]. This method can only be applied to a continuous disc winding by piercing the insulation at each crossover and the test is most conveniently carried out with the transformer short-circuited as for the copper-loss test.

Consider an axial force on a small axial length dx of a transformer winding as shown in the Fig 3.1. The element of the winding under consideration is situated at a distance x from the end a and occupies the full radial thickness of the winding. The length of the element can be calculated as πD_m around the circumference of the winding where D_m is the diameter of the limb. If the winding has AT as the ampere-turn per unit length, the element dx contains $AT \times dx$ ampere-turns. The axial force upon the whole element can be calculated as:

$$AT\ dx \times B_r \times \pi D_m$$

Where B_r is the radial component of flux density.

If the ampere-turn/unit length is constant along the whole length of the portion ab, then the total axial force on the portion is

$$F_{ab} = AT\pi D_m \int_a^b B_r dx$$

$\pi D_m \int_a^b B_r dx$ is the total radial flux passing out of the surface of the cylinder . It can be concluded that the axial force upon any portion of a winding, having uniform ampere-turns is given by the product of the ampere-turn per unit length and the total radial flux.

The radial flux at a point is normal to the cylinder surface. It is the part of the axial flux which enters the winding from one end and does not come out at the other end. Hence it is the algebraic difference between the axial flux at the two ends of the winding.

The axial flux at any point in the winding is proportional to the induced voltage per turn at that point. Hence the total radial flux of any portion of the winding and the resulting axial forces are proportional to the algebraic difference between the induced voltage per turn at the two ends of the winding. So if the distribution of the induced voltage per turn is known along the winding of a transformer, the axial force on the winding can be calculated. In fact, if the induced volt-per-turn along the winding is measured at a suitable current, the axial force on the winding can be calculated. However, these forces are the total forces on that winding and the variation around the circumference is not indicated.

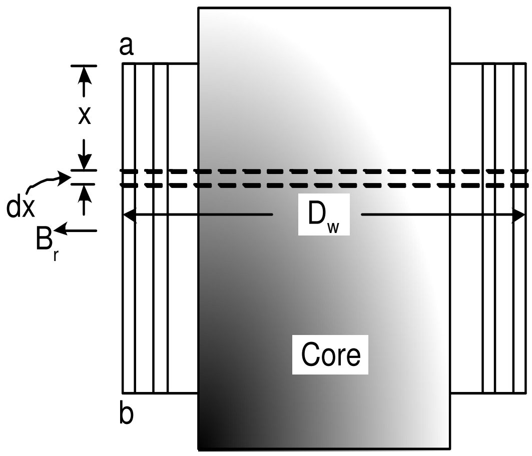

Figure 3.1: Method of calculation of radial flux by measurement of volt-per-turn [Waters, 1966]

Radial flux density

If the axial flux at any point x from the end of the winding is denoted by ϕ_A, the reduction or increase in flux is a short length dx is given by

$$d\phi_a = \pi D_m B_r \ dx \tag{3.1}$$

and

$$B_r = \frac{d\phi_A}{dx} \times \frac{1}{\pi D_m}$$

If V is the rms voltage induced per turn at any point, ϕ_A is the peak axial flux and B_r is the radial flux density then Equation 3.1 can be written as

$$B_r = \frac{dV}{dx} \times \frac{1}{4.44 f \pi D_m} \tag{3.2}$$

Where x and D_m are in meters and f is the frequency of the sinusoidal flux ϕ_A.

If the curve of volt-per-turn is plotted against distance along the winding, the slope of the curve represents the radial flux density at any point to the scale given by the Equation 3.2. This method is also valid if the turns per unit length over the length of the winding are not constant.

Volt-per-turn measurement for axial force calculation

Consider a transformer with two windings, having NI rms ampere-turns per unit length and induced voltages per turn of V_1/N_1 and V_2/N_2. The total peak radial flux is given by

$$\phi_r = \frac{\left(\frac{V_1}{N_1} - \frac{V_2}{N_2}\right)}{4.44 f} \tag{3.3}$$

The peak axial force upon the winding

$$F_A = \sqrt{2} \ NI \frac{\left(\frac{V_1}{N_1} - \frac{V_2}{N_2}\right)}{4.44 f} \tag{3.4}$$

hence

$$\text{Peak axial force} = \frac{\text{rms ampere-turns} \times \text{rms volt-per-turn difference}}{4.44 \text{ f}}$$

The scale of force at 50 Hz is given by Franklin and Franklin [1983]

$$1 \text{ volt (rms)} = \frac{\text{rms ampere-turns per mm}}{15750} \text{ kN (peak)}$$

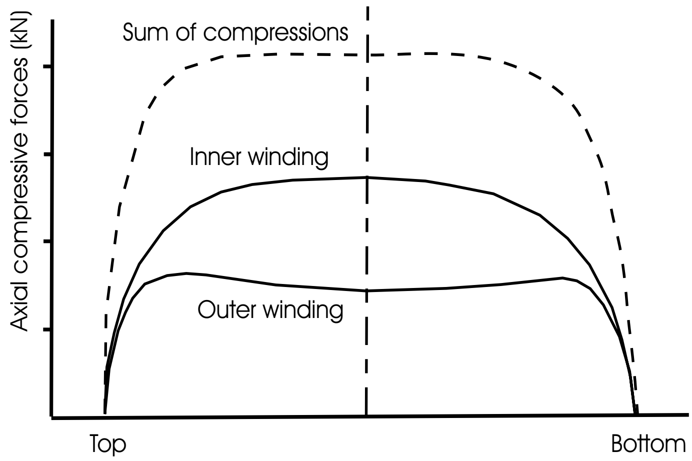

Figure 3.2: Axial compression curve for untapped transformer windings [Waters, 1966; Franklin and Franklin, 1983; Waters, 1953]

To convert the measured voltages to forces under short-circuit conditions the values must be multiplied by $(1.8I_{sc}/I_t)$ where I_{sc} is the symmetrical short-circuit current and I_t, the current at which the test is carried out.

To obtain the compression curve it is necessary to know the points of zero compression, and these have to be determined by inspection. This is not difficult since each arrangement of windings produces zero points in well defined positions.

Figure 3.2 shows axial compression curves obtained on a transformer having untapped windings of equal heights. There are no forces tending to separate the coils in the axial direction. The ordinates represent the forces on coils at all points due to the current in the windings. The shape of the curve shows that only in the end coils are there appreciable forces, as the end coils have maximum radial flux linked to them. The dotted curve shows the sum of the axial compressive forces for the inner and outer windings. This method has been explained in detail by Waters [1966]. The maximum force is given by [Franklin and Franklin, 1983]

$$P_c = \frac{510\ U}{e_z\ fh}\ \text{kN} \tag{3.5}$$

Where:

U	=	nominal voltage
P_c	=	axial compression forces, N
e_z	=	per unit impedance voltage
f	=	frequency, Hz
h	=	axial height of the winding in mm

This is the force at the peak of the first half cycle of fault current, assuming an asymmetry factor of 1.8.

It is to be noted that the forces in a transformer winding depend only on its position and on the total ampere-turns, and not on the physical size. Thus, smaller scaled model transformers were suitable for investigating forces. For large units where calculations were difficult, it was more economical to produce a model and measure the forces than to carry out elaborate calculations [Waters, 1966; Franklin and Franklin, 1983]. However, in recent years, a significant development of FEM software has enabled the force calculation to be accomplished easily but in cases where the winding and tapping arrangement is complex, the FEM software takes a long time to calculate forces on different portions of winding and other structures.

The voltage per turn method has proved very useful in detecting small accidental axial displacements of windings from the normal position during manufacture and transportation [Waters, 1966]. However, this may require piercing of insulation which is not a good idea for high voltage transformers and the method is only suitable for small lower voltage units.

3.3.2 Residual ampere-turn method

This is one of the oldest method, and follows H.O. Stephen's[1] method of calculating the interleaved component or reactance . This method has a long history of use and Say has discussed it briefly in his book [Say, 1958]. This method provides the solution for axial forces only. The brief explanation of this method is given here but detail explanation is given by the previous researchers [Waters, 1966; Franklin and Franklin, 1983; Say, 1958].

Any arrangement of concentric windings in which the sum of the ampere-turns is zero is split up into two groups each having balanced ampere-turns, one producing an axial field and the other a radial field. The radially acting ampere-turns are responsible for the radial flux which causes the axial force in the windings. At the same time it causes a slight increase in the percentage reactance.

The radial ampere-turns at any point in the winding are calculated by taking the algebraic sum of the ampere-turns of the primary and secondary windings at that point and at the end of the windings. A curve plotted for all points is a residual or unbalanced ampere-turn diagram from which the method gets its name. It is clear

[1]Stephens H.O., 'Transformer Reactance and Loss with nonuniform windings.' Elect. Eng., vol 53, Feb 1934, pp 346-349 cited in Waters [1966]

that for untapped windings of equal length and without axial displacement have no residual ampere-turns or forces between the windings. Although there is no axial thrust between windings, internal compressive forces and forces on the end coils still are present.

The method of determining the distribution of radial ampere-turns is illustrated in Fig 3.3 for a simple case of concentric winding having a fraction of the total length tapped at the end of the outer winding. The two components I and II of Figure 3.3-b are both balanced ampere-turn groups and, when superimposed, produce the given ampere-turn arrangement. The diagram showing the radial ampere-turns plotted vs distance along the winding is a triangle, as shown in Fig 3.3-c, having a maximum value of $a(NI_{max})$, where (NI_{max}) represents the ampere-turns of either the primary or secondary winding and a is the fractional difference in height of the windings as shown in the Fig 3.3 (a).

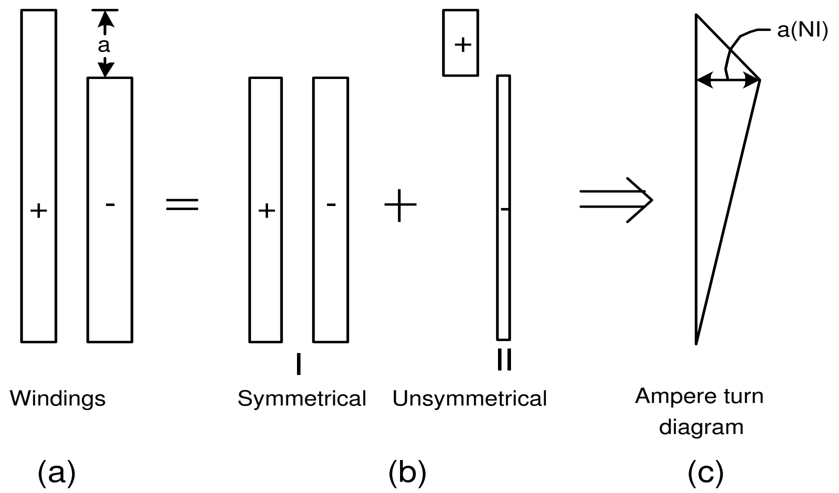

Figure 3.3: Determination of residual ampere-turns of winding tapped at top end [Waters, 1966; Franklin and Franklin, 1983]

To determine the axial forces, it is necessary to find the radial flux produced by the radial ampere-turns, or in other words to know the effective length of the path of the radial flux on all points along the winding. In previous work, an assumption was made that this length stays constant and does not vary with axial position in the winding. This was considered to be a rough approximation to obtain simple results [Waters, 1966; Franklin and Franklin, 1983]. However, tests show that this approximation is reasonably accurate and flux does in fact follow a triangular distribution curve of the same shape as the residual ampere-turns.

The calculation of the axial thrust in the case shown in Figure 3.3 can be calculated. l_{eff} is the effective length of the path of the radial flux. Since the mean value of the radial ampere-turns is $\frac{1}{2}a(NI_{max})$, the mean radial flux density at the mean diameter of the transformer limb is

$$B_r = 4\pi \times 10^{-7} \times \frac{a(NI_{max})}{2\ l_{eff}} \qquad \mathrm{T} \tag{3.6}$$

and the axial force on either winding of NI_{max} ampere-turns is

$$P_a = \frac{2\pi a(NI_{max})^2}{10^{10}}\ \frac{\pi D_m}{l_{eff}} \qquad \mathrm{kN} \tag{3.7}$$

where:

I_{max}	=	maximum current (A)
D_m	=	mean diameter of the transformer limb (mm)
l_{eff}	=	effective length of the path of the radial flux (mm)
a	=	fractional difference in winding heights

If

$\Lambda = \pi D_m / l_{eff}$,

Λ is the permeance coefficient per unit axial length of limb. It gives the force for all windings having the same properties irrespective of physical size. Also the calculation of the ampere-turns is not difficult. In order to cover all the cases, it is necessary to study only how Λ varies with the properties of the core, proximity of the tank, dimensions of the duct, dimensions of the windings and tapping arrangement.

Effective length of path for radial flux l_{eff}

Before digital computers were available, the value of l_{eff} was determined usually by extending Rogowski's work on the reactance of interleaved windings [Hague, 1929]. Tests carried out on an experimental transformer by the method described by Waters [1966] showed that expressions determined in this way cannot be applied generally and these results were confirmed by Klichler [Waters, 1966], who pointed out that Rogowski's method fails in many cases and suggests an empirical correction based on experience. He concluded that the length of path for the radial flux in transformers of normal proportions having a simple tapping arrangement of Fig 3.3 is given by

$$l_{eff} = 0.222h \tag{3.8}$$

where h is the height of the winding.

Equation 3.7, is applicable for a simple tapping arrangement and would not be used in practice, but the same method is applicable for all tapping arrangements. The ampere-turns must be determined, the residual ampere-turn diagram constructed or calculated, and with the appropriate value of Λ the axial force on the part of either winding under each loop of the residual ampere-turn diagram can be calculated. This has been explained by Waters [1966], Franklin and Franklin [1983] and Say [1958].

The value of Λ used in each case has been studied empirically [Waters, 1966, 1953], using two transformers specially designed to suit radial flux measurements (The transformer design is described in detail in the books [Waters, 1966] and [Franklin and Franklin, 1983]). The values of Λ applies exactly to these particular transformers, which were designed to have widely different values of ratio and (window height)/(core circle diameter).

The factors such as clearance between winding and core, duct width, proximity of tank, radial thickness of the windings have an effect on Λ, which is small. The values given should apply within narrow limits to any transformers having proportions not too different to those of Fig 3.4. In extreme cases with large duct widths, the accuracy decreases, as shown in Waters [1966], which gives a comparison between this method and a more accurate computer calculation for larger changes in configuration.

The proximity of the tank increases the value of Λ for the outer limbs of a three-phase transformer, but had no significant effect on the middle limb. A limited number of tests showed the presence of the tank did not increase the forces in the outer limbs to values greater than those in the middle limb. The presence of the tank increases the forces in a single-phase transformer wound on one limb, but in this case the value of Λ would not exceed that of the middle phase of a three-phase transformer.

The values of Λ to be used for usual arrangements of tappings are given in Figure 3.4 and Table 3.1 for three-phase balanced loading. They apply to the middle limb, and the total value of the force on the part of the winding.

The forces calculated with this method are not uniformly distributed around the circumference, but concentrated in the window [Franklin and Franklin, 1983; Waters, 1953, 1966]. The plot of Figure 3.5 is for a transformer which is 10 % tapped out

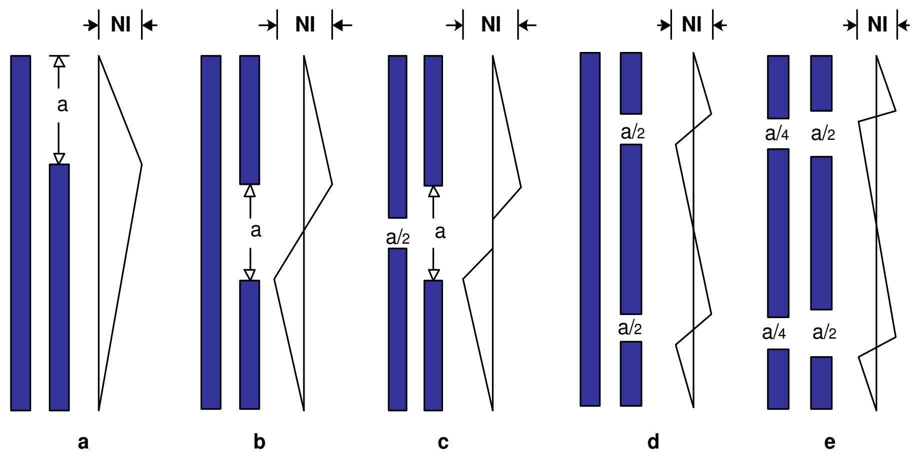

Figure 3.4: Arrangement of tappings and resulting residual-ampere-turns

Arrangement of Tappings	P_a (kN)	Λ $\left(\frac{\text{window height}}{\text{core circule}} = 4.2\right)$	Λ $\left(\frac{\text{window height}}{\text{core circules}} = 2.3\right)$
Case A Fig 3.4	$\frac{2\pi a(NI)^2\Lambda}{10^{10}}$	5.5	6.4
Case B Fig 3.4	$\frac{\pi a(NI)^2\Lambda}{2\times 10^{10}}$	5.8	6.6
Case C Fig 3.4	$\frac{\pi a(NI)^2\Lambda}{4(1-\frac{1}{2}a)\times 10^{10}}$	5.8	6.6
Case D Fig 3.4	$\frac{\pi a(NI)^2\Lambda}{8\times 10^{10}}$	6.0	6.8
Case E Fig 3.4	$\frac{2\pi a(NI)^2\Lambda}{16(1-\frac{1}{2}a)\times 10^{10}}$	6.0	6.8

Table 3.1: Arrangement of tappings and corresponding values of Λ [Franklin and Franklin, 1983]

at the middle of the outer winding on all three phases. The slight enhancement of flux density is not due to the core of the adjacent limbs, but mainly due to the ampere-turns of the windings of the side limbs.

In a three-phase transformer, the local increase of force above the mean was 25%. Hence the greatest axial forces are in the window. For a single-phase transformer wound on two limbs the force per unit of circumference is 50% greater than the mean and in a three-phase transformer 25% greater than the mean value calculated from the values of Λ given in Table 3.1.

3.4 Two-dimensional methods

The residual ampere-turn method can provide solution for axial forces in a winding or a part of the winding which has an asymmetrical distribution of the ampere-turns and does not take into account the forces present in a uniform untapped winding.

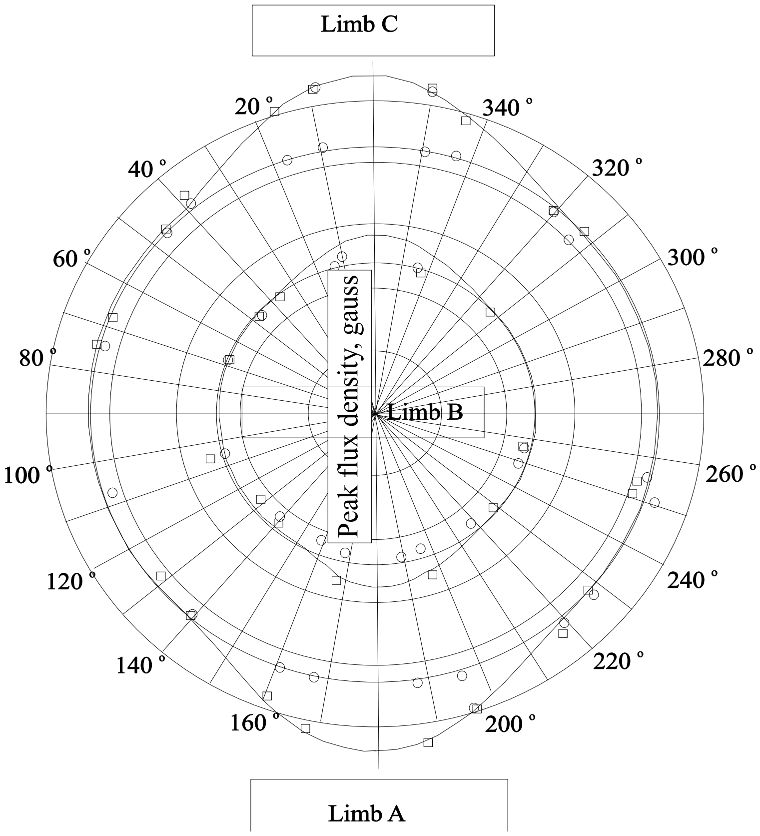

Figure 3.5: Polar diagram of flux density for the middle limb of a transformer with 10% tapped from the middle of the outer winding [Waters, 1966; Franklin and Franklin, 1983]

Attempts to formulate a simple method which can help the prediction of axial compression in any part of the winding have been made with some success. All the available methods are based on two-dimensional techniques with suitable corrections for curvature and the effect of the core.

To simplify the problem, Billing [1946] and Waters [1966] suggested that the windings should be represented by infinitely long straight coil sides; as shown in Figure 3.6. The forces in a length equal to the mean length of turn, are taken as representative of a transformer. The radial component of flux density near such a straight coil side is proportional to $\ln\left(\frac{r_2}{r_1}\right)$, and the axial component is proportional to the angle ϕ subtended at the ends (Figure 3.6). By simple integration the axial force between two contiguous portions of winding occupying the total axial length is calculated as [Waters, 1966]

$$P_a = P\psi(k, d) \tag{3.9}$$

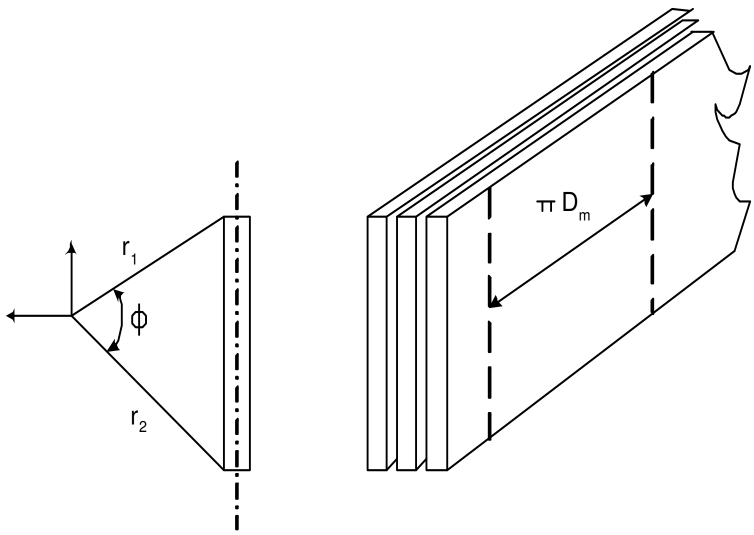

Figure 3.6: Winding representation as infinitely long two-dimensional straight conductor [Waters, 1966; Franklin and Franklin, 1983]

where

$$P = \frac{2(NI)^2}{10^{10}} \times \frac{\pi D_m}{h} \text{ kN} \qquad \text{[Waters, 1966; Franklin and Franklin, 1983]}$$

Where

$$\begin{aligned} D_m &= \text{mean diameter of the transformer, mm} \\ h &= \text{length of the winding, mm} \\ (NI) &= \text{ampere-turns of one winding} \end{aligned}$$

and $\psi(k,d)$ is a function of the fraction k of the total winding length occupied by one of the contiguous portions of winding and d is the radial distance between them also expressed as a fraction of the winding length. Therefore as determined by Waters [1966].

$$\begin{aligned} \psi(k,d) \quad = \quad & \frac{k}{2}\ \ln\left(\frac{1+d^2}{k^2+d^2}\right) \ + \ \frac{1-k}{2}\ \ln\left(\frac{1+d^2}{(1-k)^2+d^2}\right) \\ & -d\left\{\tan^{-1}\!\left(\frac{k}{d}\right) + \tan^{-1}\!\left(\frac{1-k}{d}\right) - \tan^{-1}\!\left(\frac{1}{d}\right)\right\} \end{aligned} \tag{3.10}$$

Tables of this function are available and it is also shown how these may be used to calculate the forces in any winding arrangement [Waters, 1966].

This method is based on the assumption that the ampere turns are concentrated along a line at the mean diameter of the winding and d is the radial distance between winding centers. The method produced close results in comparison with Residual Ampere Turn method 3.3 for compressive forces [Waters, 1966].

3.4.1 Two-dimensional method of images

To apply the above method to complicated cases, it was proposed to employ the method of images using an iron boundary as shown in Fig 3.7-b. This representation is on one side only, and is an attempt to represent the presence of the core.

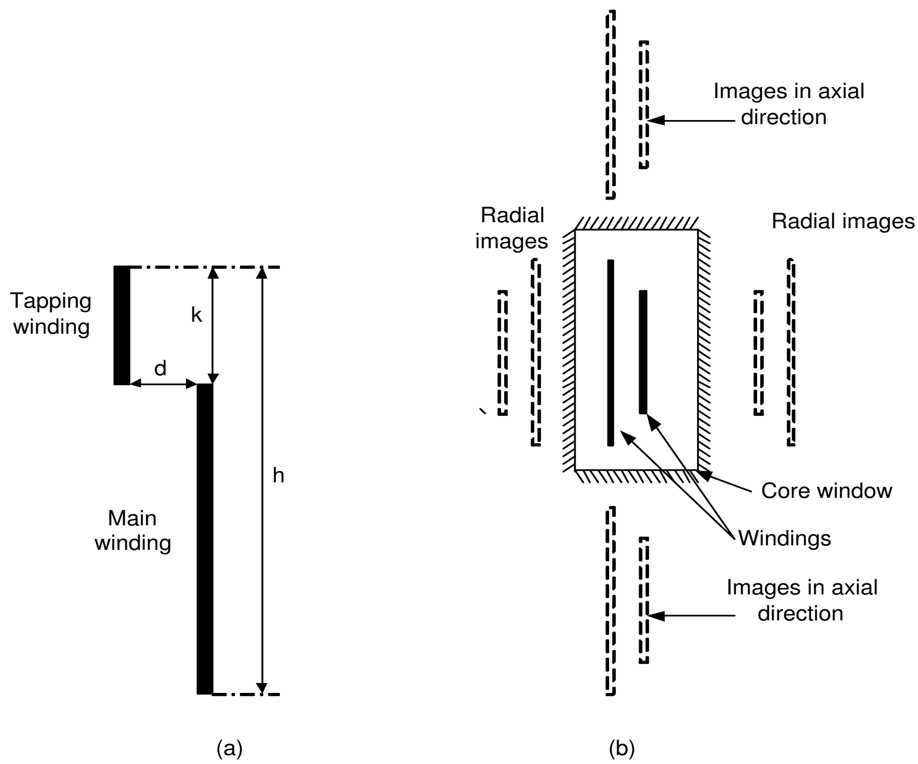

Figure 3.7: Contiguous winding sections used in axial force calculation and images representing the effect of the core

Waters [1966], suggested that this method does not give accurate results if only one side boundary is employed. Waters suggested that top and bottom boundaries representing the yoke can be omitted without loosing accuracy.

3.4.2 Two-dimensional graphical image method

This method has been described by P Ignacz[2]. The method is similar to one explained above but in a simplified form by an ingenious device developed by P Ignacz (Detail of the method is given in Waters [1966]). Instead of carrying out tedious integration of Equations 3.9 and 3.10, the force on each coil is calculated individually using the picture given in Fig 3.6 with a simple relation developed empirically by Ignacz.

$$\begin{aligned}\phi_r &= C\phi \\ \phi_a &= C \ln\left(\frac{r_2}{r_1}\right)\end{aligned}$$

where ϕ_r and ϕ_a are the radial and axial components of the force respectively and

$$C = \frac{2.04}{10^8} \times \frac{NI}{h} \times NI\pi D_c \text{ kg}$$

ϕ	=	the angle subtended by end from the position of the winding (Fig 3.6)
NI	=	AT of the winding
πD_c	=	mean length of the turn
$r_1,\ r_2$	=	distances from the winding ends Fig 3.6

More detail of how this method is used is given in Waters [1966].

The method recognizes that the force on a coil, due to the winding of which it is a part of, can not be calculated without reference to its dimensions. Curves have been prepared (by taking dimensions into account) to enable this to be done quickly. The effect of the core is taken into account by the method of images. The results obtained by this method correlate well with the measured values. The method proved to be a practical method where calculations are done by hand [Waters, 1966].

3.5 Calculation using Fourier series

Roth [Hague, 1929; Waters, 1966] was the first to attempt accurate calculations of the forces in a transformer. To start with, he produced a solution in two dimensions only, using double Fourier Series which became the basis of later work in two dimensions. In 1936 he produced a solution using cylindrical co-ordinates and correctly took into account the curvature of the windings. Computer codes of this method are available [Waters, 1966].

[2] Ignacz P, Determination of short-circuit forces in transformer windings. '*Institute of Electrical Power Research'*, Budapest. (in Hungarian) cited in [Waters, 1966]

In the 2-dimensional method the windings are considered as infinitely long straight rectangular bars having the same cross-sections as the windings and uniform current distribution, in a closed iron duct as shown in Fig 3.8.

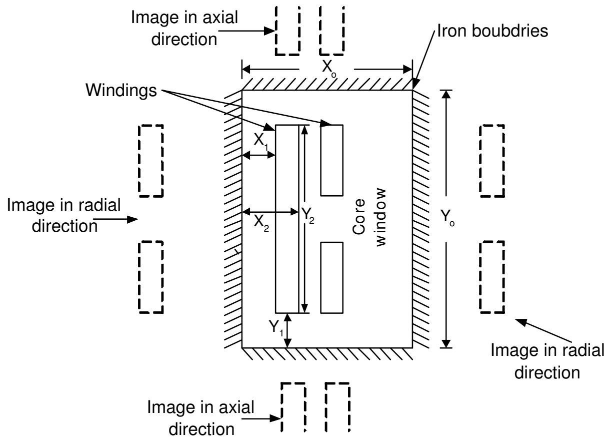

Figure 3.8: Two-dimensional representation of transformer windings with images [Waters, 1966]

The force on a whole winding can be calculated by taking a length of the bar equal to the mean length of the turn of the winding. This arrangement is a close approximation to the straight portions of a winding in a shell-type transformer, but it is not accurate for a core-type transformer. Pichon and Hochart [1958] have compared the two-dimensional method with the more accurate three-dimensional solution in cylindrical co-ordinates on the computer and preferred the former for large transformers on account of its simplicity. The forces in the window are accurately predicted by taking the window dimensions as the iron boundary. Less accuracy is obtained for forces on the windings away from the core window [Waters, 1966].

Considering the arrangement of Fig 3.8, the permeability of the iron may be assumed to be infinity with only a negligible loss in accuracy. This enables the flux to enter the walls at right angles and the field inside the duct is not changed if the iron is replaced by an infinite series of images in all four directions as shown dotted in Figure 3.8. The problem is reduced to calculating the flux density at any point due to the bars and the array of images .

If A is the vector potential at any point inside the slot then the differential equations governing the field are,

$$\frac{\partial^2 A}{\partial x^2} + \frac{\partial^2 A}{\partial y^2} = 0 \tag{3.11}$$

in the duct of the winding,

$$\frac{\partial^2 A}{\partial x^2} + \frac{\partial^2 A}{\partial y^2} = 4\pi j_d \tag{3.12}$$

Where j_d is the current density in the cross-sections of the windings.

Solutions of these equations may be expressed in either single or double Fourier Series, the constants being determined by the positions of the iron boundaries, number, position and dimensions of the windings. The mathematical derivations are long and tedious and have been carried out by several researchers in this field, who have continued the work of Roth and are listed in Waters [1966].

The scope of this work is not to produce the derivation, and only the final solution is given. The solution using a single series is mathematically equivalent to the double series method of Roth and is an attempt to simplify the final result, but now with powerful computers the need for mathematical simplification is not essential. However, DeKuijper [Waters, 1966] considered the single Fourier series to have some advantages.

Pichon and Hochart [1958] have successfully adapted the original solution of Roth for the computer codes and have indicated the programming technique. The bottom left-hand corner of the window is taken as the origin and the forces are calculated from the ampere-turns and the coordinates of the corners of the windings and the iron boundary, all of which are assumed to have rectangular cross-sections as shown in Fig 3.8. The complete solutions for the radial force and the axial force are given in Waters [1966] and Hague [1929]. It should be noted that for the force on a part of a winding, the part has to be considered as a separate winding with its correct value of ampere-turns [Waters, 1966]. This method is simple and calculations can be carried out by hand but are very time consuming hence computer use is recommended [Waters, 1966].

3.6 Methods using digital computers

The configuration of a three-phase core-type transformer does not lend itself to developing rigorous mathematical expressions for the leakage flux or for the forces on the conductors at any point in the windings. In order to deal with a transformer mathematically, it must be represented in an idealized form having axial symmetry as shown in Fig 3.9. The core is assumed to be cylindrical and the yokes represented by infinite planes, all having infinite permeability. An outer iron boundary may be assumed co-axial with the limb, as shown in Fig 3.9, but the solution allows this boundary to be at any distance up to infinity. The windings are co-axial with the limb and of rectangular cross-section with uniform current density. If a winding has parts of different current densities, it is necessary to treat these parts as separate windings. Mathematically this presents no difficulty. Tapered windings can be dealt with only by using a stepped representation, each step being treated as a separate winding [Waters, 1966].

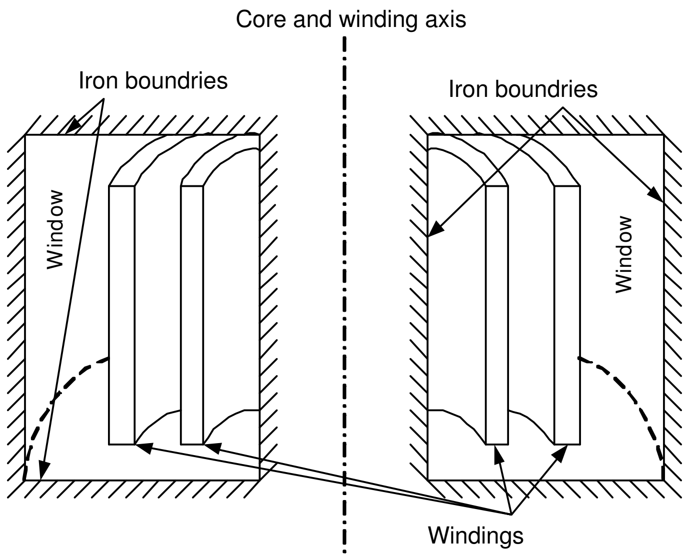

Figure 3.9: Idealized core-type transformer with curvature of windings

Experience has shown that the single limb idealization (Fig 3.9) enables highly accurate estimates of flux density and electromagnetic forces. The assumptions of infinite permeability, uniform current distribution, instead of discrete conductors and infinite planes to represent the yoke, lead to errors which are negligible compared with the errors due to differences between the design dimensions and manufactured dimensions of the transformer. Curvature may be taken into account correctly and since no other assumptions were made (apart from those mentioned above), it is possible to deal with unusual arrangements of windings. The approach to the problem is simple. More details on this method in given in Waters [1966] and Hague [1929] which describe the method in detail.

3.6.1 Smythe's solution

Roth's method can be simplified considerably by assuming that the ampere-turns of each winding are concentrated in a thin cylinder which is assumed to have the same mean diameter as the actual winding. Based on this idea, Smythe [Waters, 1966] suggested a solution, which simplifies the problem and makes it possible to calculate the forces using an ordinary calculator.

Vein [Waters, 1966] has used Smythe's solution to produce expressions for the force in a multi-layer winding and proved that if the ampere-turns are concentrated in thin layers the method should give accurate results.

3.6.2 Rabin's Solution

Rabin's solution is the simplified solution of Roth's [3] which was produced by taking into account the curvature of the windings . In 1956 Rabin [Waters, 1966] introduced a simpler solution using a single Fourier series with coefficients which were Bessel and Struve functions. The expression he used for the reactance calculation when differentiated, leads to flux density and to the electromagnetic force. Rabins method has been used in mid 1960s for software tools. The Bessel and Struve functions are also generated by computer using appropriate expressions. Kuster [Waters, 1966] has given a method to calculate these functions by computers, but in certain cases, double-length arithmetic is required to obtain adequate accuracy. A more suitable method has been provided by Chebyshew [4] which is more useful particularly when the 'double-length arithmetic' is not provided.

3.6.3 Solution by analogue computer

Goldenhberg [Waters, 1966] has shown how the basic equations for the flux and forces in a transformer with axial symmetry may be solved by means of a two-dimensional resistance network. This solution is based on a finite difference approximation of the basic differential equations and boundary conditions. The number of resistance elements required are very large. But if the solutions of a large number of problems of this type was required it might be economical to set up such a network. Once the setup is made, it would be more flexible in use than a digital computer and could cope with different arrangements of windings, e.g. triangular shapes, which could not be easily done with a digital computer.

3.6.4 Image method with discrete conductors

This method uses a technique similar to that mentioned in Section 3.4.1. Here each turn of the winding is regarded as a straight conductor. A similar method has also been used by the Cigré Working Group in the Final Report: Cigré Working

[3] Roth E: (cited in Waters [1966])

[4] cited in Waters [1966]

Group 12-04 [1979] to calculate the forces in a core type transformer. The force on a bundle of conductors, a disk or any section of winding may be calculated by regarding them as filaments carrying current at their geometrical centers. The cross-section of the conductor is assumed as circular but the square and rectangular cross-sections can be accommodated with same simplification by using the formulas which take into account the cross-sections of different geometries [Hague, 1929]. Alternatively, multiple circular conductors of suitable diameter can be packed into the shape of the conductor in use. Figure 3.10 shows the conductors and the core in two-dimensional geometry and Fig 3.11 shows the arrangement of images to take into account the iron boundaries.

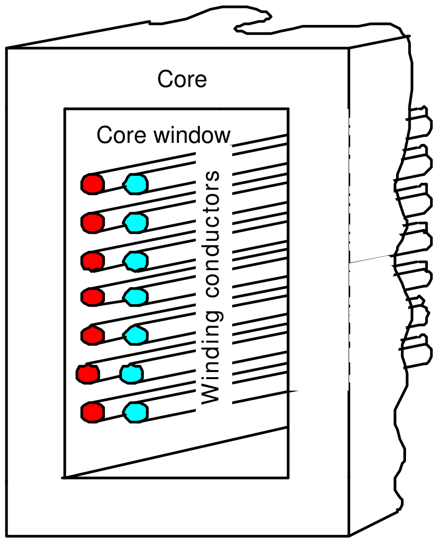

Figure 3.10: Discrete image method

This method uses a simple formula to calculate the force on each winding conductor/turn. It is assumed that the turns are conductors of equal length, carrying current and running in parallel. The force can be determined as follows,

$$\mathbf{F} = \mathbf{B}\mathbf{i}\; l \sin\theta \tag{3.13}$$

Where $\mathbf{B}$ is the flux density at a particular turn and $\mathbf{F}$ is the force on that turn, and

$$\mathbf{B} = \mu_0 \frac{1}{2}\frac{\mathbf{i}_1}{h} \tag{3.14}$$

where $\mathbf{i}_1$ is the current in the conductor and h is the distance between the two conductors

$$\mathbf{F} \;= \mu_0 \;\frac{\mathbf{i}_1\mathbf{i}_2}{h} \tag{3.15}$$

$$\mathbf{F} = 2\pi l.10^{-7}\frac{\mathbf{i}_1\mathbf{i}_2}{h} \tag{3.16}$$

The flow chart in Fig 3.12 shows the procedure used for developing the MATLAB™ code used to calculate the forces on the inner and outer winding conductors (disks or turns). The developed code is given in appendix A. MATLAB™ was chosen because it is a high level mathematical and engineering language with good graphical capabilities. The output of this code can be easily used in SIMULINK® for modeling of the dynamic behaviour of the transformer which is the main objective of this work.

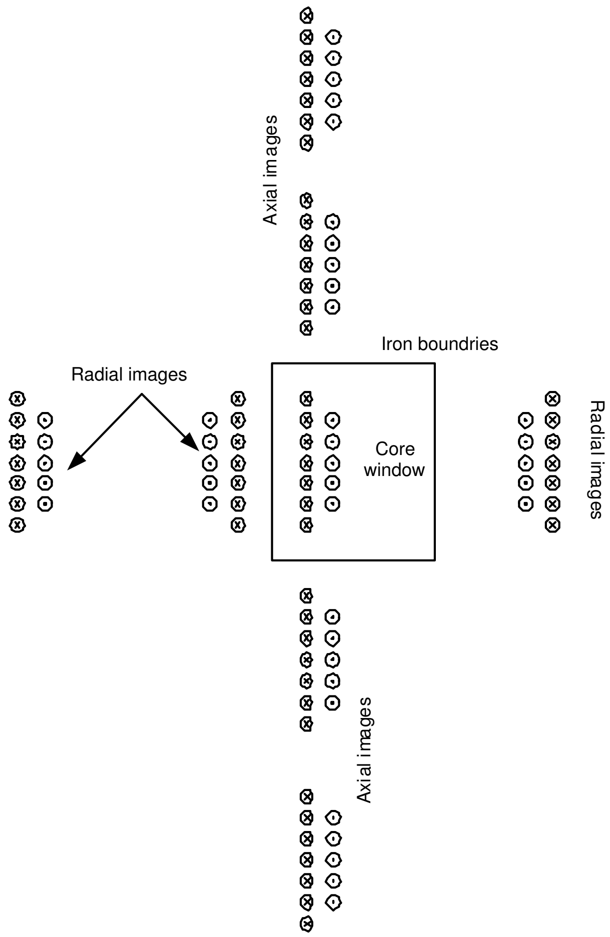

Figure 3.11: System of images in discrete image method for a two-winding transformer

The forces calculated with this method do not consider the core window. Also it is assumed that the whole length of turn πD_m (where D_m = mean diameter of turn) is situated under the yoke. This limitation can be overcome by considering that only the conductor length under the yoke is used for the yoke side images. With this method, axial and radial forces are calculated at the same time if the position of the conductor is represented in complex form i.e. $(x + jy)$, where x and y are the coordinates of a two dimensional system. This is the method that was used for calculating the time dependent forces on each disk of the winding of the test transformer in Chapters 5 and 6 and in Appendix A. This force is the input of the dynamic SIMULINK® model used to study the behaviour of the windings under short circuits.

3.6.5 Finite element method (FEM)

The finite element method is a method for solving problems which are usually defined as a continuous domain either by differential equations or by equivalent global statements. To make the problem manageable to numerical solution, the infinite degrees of freedom of the system are discretized or replaced by a finite number of unknown parameters, as a process of approximation. So the concept of 'Finite Element' is replacing the continuous system by a number of sub-domains or elements whose behaviour is modeled adequately by a limited number of degrees of freedom using processes available in the analysis of discrete systems.

In this work the Maxwell® Finite Element Analysis (FEA) software from Ansoft Corporation was used to calculate the force on the conductors of the test transformer. The software does take into account the non-linearity of the iron.

The force on each disk of the test transformer was calculated with FEM (Maxwell) and with the discrete image method at $1kA$ per disk. This was to compare the accuracy of the much faster discrete image method to the more time-consuming FEM. The magnetic field pattern (from FEM) is given in the Figure 3.13. The comparison of the results is given in Figures 4.4 and 4.5 for the inner and outer windings respectively. The discrete image method shows lower accuracy in calculation of radial forces and can be improved by the addition of more images in the radial direction. The accuracy of the discrete image method can be further improved by assuming images only for the conductors under the yokes which can not be done in two-dimensional FEM and 3-dimensional FEM is required which is more time consuming than 2-dimensional FEM.

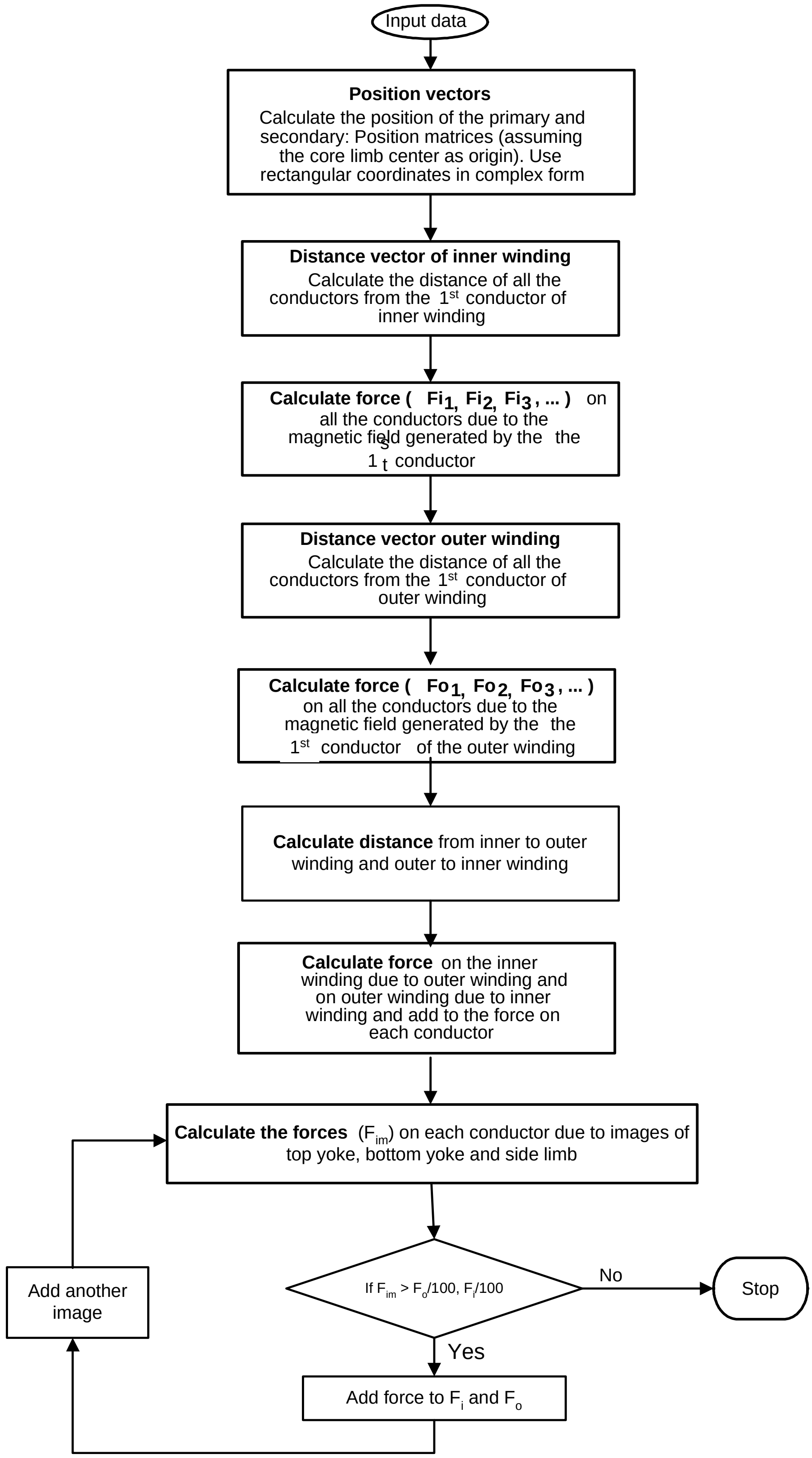

Figure 3.12: Flow chart of system of the images in discrete image method for a two-winding transformer

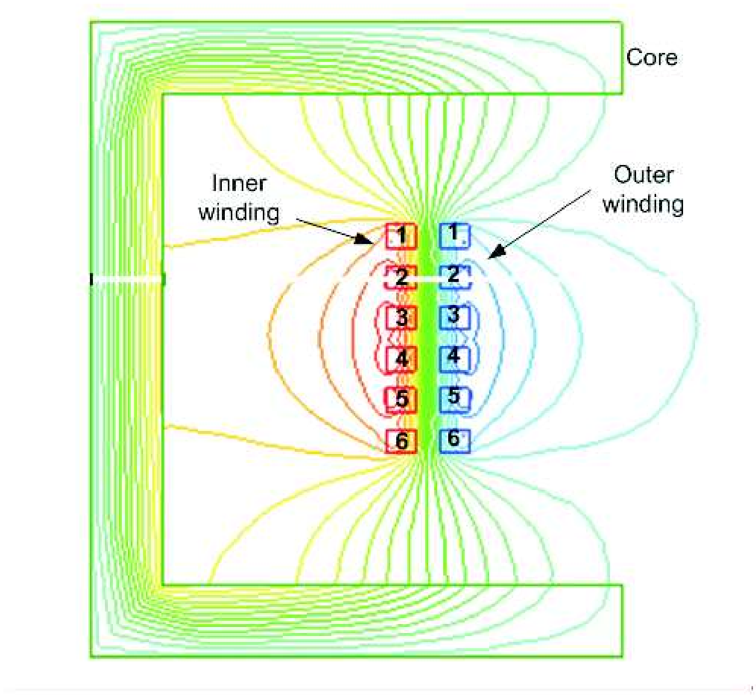

Figure 3.13: Magnetic field in the test transformer under short circuit conditions.

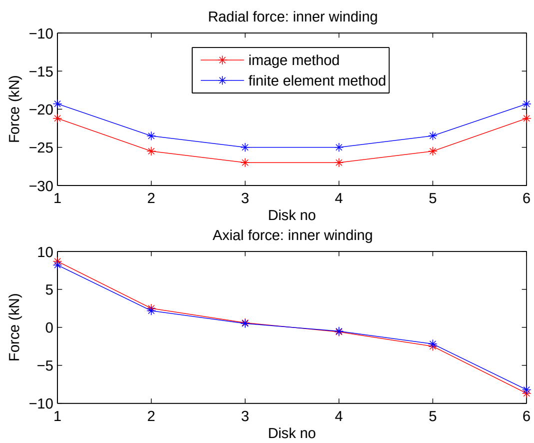

Figure 3.14: Comparison of results of discrete image method and Finite Element Method for inner winding.

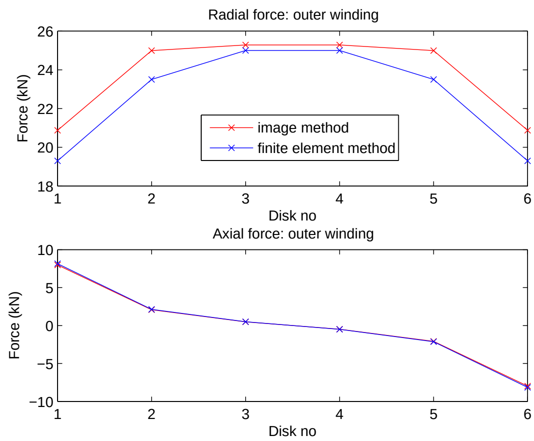

Figure 3.15: Comparison of results of discrete image method and Finite Element Method for outer winding.

3.7 Discussion

Although the Finite Element Method is a very accurate tool to calculate the electromagnetic forces, the time taken to draw a transformer geometry is very significant. Then the force on each element has to be calculated separately and the program has to be run as many times as the number of the elements. If the transformer winding arrangement is complex, the computation time can be extremely long.

The image method is also accurate and a fraction of time is consumed for both setup and computation when compared to the Finite Element Method. The results of force on each component are calculated simultaneously in the image method. Finite Element Method is more comprehensive because it takes non-linearity of iron into account. The accuracy of discrete image method can be improved by the addition of more images. However, for practical calculations, 10% discrepancy is not significant.

3.8 Conclusion

The image method is accurate and less time consuming than the Finite Element Method. It calculates the radial and axial forces simultaneously. Also the results can be programmed as a force vs time waveform which are required for the SIMULINK® model used to study the dynamic behaviour.

Chapter 4

Calculation of radial electromagnetic forces in concentric windings

4.1 Introduction

Radial forces in concentric windings of a two-winding transformer produce a hoop stress that tends to extend the radius of the outer winding and at the same time they produce a compressive stress in the inner winding producing buckling as shown in Chapter 2. In this chapter the methods of calculating the electromagnetic forces in the radial direction in a transformer with concentric windings are considered. Only the core type transformers with cylindrical windings are discussed here. However, these techniques can be applied to the other types of windings [Say, 1958; Franklin and Franklin, 1983; Waters, 1966].

4.2 Prediction of radial electromagnetic forces

The radial components of the forces in a transformer with concentric windings have never been considered significant due to the fact that radial strength of the winding is high. Although, radial buckling has been experienced in transformers, the general conception is that it can be avoided by a perfectly round winding cross-section and by adequate radial supports. The bulk of the previous research deals with the force calculation in the axial direction, since the vast majority of failures are due to axial forces. Also axial movement is more damaging to the winding and insulation structures than radial movements.

The methods available for the calculation of the radial forces range from the basic empirical methods to more sophisticated methods. The empirical methods are based on simplified assumptions. Corrections are added on the basis of experience or experimental results to reduce the inaccuracies. As a result, the radial forces can be easily and relatively accurately calculated by elementary methods especially when the maximum radial force is required. However, the more sophisticated methods like the two-dimensional image method and two or three dimensional Finite Element Methods are more accurate but require the use of a computer.

4.3 Elementary methods to calculate radial electromagnetic forces

The winding of a transformer can be represented in a two-dimensional geometry. Figure 4.1 shows a cross section of one side of the limb of a two-winding transformer. The outer winding lies in an axial field which causes a radial force acting outwards tending to stretch the conductor (producing a hoop stress), and the inner winding experiences a similar force acting inwards tending to crush or collapse it.

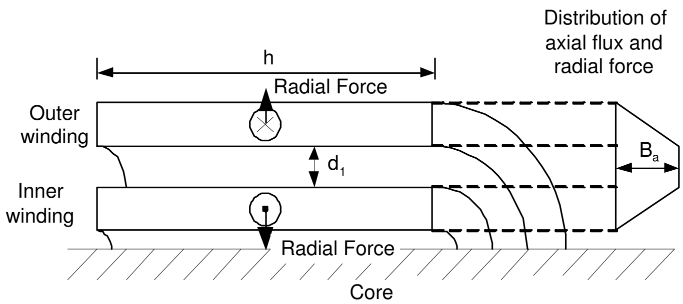

Figure 4.1: Two-dimension representation of concentric transformer windings for the calculation of radial electromagnetic forces showing axial flux and resulting radial force [Waters, 1966]

These radial forces are slightly less at the ends of the windings due to the curving of the magnetic flux, but the force per unit length of winding will be almost uniform over the greater part of the winding length and it can be accurately calculated at the middle of the winding. Since it is the maximum force which is important [Say, 1958; Franklin and Franklin, 1983; Waters, 1966], it is convenient to ignore the curvature of the field near the ends of the windings and assume the leakage field is uniform along the whole length and that the radial forces will also be the same at all points along the winding. The stresses calculated in this way will correspond to those in the middle 90% of the winding. The reduction that occurs near the ends to about half is of little practical importance [Waters, 1966].

4.4 Forces in the outer winding

Considering the simple two-dimensional picture of Fig 4.1, the axial flux density in the leakage duct is $\frac{4\pi\times10^{-7}(NI)}{h}$ T if (NI) is the instantaneous value of the ampere-turn in each winding and h is the length of the windings.

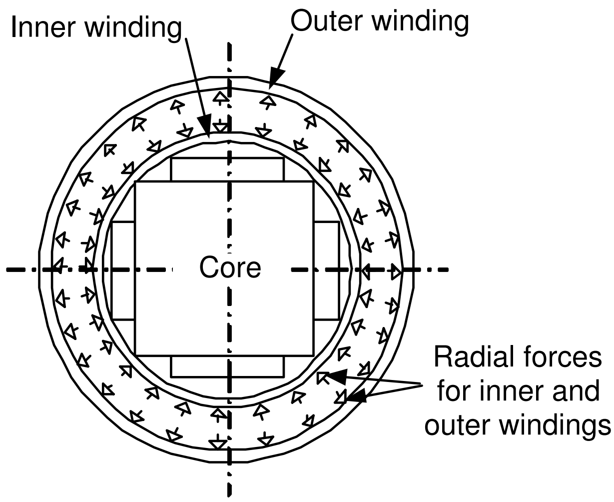

Figure 4.2: Radial electromagnetic forces in concentric transformer windings [Waters, 1966]

The method is based on the two-dimensional picture (Fig 4.1) of the magnetic field used for the reactance calculation [Waters, 1966; Franklin and Franklin, 1983]. The flux density decreases linearly from maximum value (in the duct) at the two surfaces of the duct to zero at the other surfaces of the windings as shown in the diagram at the right hand side of Fig 4.1. The radial force is produced by the average axial flux density in the winding which is equal to half of the duct flux density. This radial force acts radially outward as shown in Fig 4.2. The mean hoop stress in the outer winding can be calculated considering the winding as a thin cylinder shown in Fig 4.3. The transverse force in two opposite halves is equivalent to the pressure on the diameter [Waters, 1966; Franklin and Franklin, 1983], while the total force is the equivalent to the pressure upon the circumference πD_w where D_w is the diameter of the outer winding. This force acts on both ends of the diameter AB in Fig 4.3, i.e. on a cross sectional area of conductor equal to twice that of the whole winding.

The mean hoop stress σ_{mean} in the conductor of the outer winding at the peak of the first half cycle of short-circuit current, assuming an asymmetry factor of 1.8 [Franklin and Franklin, 1983; Waters, 1966] is,

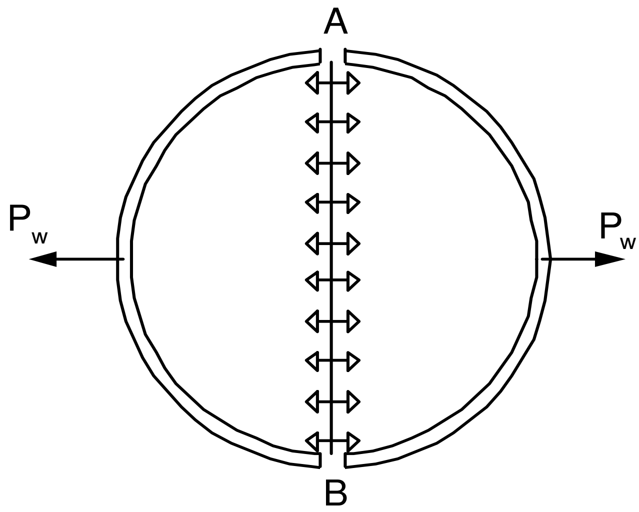

Figure 4.3: Mean hoop stress calculating method [Waters, 1966]

$$\sigma_{mean} = \frac{0.031 W_{cu}}{h e_z^2} \text{ kN/mm}^2 \text{ (peak)} \tag{4.1}$$

where W_{cu} = $I^2 R_{dc}$ loss in the winding in kW at rated full load at 75°C

h = axial height of the winding in mm

e_z = per unit impedance voltage

The inner winding tends to become crushed against the core and it is common practice to support the winding from the core and to treat the winding as a continuous beam with equidistant supports, ignoring the increase in strength due to curvature. The mean radial load per mm length of the conductor of the disk coil is (after [Franklin and Franklin, 1983]):

$$W = \frac{0.031 \sigma_{mean} A_c}{D_w} \text{ kN/mm length} \tag{4.2}$$

or alternatively

$$W = \frac{510 U \ X1}{e_z f d_1 \pi D_m N} \text{ kN/mm length} \tag{4.3}$$

where

$$\begin{aligned}
W_{cu} &= I^2R_{dc} \text{ loss in the winding in kW at rated full load at } 75^\circ\text{C} \\
h &= \text{axial height of the winding in mm} \\
A_c &= \text{cross-section of the conductor on which the force is to be determined, mm}^2 \\
D_w &= \text{mean diameter of the outer winding, mm} \\
U &= \text{rated kVA per limb} \\
f &= \text{frequency, Hz} \\
\sigma_{mean} &= \text{mean hoop stress at the peak of first half cycle, kN/mm}^2\text{, from equation 4.1} \\
d_1 &= \text{equivalent duct width, mm} \\
D_m &= \text{mean diameter of the transformer windings} \\
&\quad \text{(i.e. of HV and LV windings together), mm} \\
N &= \text{number of turns in the outer winding} \\
e_z &= \text{per unit impedance voltage}
\end{aligned}$$

Equation 4.3 gives a total force on 1mm length of the conductor occupying the full radial thickness of the winding. In a multilayer winding, with k layers, the value for the layer next to the duct would be $(2k-1)/k$ times this value, the second layer $(2k-3)/k$, and so on.

4.4.1 Hoop stress in disk windings

In the event of Hoop Stress in disc windings in a tightly wound disc coil, the inner turns cannot elongate without stressing those on the outside. The transfer of stress is considerable and instead of the stress varying from practically zero on the outside to twice the mean value on the inside, it becomes almost uniform with a maximum not much greater than the mean stress [Waters, 1966]. Alternatively, if the turns of a disc coil are free to slide, then the tension must be the same at all points and the hoop stress must be the same in all turns. Thus in an ordinary disc coil it is a reasonable assumption to use the mean hoop stress when considering the strength of the coil as a whole.

4.5 Forces on the inner winding

The inner winding is subjected to radial forces acting inwards as shown in Fig 4.2 and these may be calculated by using the mean diameter. However, the inner winding does not have a simple compressive stress equivalent to the hoop stress in the outer winding. The modes of the failure of the windings are either by collapsing, or if it is supported from the core, by bending between the supports.

If the inner winding is of the disk type then each disk is subjected to a radial force per mm of conductor,

$$p_r = \frac{2\ \sigma_{mean}\ n_c A_c}{D_w} \quad \text{kN/mm length} \tag{4.4}$$

where

$$\begin{aligned} \sigma_{mean} &= \text{mean stress calculated in Eq 4.1} \\ p_r &= \text{radial force per mm of conductor} \\ A_c &= \text{cross sectional area of each conductor mm}^2 \\ n_c &= \text{number of conductors in each disk} \\ D_w &= \text{mean diameter of the winding (inner and outer) mm} \end{aligned}$$

and the total radial force

$$P_{rw} = 2\pi\ \sigma_{mean}\ n_c A_c \quad \text{kN} \tag{4.5}$$

It is however difficult and tedious to predict the forces on each disk or turn separately to use in a mechanical behaviour study. On the other hand, sophisticated methods provide the solution of forces on individual turns/disks. These methods are rigorous and deal with axial and radial force calculation simultaneously and are discussed in Chapter 3.

4.6 Discussion

The methods discussed here are capable of calculating the cumulative radial force on each winding but are ineffective when the force on each disk is required for the dynamic behaviour study.

The Finite Element Method and Discrete Image Method, described in Chapter 3 are the accurate methods. The 'Image method with discrete conductors' is the method of choice for this work because of its ability to calculate both axial and radial forces simultaneously and accurately. The code developed with this method is given in Appendix A. The comparison of the results of 'Finite Element Method' and 'Image Method with Discrete Conductors' for radial forces of the test transformer are presented in Figures 4.4 and 4.5.

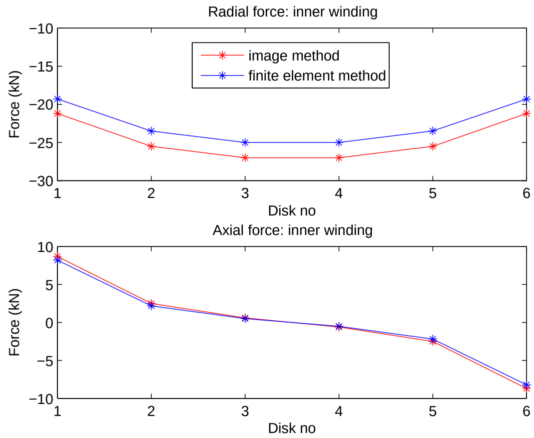

Figure 4.4: Comparison of results of discrete image method and finite element method for inner winding

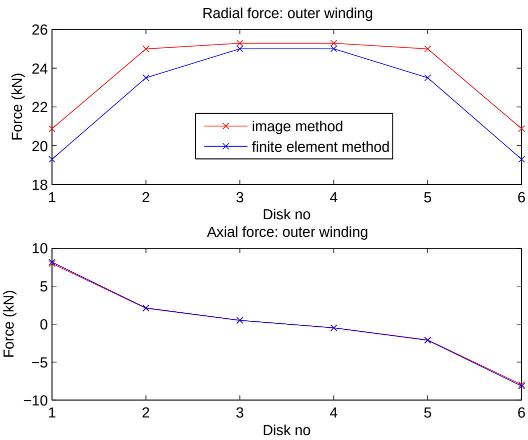

Figure 4.5: Comparison of results of discrete image method and finite element method for outer winding

4.7 Conclusion

The accuracy of the 'Image Method with Discrete Conductors' depends upon the number of radial images. The program written was able to calculate the forces on each disk which was required for the dynamic model of Chapter 8.

The discrepancy between discrete image method and FEM is not regarded as significant (Section 3.7, Chapter 3).

Chapter 5

Dynamic axial behaviour of transformer windings

5.1 Introduction

The mathematical models to study the dynamic axial behaviour of large power transformers have been available since the late 1950's and early 1960's. The models were simplified by suitable assumptions to reduce the complexity and time of computation. Most of the models assumed pressboard to behave as a linear spring [Tournier et al., 1964; J P Martin, 1980]. Patel [1972] assumed pressboard as a non-linear, unidirectional spring. The model of the pressboard was further improved by Swihart and McCormick [1980]. They developed a non-linear model including damping.

The axial model presented in this chapter, is similar to the models of previous researchers and has used a few assumptions to simplify the problem. The pressboard under dynamic load is treated as non-linear. The derivation of the mathematical equations of the model was carried out by assuming the spring constant as linear and the nonlinearity was then introduced by representing the spring characteristics as a lookup table. The implementation of the nonlinear model is given in Chapter 8. This model is an integral component in the construction of the combined model to study the behaviour of a transformer in reality.

5.2 Axial model of power transformer windings

The physical structure of the winding of a transformer consists of copper windings insulated with craft paper (wrapped) and pressboard (clacks) used in the radial and the axial directions respectively, as insulation and to accommodate the oil flow for cooling of the copper conductors. The winding is made on a pressboard cylinder (former) and the disks are supported radially by ribs as shown in Fig 5.1.

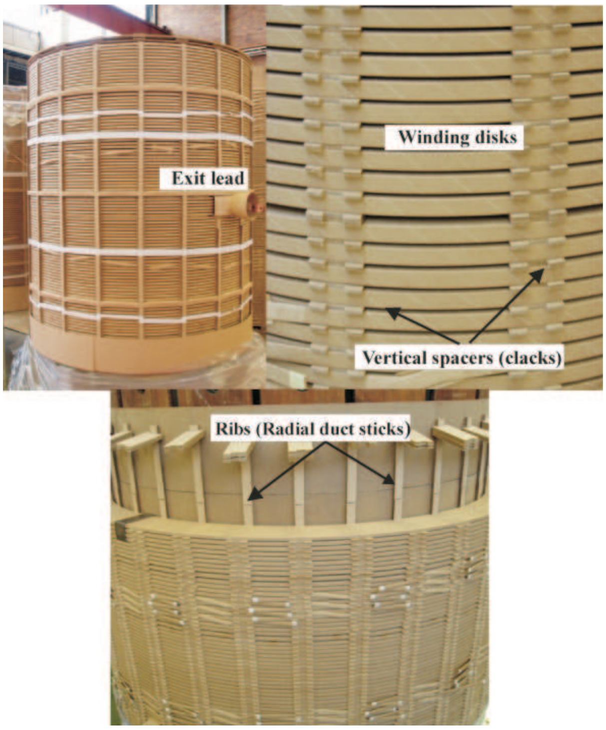

Figure 5.1: Physical construction of transformer winding. On the top left, a photo shows the full winding and the right is the magnified section of the winding showing axial spacers. The bottom section of photo shows the duct sticks (ribs).

The first comprehensive approach to model the axial behaviour of a transformer winding was suggested by Tournier et al. [1962a]. The model was based on the following assumptions.

- the mass of the winding was divided into a number of lumped masses (lumped masses were assumed rigid)
- the axial insulation between the turns/disks was also lumped

The mathematical model was a set of differential equations and had to be solved numerically. To reduce the time of computation, the number of the lumped masses was reduced to 11 as it produced the same values for the first few natural frequencies.

The spring constant and damping of the pressboard insulation were determined experimentally from the oscillograms of tests conducted on the transformer which showed very little damping in the insulation components.

In 1963 Watts [1963] made an improvement to Touriner's axial model by introducing the non-linear behaviour of pressboard. Watts's non-linear (VISCO-ELASTIC) model was further used by Patel [1973b, 1972], in his axial model of the transformer winding which was developed for a three phase transformer. This model included the effects of core clamps, tie rods and the response of the tank under short circuit conditions. The model was capable of including different pre-stress levels. He simplified the viscoelastic model to a two component model and further concluded that under short-circuit conditions there was no internal damping in the pressboard insulation.

The researchers [Madin and Whitaker, 1963a; Hiraishi, 1971; Ayres et al., 1975] produced similar axial models and tested them on full scale transformers.

Swihart and Wright [1976] did an extensive study in determining the physical properties of pressboard under different pre-stress levels and suggested a very complex model for the insulation. This model took into account the spring and damping characteristics of the pressboard. The measurements made by Swihart et al showed significant damping in the pressboard even after stabilization. The work also pointed out that the behaviour of pressboard under heavy dynamic loading was considerably different from that under lighter dynamic loads. Also there was a considerable difference between the dynamic and static characteristics of pressboard which was used in the earlier dynamic studies. Later, Hori et al [Hori and Okuyama, 1990] produced a two dimensional model based on the difference in applied electromagnetic force on a winding coil on the inside and outside of the core window.

5.3 Dynamic axial model

The axial model suggested in this work is similar to the previous models with a change to two separate windings as shown in Fig 5.2. The previous authors have lumped the pressboard vertical spacers, but in this study, each winding disk is assumed as a lumped mass and instead of combining the pressboard vertical spacers together in lumped springs, each vertical spacer (the insulation between each disk) is represented as a spring and a dashpot. The winding clamps are assumed rigid which is realistic because the copper winding and pressboard insulation are the weakest

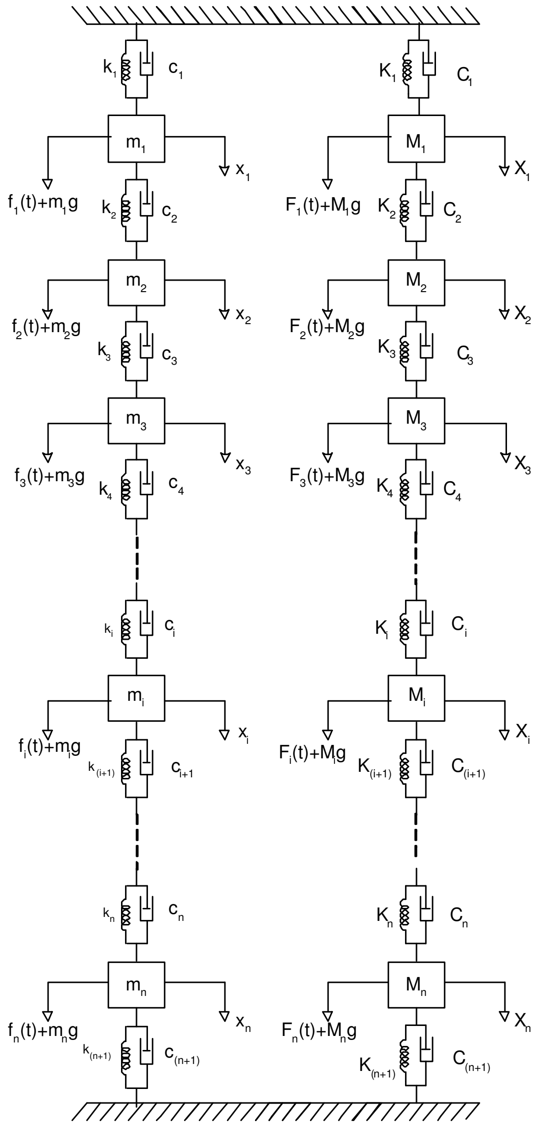

Figure 5.2: Lumped mass model of a two-winding transformer

parts and have significantly lower stiffness than the clamp and core structure. The top and bottom clamps are relatively heavier and stronger structures, joined with tie rods allowing little movement of the top and bottom yoke and core clamps.

The equation of motion of the spring-mass system of Fig 5.2 can be written by applying Newton's 2nd law of motion. The direction of force and resulting displacement are shown in Fig 5.2.

The equations of motion for lumped masses (winding disk) of the inner winding can be written as:

$$
\begin{aligned}
m_1\ddot{x}_1 + (c_1+c_2)\dot{x}_1 - c_2\dot{x}_2 + (k_1+k_2)x_1 - k_2x_2 &= f_1(t) + m_1g \\
m_2\ddot{x}_2 - c_2\dot{x}_1 + (c_2+c_3)\dot{x}_2 - c_3\dot{x}_3 - k_2x_1 + (k_2+k_3)x_2 - k_3x_3 &= f_2(t) + m_2g \\
\vdots \quad & \quad \vdots \\
m_i\ddot{x}_i - c_i\dot{x}_{i-1} + (c_i+c_{i+1})\dot{x}_i & \\
-c_{i+1}\,\dot{x}_{i+1} - k_ix_{i-1} + (k_i+k_{i+1})x_i - k_{i+1}\,x_{i+1} &= f_i(t) + m_ig \\
\vdots \quad & \quad \vdots \\
m_n\ddot{x}_n - c_{n-1}\dot{x}_{n-1} + (c_{n-1}+c_n)\dot{x}_n - k_{n-1}x_{n-1} + (k_{n-1}+k_n)x_n &= f_n(t) + m_ng
\end{aligned}
$$

Where:

x_i= local displacement of mass
c_i= is the damping coefficient
k_i= spring constant

The above equations can be written in matrix form

$$[\mathbf{m}]\ddot{\mathbf{x}}_{in} + [\mathbf{c}]\dot{\mathbf{x}}_{in} + [\mathbf{k}]\mathbf{x}_{in} = \mathbf{f}(t) + \mathbf{m}g \tag{5.1}$$

where $\mathbf{x}_{in}$= local displacement of disk of inner winding

$$
[\mathbf{m}] = \begin{bmatrix}
m_1 & 0 & 0 & 0 & 0 & \cdots \\
0 & m_2 & 0 & 0 & 0 & \cdots \\
0 & 0 & m_3 & 0 & 0 & \cdots \\
\vdots & & & \ddots & & \\
0 & \cdots & 0 & m_i & 0 & \cdots \\
\vdots & & & & \ddots & \\
0 & 0 & 0 & \cdots & 0 & m_n
\end{bmatrix}
\qquad \text{and} \qquad
[\mathbf{x}_{in}] = \begin{bmatrix} x_1 \\ x_2 \\ x_3 \\ \vdots \\ x_i \\ \vdots \\ x_n \end{bmatrix}
$$

and

$$
[\mathbf{c}] = \begin{bmatrix}
(c_1+c_2) & -c_2 & 0 & 0 & 0 & 0 & \cdots \\
-c_2 & (c_2+c_3) & -c_3 & 0 & 0 & 0 & \cdots \\
0 & -c_3 & (c_3+c_4) & -c_4 & 0 & 0 & \cdots \\
\vdots & & & & & & \\
0 & \cdots & -c_{i-1} & (c_{i-1}+c_i) & -ci & 0 & \cdots \\
\vdots & & & & & & \\
0 & 0 & \cdots & 0 & -c_{n-1} & & c_n
\end{bmatrix}
$$

also $[\mathbf{k}]$ can be represented as

$$
[\mathbf{k}] = \begin{bmatrix}
(k_1+k_2) & -k_2 & 0 & 0 & 0 & 0 & \cdots \\
-k_2 & (k_2+k_3) & -k_3 & 0 & 0 & 0 & \cdots \\
0 & -k_3 & (k_3+k_4) & -k_4 & 0 & 0 & \cdots \\
\vdots & & & & & & \\
0 & \cdots & -k_{i-1} & (k_{i-1}+k_i) & -k_i & 0 & \cdots \\
\vdots & & & & & & \\
0 & 0 & & \cdots & 0 & -k_n & k_{n+1}
\end{bmatrix}
$$

Similarly, the equation of motion for the outer winding can be written as:

$$[\mathbf{M}]\ddot{\mathbf{x}}_{ot} + [\mathbf{C}]\dot{\mathbf{x}}_{ot} + [\mathbf{K}]\ \mathbf{x}_{ot} = \mathbf{F}(t) + \mathbf{m}g \tag{5.2}$$

Here $\mathbf{x}_{ot}$ is the displacement of outer winding disks

Where $\mathbf{M}$, $\mathbf{C}$ and $\mathbf{K}$ are similar to the matrices $\mathbf{m}$, $\mathbf{c}$ and $\mathbf{k}$ respectively.
By combining Equations 5.1 and 5.2, the equation of axial motion becomes:

$$[\mathbf{M}_{ax}]\ddot{\mathbf{X}} + [\mathbf{C}_{ax}]\dot{\mathbf{X}} + \mathbf{K}_{ax}\mathbf{X} = \mathbf{F}_{ax}(t) + \mathbf{M}g \tag{5.3}$$

The combined displacement 'X' mass 'M_{ax}', damping 'C_{ax}' and stiffness 'K_{ax}' matrices can be obtained by combining the matrices of inner and outer windings.

$$[\mathbf{X}] = \begin{bmatrix} \mathbf{x}_{in} \\ \mathbf{x}_{ot} \end{bmatrix} \tag{5.4}$$

$$[\mathbf{M}_{ax}] = \begin{bmatrix} \mathbf{m} & 0 \\ 0 & \mathbf{M} \end{bmatrix} \tag{5.5}$$

Similarly the stiffness and damping matrices are represented as:

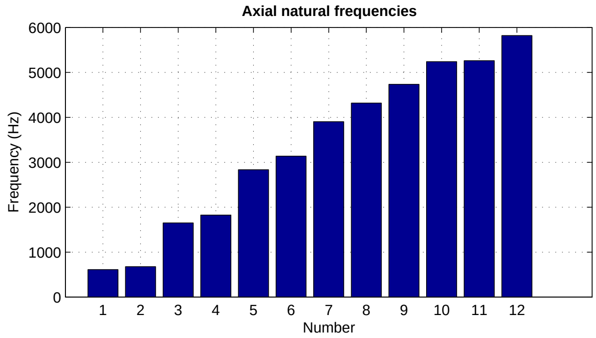

Figure 5.3: The natural frequencies of test transformer in axial direction

$$[\mathbf{K}_{ax}] = \begin{bmatrix} \mathbf{k} & 0 \\ 0 & \mathbf{K} \end{bmatrix} \tag{5.6}$$

$$[\mathbf{C}_{ax}] = \begin{bmatrix} \mathbf{c} & 0 \\ 0 & \mathbf{C} \end{bmatrix} \tag{5.7}$$

The applied electromagnetic force including the static gravitational force in matrix form is:

$$[\mathbf{F}_{ax}] = \begin{bmatrix} \boldsymbol{f}(t) + \boldsymbol{m}g \\ \boldsymbol{F}(t) + \boldsymbol{M}g \end{bmatrix} \tag{5.8}$$

$\mathbf{f}(t)$ and $\mathbf{F}(t)$ are applied electromagnetic forces on the inner and outer windings, $\mathbf{m}$ and $\mathbf{M}$ is the mass of each lumped mass of inner and outer windings respectively and g is the gravitational acceleration.

5.4 Implementation of model

MATLAB™ code was written to construct $\mathbf{X}$ $\mathbf{K}_{ax}$, and $\mathbf{M}_{ax}$ matrices and the natural frequencies were calculated as shown in Figure 5.3. The MATLAB™ code determines the inputs to the axial dynamic model implemented in SIMULINK®. The model implementation is given in Appendix B. The nonlinearity of the pressboard was included by using measured dynamic stress-strain characteristics which are discussed in Chapter 7.

5.5 Conclusion

The model is intended to calculate inputs which will be used in the study of axial and combined dynamic behaviour. The code based on the equations derived in this chapter was used to calculate the natural frequency of the test transformer in the axial direction.

The fundamental natural frequency of the test transformer is around 600 Hz which shows the axial stiffness of the transformer is very high resulting in a natural frequency far removed from the 100 Hz electromagnetic force frequency.

Chapter 6

Dynamic radial behaviour of transformer windings

6.1 Introduction

In early years, research into the dynamics of windings was limited to the axial behaviour of the windings. In the radial direction, the windings were assumed to be capable of withstanding the radial stresses due to the higher stiffness. In the recent past, it has been realized that the inner winding buckling goes unnoticed due to a lack of means of easy visual inspection. Some electrical techniques have been available and applied but they fail to detect the deformation, especially when the relative deformation of the windings is small. Many indirect methods (Sweep Frequency Response etc) have been developed to assess the deformation by measurement but none of them are either consistent or accurate.

This chapter presents the equations governing the dynamic radial behaviour of a two concentric windings transformer. The interaction of radial and axial behaviour under dynamic conditions will be discussed in Chapter 8.

6.2 Radial behaviour of windings

In 1971 Hiraishi [1971] conducted experimental work to investigate the radial and axial behaviour of transformer windings. In this work, the vibration characteristics of the winding and natural frequencies were determined experimentally. The effects of the natural frequency on the buckling strength were also explored. He derived equations for the calculation of the buckling strength and plastic deformation under static conditions. The radial deformation was further studied by Ayres et al. [1975]. Saravolac et al. using a static approach for radial strength based on Timoshenko's formula for the critical load of a hinged arch [Saravolac et al., 2000]. They also conducted experiments to understand the withstand capabilities of different types of windings under uniform forces in the radial direction.

6.3 Radial model of a two-winding transformer

Consider a two-winding transformer with both inner and outer windings having the same voltage and current. The windings are disk type as shown in Fig 6.1. The radial behaviour of the windings can be investigated by considering both windings as concentric elastic rings coupled with springs and dashpots (insulation ribs) as shown in Fig 6.4. Although copper is not linearly elastic, the assumption that copper rings are elastic is realistic under small displacements. The assumption is more applicable for the copper used in modern windings which is cold worked and can have an elasticity of 1.4×10^{10} P and even higher. The vibration of these rings under a periodic force excitation can be of the following types [Timoshenko et al., 1974].

- extensional vibration with a periodic change in the radius of the ring (Figure 6.3)
- flexural vibration in the plane of the ring
- flexural vibration involving the displacements at right angles, out of the plane of the ring
- twist

For the inner winding, consider the flexural vibration in the plane of the ring [Timoshenko et al., 1974] of radius r. Figure 6.2 shows the angle θ representing the angular coordinates of the radial displacement, u is the radial displacement (positive outward) and v is the tangential displacement (positive in anti clockwise direction). Similarly for the outer winding, R is the radius, U and V are the radial and tangential displacements respectively and will be used further in this chapter.

Due to the displacements u and v, the unit elongation of the center line of the ring at any point is represented as [Timoshenko et al., 1974].

$$e = \frac{u}{r} + \frac{\partial v}{r\partial\theta} \tag{6.1}$$

For the general case of flexural vibrations in the plane of the ring the radial displacement u can be expanded in the form of a trigonometric series [Timoshenko et al.,

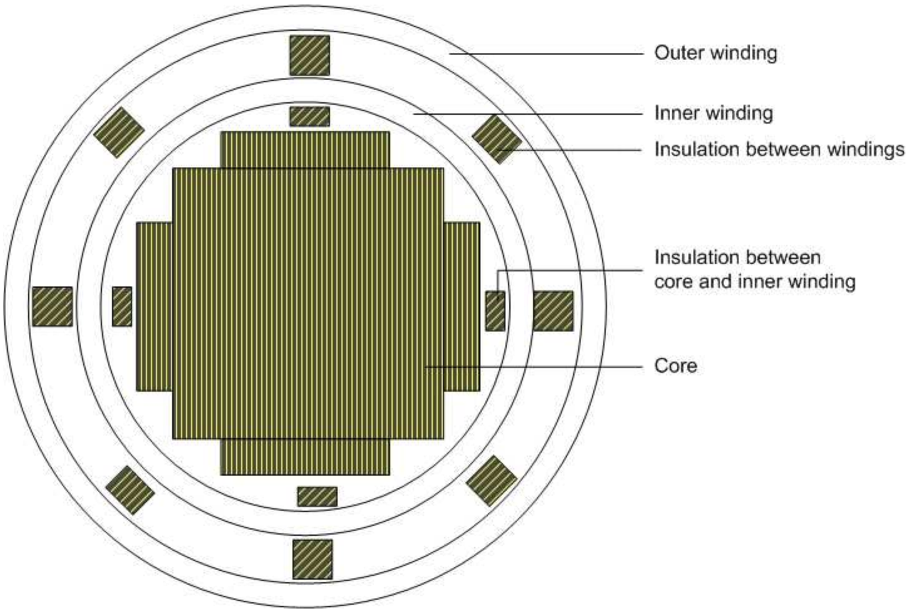

Figure 6.1: Cross-sectional view of a transformer winding

1974] as given in Equation 6.2,

$$u = a_o + a_1 \cos\theta + b_1 \sin\theta + a_2 \cos 2\theta + b_2 \sin 2\theta + a_3 \cos 3\theta + b_3 \sin 3\theta + \cdots \quad (6.2)$$

where $a_1, a_2, \ldots, b_1, b_2, \ldots$ are the generalized displacements and are functions of time. However a_o represents pure uniform radial displacement represented by a constant term. The trigonometric terms $cos\theta$ and $sin\theta$ of Equation 6.2 show the influence of radial position. For pure flexural vibration without any radial extension, the elongation e in Equation 6.1 is 0.

$$u = -\frac{\partial v}{\partial \theta} \quad (6.3)$$

and the circumferential displacement of the ring can be represented as

$$v = -\int u d\theta \quad (6.4)$$

by integrating u and multiplying by -1, results in

$$v = 0 - a_1 \sin\theta + b_1 \cos\theta - \frac{1}{2}\, a_2 \sin 2\theta + \frac{1}{2}\, b_2 \cos 2\theta - \frac{1}{3}\, a_3 \sin 3\theta + \frac{1}{3}\, b_3 \cos 3\theta - \ldots \quad (6.5)$$

The term a_o represents 'breathing' motion of the ring with no circumferential displacement and hence in Equation 6.5 is regarded as 0.

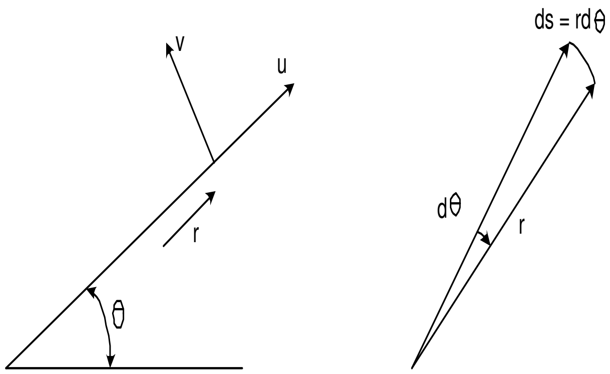

Figure 6.2: Radial and circumferential displacements, u and v the inner winding ring.

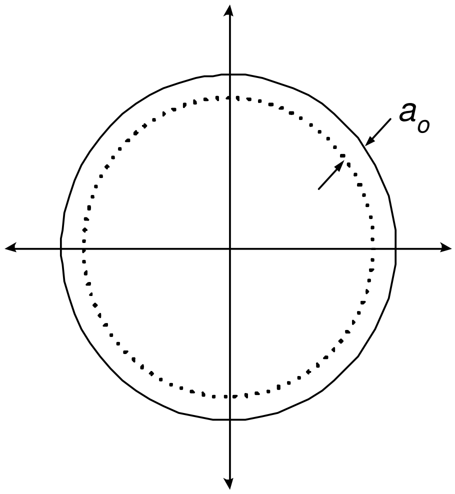

Figure 6.3: Simplest mode of vibration 'breathing motion' uniform radial expansion and contraction

Equation 6.2 can be resolved in vector form, if

$$\mathbf{q} = \begin{bmatrix} a_o \\ a_1 \\ b_1 \\ a_2 \\ b_2 \\ a_3 \\ b_3 \\ \vdots \end{bmatrix} \tag{6.6}$$

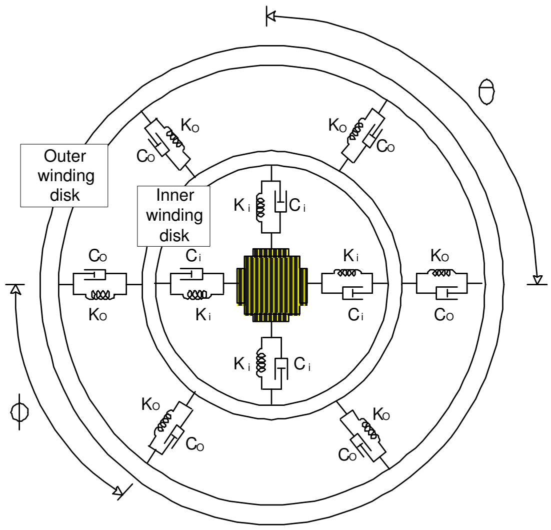

Figure 6.4: Inner and outer winding represented as elastic rings coupled with springs and dashpots

Where '**q**' represents the general coordinates in a vector format and the angular coordinates in vector form are represented as '$\boldsymbol{\phi}_u$'

$$\boldsymbol{\phi}_u = \begin{bmatrix} 1 \\ \cos\theta \\ \sin\theta \\ \cos 2\theta \\ \sin 2\theta \\ \cos 3\theta \\ \sin 3\theta \\ \vdots \end{bmatrix} \tag{6.7}$$

Similarly 'v' can also be represented in vector form of '**q**' and '$\boldsymbol{\phi}_v$'. Where $\boldsymbol{\phi}_v$ is the angular vector given as,

$$\boldsymbol{\phi}_v = \begin{bmatrix} 0 \\ -\sin\theta \\ \cos\theta \\ -\frac{1}{2}\sin 2\theta \\ \frac{1}{2}\cos 2\theta \\ -\frac{1}{3}\sin 3\theta \\ \frac{1}{3}\cos 3\theta \\ \vdots \end{bmatrix} \tag{6.8}$$

Equation 6.2 can be written in matrix form,

$$u = \mathbf{q}^T [\boldsymbol{\phi}_u] = [\boldsymbol{\phi}_u]^T \mathbf{q} \tag{6.9}$$

Similarly, the equation of v can also be represented in matrix format as,

$$v = \mathbf{q}^T [\boldsymbol{\phi}_v] = [\boldsymbol{\phi}_v]^T \mathbf{q} \tag{6.10}$$

6.4 Kinetic energy of inner and outer disks

The kinetic energy of the vibrating inner and outer rings is of two types, the kinetic energy due to simple extensional vibration (Fig 6.3) and the flexural kinetic energy which can be represented as [Timoshenko et al., 1974],

$$T = \frac{\rho A}{2}\ \dot{u}^2\ 2\pi r \tag{6.11}$$

Where:

T	=	kinetic energy of a ring due to flexural vibration
A	=	cross-sectional area of the ring
ρ	=	mass density
r	=	radius of the ring
$\dot{u}$	=	$\frac{du}{dt}$, velocity in the radial direction

The rings have radial and tangential movements. Hence the total velocity of the ring includes the radial and tangential velocity $\dot{u}$ and $\dot{v}$. Therefore, the kinetic energy of the inner ring due to radial and tangential motion is given in the following equation.

$$T^i = \frac{1}{2}\rho A_i \int_0^{2\pi} \left(\dot{u}^2 + \dot{v}^2\right)\ r d\theta \tag{6.12}$$

The total kinetic energy of the inner and outer winding rings due to the flexural vibration can be represented as,

$$\begin{aligned} T &= T^i + T^o \\ T^i + T^o &= \frac{\rho A_i}{2}\int_0^{2\pi}(\dot{u}^2 + \dot{v}^2) r d\theta + \frac{\rho A_o}{2}\int_0^{2\pi}(\dot{U}^2 + \dot{V}^2) R d\theta \end{aligned} \tag{6.13}$$

Where

T^i = Kinetic energy of the inner ring

T^o = Kinetic Energy of the outer ring

ρ = the mass density of winding ring

A_i, A_o = are the cross-sectional areas of inner and outer winding rings respectively

U, V =are the radial and tangential displacements of the outer winding and

u, v = are the radial and tangential displacements of the inner ring as shown in Figure 6.2.

To calculate the kinetic energy 'T^i' for the inner winding ring,

$$\begin{aligned} \dot{u} &= \dot{\mathbf{q}}^T \boldsymbol{\phi_u} \\ \text{and} \quad \dot{u}^2 &= \dot{\mathbf{q}}^T \boldsymbol{\phi_u} \ \ \boldsymbol{\phi_u}^T \dot{\mathbf{q}} \end{aligned}$$

similarly $\dot{v}^2$ is

$$\dot{v}^2 = \dot{\mathbf{q}}^T \boldsymbol{\phi}_v \ \ \boldsymbol{\phi}_v{}^T \dot{\mathbf{q}} \tag{6.14}$$

Recalling '$\mathbf{q}$' is a function of time and is independent of θ.

hence

$$\left(\dot{u}^2 + \dot{v}^2\right) = \dot{\mathbf{q}}^T \boldsymbol{\phi}_u \ \ \boldsymbol{\phi}_u{}^T \dot{\mathbf{q}} + \dot{\mathbf{q}}^T \boldsymbol{\phi}_v \ \ \boldsymbol{\phi}_v{}^T \dot{\mathbf{q}} \tag{6.15}$$

and can be represented as

$$= \dot{\mathbf{q}}^T \left(\boldsymbol{\phi}_u \ \ \boldsymbol{\phi}_u^T + \boldsymbol{\phi}_v \ \ \boldsymbol{\phi}_v^T\right) \dot{\mathbf{q}} \tag{6.16}$$

Integrating both sides of Equation 6.16 w.r.t θ,

$$\int_0^{2\pi} \left(\dot{u}^2 + \dot{v}^2\right) d\theta = \dot{\mathbf{q}}^T \left(\int_0^{2\pi} \boldsymbol{\phi}_u \boldsymbol{\phi}_u^T d\theta\right) \ \dot{\mathbf{q}} + \dot{\mathbf{q}}^T \left(\int_0^{2\pi} \boldsymbol{\phi}_v \boldsymbol{\phi}_v^T d\theta\right) \ \dot{\mathbf{q}} \tag{6.17}$$

To evaluate the expression given in Equation 6.17, as a first step, the vectors $\boldsymbol{\phi}_u$ and $\boldsymbol{\phi}_u^T$ are required to be multiplied. Hence multiplying $\boldsymbol{\phi}_u$ and $\boldsymbol{\phi}_u^T$,

$$\boldsymbol{\phi}_u \boldsymbol{\phi}_u^T = \begin{bmatrix} 1 & \cos\theta & \sin\theta & \cos 2\theta & \sin 3\theta & \cdots \\ \cos\theta & \cos^2\theta & \cos\theta\sin\theta & \cos\theta\cos 2\theta & \cos\theta\sin 2\theta & \cdots \\ \sin\theta & \sin\theta\cos\theta & \sin^2\theta & \sin\theta\cos 2\theta & \sin\theta\sin 2\theta & \cdots \\ \cos 2\theta & \cos 2\theta\cos\theta & \cos 2\theta\sin\theta & \cos^2 2\theta & \cos 2\theta\sin 2\theta & \cdots \\ \sin 2\theta & \sin 2\theta\cos\theta & \sin 2\theta\sin\theta & \sin 2\theta\cos 2\theta & \sin^2 2\theta & \cdots \\ \vdots & \vdots & \vdots & \vdots & & \ddots \end{bmatrix} \tag{6.18}$$

Similarly $\boldsymbol{\phi}_v$ and $\boldsymbol{\phi}_v^T$ result in the following matrix.

$$\boldsymbol{\phi}_v\boldsymbol{\phi}_v^T = \begin{bmatrix} 0 & 0 & 0 & 0 & 0 & \cdots \\ 0 & \sin^2\theta & -\sin\theta\cos\theta & \frac{1}{2}\sin\theta\sin 2\theta & -\frac{1}{2}\sin\theta\cos 2\theta & \cdots \\ 0 & -\cos\theta\sin\theta & \cos^2\theta & -\frac{1}{2}\cos\theta\sin 2\theta & \frac{1}{2}\cos\theta\cos 2\theta & \cdots \\ 0 & \frac{1}{2}\sin 2\theta\sin\theta & \frac{1}{2}\sin 2\theta\cos\theta & \frac{1}{4}\sin^2 2\theta & -\frac{1}{4}\sin 2\theta\cos 2\theta & \cdots \\ 0 & -\frac{1}{2}\cos 2\theta\sin\theta & \frac{1}{2}\cos 2\theta\cos\theta & -\frac{1}{4}\cos 2\theta\sin 2\theta & \frac{1}{4}\cos^2 2\theta & \cdots \\ \vdots & \vdots & \vdots & \vdots & & \ddots \end{bmatrix} \tag{6.19}$$

Integrating Equations 6.18 and 6.19 and using the following formulae

$$\begin{aligned} \int_0^{2\pi} \cos^2 m\theta \; d\theta &= \pi \\ \int_0^{2\pi} \sin^2 m\theta \; d\theta &= \pi \\ \int_0^{2\pi} \cos m\theta \sin n\theta \; d\theta &= 0 \\ \int_0^{2\pi} \cos n\theta \sin m\theta \; d\theta &= 0 \\ \int_0^{2\pi} \cos m\theta \cos n\theta \; d\theta &= 0 \\ \int_0^{2\pi} \sin m\theta \sin n\theta \; d\theta &= 0 \end{aligned} \tag{6.20}$$

the results of the integrals in expanded form can be represented as,

$$\int_0^{2\pi} \boldsymbol{\phi}_u\boldsymbol{\phi}_u^T d\theta = \begin{bmatrix} 2\pi & 0 & 0 & 0 & 0 & 0 & \cdots \\ 0 & \pi & 0 & 0 & 0 & 0 & \cdots \\ 0 & 0 & \pi & 0 & 0 & 0 & \cdots \\ 0 & 0 & 0 & \pi & 0 & 0 & \cdots \\ 0 & 0 & 0 & 0 & \pi & 0 & \cdots \\ 0 & 0 & 0 & 0 & 0 & \pi & \cdots \\ \vdots & \vdots & \vdots & \vdots & \vdots & & \ddots \end{bmatrix} \tag{6.21}$$

and

$$\int_0^{2\pi} \boldsymbol{\phi}_v \boldsymbol{\phi}_v^T d\theta = \begin{bmatrix} 0 & 0 & 0 & 0 & 0 & 0 & 0 & \cdots \\ 0 & (\frac{1}{1})^2\pi & 0 & 0 & 0 & 0 & 0 & \cdots \\ 0 & 0 & (\frac{1}{1})^2\pi & 0 & 0 & 0 & 0 & \cdots \\ 0 & 0 & 0 & (\frac{1}{2})^2\pi & 0 & 0 & 0 & \cdots \\ 0 & 0 & 0 & 0 & (\frac{1}{2})^2\pi & 0 & 0 & \cdots \\ 0 & 0 & 0 & 0 & 0 & (\frac{1}{3})^2\pi & 0 & \cdots \\ 0 & 0 & 0 & 0 & 0 & 0 & (\frac{1}{3})^2\pi & \cdots \\ \vdots & \vdots & \vdots & \vdots & \vdots & \vdots & \vdots & \ddots \end{bmatrix} \tag{6.22}$$

Adding Equations 6.21 and 6.22

$$\int_0^{2\pi} (\dot{u}^2 + \dot{v}^2)\ d\theta = \dot{\mathbf{q}} \begin{bmatrix} 2\pi & 0 & 0 & 0 & 0 & 0 & \cdots \\ 0 & 2\pi & 0 & 0 & 0 & 0 & \cdots \\ 0 & 0 & 2\pi & 0 & 0 & 0 & \cdots \\ 0 & 0 & 0 & \frac{5}{4}\pi & 0 & 0 & \cdots \\ 0 & 0 & 0 & 0 & \frac{5}{4}\pi & 0 & \cdots \\ 0 & 0 & 0 & 0 & 0 & \frac{10}{9}\pi & \cdots \\ \vdots & \vdots & \vdots & \vdots & \vdots & \vdots & \ddots \end{bmatrix} \dot{\mathbf{q}}^T \tag{6.23}$$

By replacing the diagonal matrix of Equation 6.23 with $\mathbf{H}$.

$$\int_0^{2\pi} (\dot{u}^2 + \dot{v}^2)\ d\theta = \dot{\mathbf{q}}\ \ \mathbf{H}\ \dot{\mathbf{q}}^T \tag{6.24}$$

Hence, the total kinetic energy for the inner ring can be represented by Equation 6.25

$$T^i = \dot{\mathbf{q}}_i{}^T \left(\frac{\rho A_i r}{2} \mathbf{H} \right) \dot{\mathbf{q}}_i \tag{6.25}$$

Similarly the total kinetic energy T_o of outer ring is given by Equation 6.26

$$T^o = \dot{\mathbf{q}}_o^T \left(\frac{\rho A_o R}{2}\ \mathbf{H} \right) \dot{\mathbf{q}}_o \tag{6.26}$$

In Equations 6.25 and 6.26, the A_i and A_o are the areas of cross-section, and r and R are radii of inner and outer winding rings respectively. In Equations 6.25 and 6.26, the $\mathbf{q}_i$ and $\mathbf{q}_o$ are the generalized coordinates (function of time) of inner and outer rings.

The total kinetic energy T of the system is obtained by adding the kinetic energy of the inner ring and the outer ring and is given in Equation 6.27.

$$T = T^i + T^o = \frac{1}{2}\,\dot{\mathbf{q}}_i{}^T \underbrace{(\rho A_i r \mathbf{H})}_{\mathbf{M}_{in}} \dot{\mathbf{q}}_i + \frac{1}{2}\,\dot{\mathbf{q}}_o{}^T \underbrace{(\rho A_o R \mathbf{H})}_{\mathbf{M}_{ot}} \dot{\mathbf{q}}_o \tag{6.27}$$

To simplify Equation 6.27 the expressions $\rho A_i r\mathbf{H}$ and $\rho A_o R\mathbf{H}$ are replaced by $\mathbf{M}_{in}$ and $\mathbf{M}_{ot}$. Where $\mathbf{M}_{in}$ and $\mathbf{M}_{ot}$ are the mass matrices of inner and outer rings respectively.

$$T = \frac{1}{2}\,\dot{\mathbf{q}}_i^T \mathbf{M}_{in}\,\dot{\mathbf{q}}_i + \frac{1}{2}\,\dot{\mathbf{q}}_o{}^T \mathbf{M}_{ot}\,\dot{\mathbf{q}}_o \tag{6.28}$$

Hence, the total kinetic energy for both inner and outer rings in matrix form can be represented as,

$$T = \frac{1}{2}\,\dot{\mathbf{Q}}^T \begin{bmatrix} \mathbf{M}_{in} & \mathrm{O} \\ \mathrm{O} & \mathbf{M}_{ot} \end{bmatrix} \dot{\mathbf{Q}} \tag{6.29}$$

$$\mathbf{Q} = \begin{bmatrix} \mathbf{q}_i \\ \mathbf{q}_o \end{bmatrix} = \begin{bmatrix} a_o \\ a_1 \\ b_1 \\ a_2 \\ b_2 \\ \vdots \\ A_0 \\ A_1 \\ B_1 \\ A_2 \\ B_2 \\ \vdots \end{bmatrix} \tag{6.30}$$

Where Q is a vector consisting of the generalized coordinates of the inner and outer rings.

Equation 6.29 has the basic form of the kinetic energy equation $\left(T = \frac{1}{2}\,mv^2\right)$ and the diagonal matrix in the equation is the mass matrix and can be replaced with the symbol $\mathbf{M}_r$. Where $\mathbf{M}_r$ is the mass matrix of the inner and outer springs.

$$\mathbf{M}_r = \begin{bmatrix} \mathbf{M}_{in} & \mathrm{O} \\ & \\ \mathrm{O} & \mathbf{M}_{ot} \end{bmatrix} \tag{6.31}$$

The equation of the kinetic energy can be written in general format as

$$T = \frac{1}{2}\,\dot{\mathbf{Q}}^T\,\mathbf{M}_r\,\dot{\mathbf{Q}} \tag{6.32}$$

$\mathbf{M}_r$ is mass matrix and will used in the study of the radial dynamic behaviour of the windings.

6.5 Strain (potential) energy

The potential energy (PE) is the energy stored in the system due to dynamic conditions. This is the sum of potential energies stored by different components due to their behaviour. The energy stored in the copper rings is due to their elastic behaviour and potential energy stored in the insulation ribs depends upon the stress-strain characteristics of pressboard. The total potential energy can be represented as

$$E_p = E_p^i + E_p^o + E_{p-ins}^i + E_{p-ins}^o \tag{6.33}$$

Where

E_p = total potential energy

E_p^i = potential energy of inner ring

E_p^o = potential energy of outer ring

E_{p-ins}^i = potential energy of inner insulation ribs (between core and inner winding)

E_{p-ins}^o = potential energy of outer insulation ribs (between inner and outer winding)

6.5.1 Potential energy of copper rings

The PE due to elastic behaviour of copper rings can be calculated as given by Timoshenko et al., [1974]. Timoshenko's formula is given in Equation 6.34.

$$E_p^i = \frac{\varepsilon I_i}{2r^4}\int_0^{2\pi}\left(\frac{\partial^2 u}{\partial \theta^2} + u\right)^2 r d\theta \tag{6.34}$$

Where ε is the elasticity of the copper, I_i is the moment of inertia of the inner ring, r is the radius of the inner winding and u is the displacement of the ring in the radial direction under flexural vibration as defined in Figure 6.2.

From Equation 6.9, u is given as

$$u = \mathbf{q}_i^T \boldsymbol{\phi}_u \tag{6.35}$$

Differentiating both sides with respect to θ

$$\frac{\partial u}{\partial \theta} = \mathbf{q}_i^T \boldsymbol{\phi}'_u \tag{6.36}$$

Where $\boldsymbol{\phi}'$ is the derivative of $\boldsymbol{\phi}$ with respect to θ.

Differentiating both sides of Equation 6.36 with respect to θ again

$$\frac{\partial^2 u}{\partial \theta^2} = \mathbf{q}_i^T \boldsymbol{\phi}''_u \tag{6.37}$$

Differentiating the matrix $\boldsymbol{\phi}_u$ twice w.r.t θ gives the following expressions.

$$\boldsymbol{\phi}'_u = \begin{bmatrix} 0 \\ -\ \sin\theta \\ \cos\theta \\ -2\sin 2\theta \\ 2\cos 2\theta \\ -3\sin 3\theta \\ 3\cos 3\theta \\ \vdots \end{bmatrix} \qquad \text{and} \qquad \boldsymbol{\phi}''_u = \begin{bmatrix} 0 \\ -\ \cos\theta \\ -\ \sin\theta \\ -4\cos 2\theta \\ -4\sin 2\theta \\ -9\cos\theta \\ -9\sin\theta \\ \vdots \end{bmatrix}$$

Adding $\boldsymbol{\phi}_u''$ and $\boldsymbol{\phi}_u$

$$(\boldsymbol{\phi}_u'' + \boldsymbol{\phi}_u) = \begin{bmatrix} 1 \\ 0 \\ 0 \\ -3\cos 2\theta \\ -3\sin 2\theta \\ -8\cos\theta \\ -8\sin\theta \\ \vdots \end{bmatrix} \tag{6.38}$$

Therefore

$$\left(\frac{\partial^2 u}{\partial \theta^2} + u\right) = \mathbf{q}_i^T \left(\boldsymbol{\phi}_u{}'' + \boldsymbol{\phi}_u\right) = \mathbf{q}_i^T \begin{bmatrix} 1 \\ 0 \\ 0 \\ -3\cos 2\theta \\ -3\sin 2\theta \\ -8\cos\theta \\ -8\sin\theta \\ \vdots \end{bmatrix} \tag{6.39}$$

Hence Equation 6.39, can be written as

$$\begin{aligned} \frac{\partial^2 u}{\partial \theta^2} + u &= \mathbf{q}_i^T \boldsymbol{\phi}_u'' + \mathbf{q}_i^T \boldsymbol{\phi}_u \\ &= \mathbf{q}_i^T \underbrace{(\boldsymbol{\phi}_u'' + \boldsymbol{\phi}_u)}_{\mathbf{D}} \\ &= \mathbf{q}_i^T \mathbf{D} \end{aligned} \tag{6.40}$$

In the above equations for simplification the vector $\left(\boldsymbol{\phi}_u'' + \boldsymbol{\phi}_u\right)$ is replaced with $\mathbf{D}$ which is related to the elastic behaviour of copper rings.

Squaring both sides of Equation 6.40

$$\begin{aligned} \left(\frac{\partial^2 u}{\partial \theta^2} + u\right)^2 &= \\ &= \mathbf{q}_i^T \; \mathbf{D}\mathbf{D}^T \; \mathbf{q}_i \\ &= \mathbf{q}_i^T \begin{bmatrix} 1 & 0 & 0 & -3\cos 2\theta & -3\sin 2\theta & \cdots \\ 0 & 0 & 0 & 0 & 0 & \cdots \\ 0 & 0 & 0 & 0 & 0 & \cdots \\ -3\cos 2\theta & 0 & 0 & 9\cos^2 2\theta & 9\cos 2\theta\sin 2\theta & \cdots \\ -3\sin 2\theta & 0 & 0 & 9\sin 2\theta\,\cos 2\theta & 9\sin^2 2\theta & \cdots \\ \vdots & \vdots & \vdots & \vdots & \vdots & \ddots \end{bmatrix} \mathbf{q}_i \end{aligned} \tag{6.41}$$

Integrating both sides and by using the formulae given in 6.20

$$\int_0^{2\pi}\left(\frac{\partial^2 u}{\partial\theta^2}+u\right)^2 d\theta \quad = \quad \mathbf{q}_i^T \begin{bmatrix} E_{P_{ec}} & 0 & 0 & 0 & 0 & 0 & 0 & \cdots \\ 0 & 0 & 0 & 0 & 0 & 0 & 0 & \cdots \\ 0 & 0 & 0 & 0 & 0 & 0 & 0 & \cdots \\ 0 & 0 & 0 & 9\pi & 0 & 0 & 0 & \cdots \\ 0 & 0 & 0 & 0 & 9\pi & 0 & 0 & \cdots \\ 0 & 0 & 0 & 0 & 0 & 64\pi & 0 & \cdots \\ 0 & 0 & 0 & 0 & 0 & 0 & 64\pi & \cdots \\ \vdots & \vdots & \vdots & \vdots & \vdots & \vdots & \vdots & \ddots \end{bmatrix} \mathbf{q}_i \tag{6.42}$$

The first element of the diagonal matrix of equation 6.42 ($E_{P_{ec}}$) represents the extension/compression mode of vibration when the central line of the ring forms a circle of uniformly varying radius, and all cross sections move radially without rotation (Fig 6.1). If u is the radial displacement (positive outward) of any point on the ring of radius r. Then the unit elongation of the ring in the circumferential direction (extensional strain) is equal to ($\frac{u}{r}$). The potential energy (which in this case is the energy of simple tension) is given by the Equation 6.43, where A is the cross-sectional area of the ring [Timoshenko et al., 1974]. Hence E_{Pec} is to be replaced by the value given by the Equation 6.43.

$$E_{P_{ec}} = \frac{A\varepsilon u^2}{2r^2}2\pi r \tag{6.43}$$

By replacing the diagonal matrix of Equation 6.42 with $\mathbf{K}_{el}$, the potential energy stored in the inner ring due to its elastic behaviour can be represented as

$$E_P^i = \mathbf{q}_i^T \left(\frac{\varepsilon I_i}{2r^3}\,\mathbf{K}_{el}\right)\mathbf{q}_i \tag{6.44}$$

Similarly the elastic potential energy of the outer ring

$$E_p^o = \mathbf{q}_o^T \left(\frac{\varepsilon I_o}{2R^3}\,\mathbf{K}_{el}\right)\mathbf{q}_o \tag{6.45}$$

This potential energy is due to the elastic behaviour of the copper rings for the inner and outer windings and will be used to calculate the total potential energy of the two ring system coupled with pressboard insulation ribs (radial spacers).

6.5.2 Potential energy (PE) stored in pressboard ribs (radial spacers)

The ribs or radial spacers are the components connecting the inner ring to the core and to the outer copper ring. These ribs are normally made of pressboard material and support the windings in the radial direction on the core.

The potential energy stored in insulation ribs can be calculated by assuming a spring connecting the inner side of elastic copper ring to the core and to the outer ring. The PE of the springs is represented by the following equation.

$$E^i_{pins} = \frac{1}{2} \sum_{ij=1}^{n} K_j \; u_j^2 \; (\theta_j, t) \tag{6.46}$$

where $i = 1, 2, 3, \cdots, n$ depending on number of ribs

Assuming four ribs for the inner winding and two approximating functions, the radial displacements of the inner springs are given by

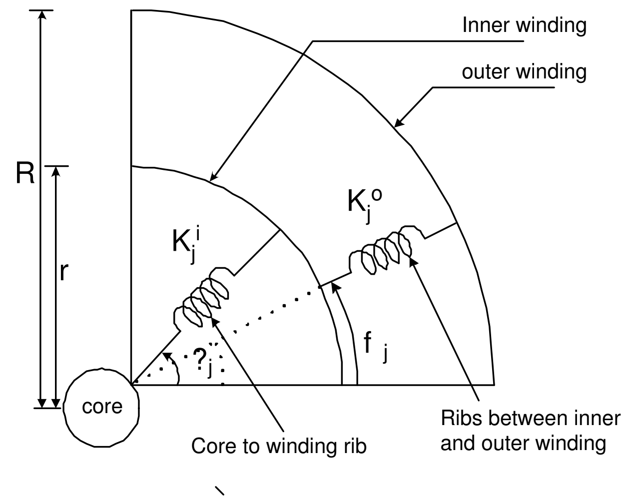

Figure 6.5: Angular position of core and ribs. The ribs are represented as coupling springs between the core and the inner winding and between the inner and outer winding

$$\mathbf{u} = \begin{bmatrix} 1 & \cos\theta_1 & \sin\theta_1 & \cos 2\theta_1 & \sin 2\theta_1 \\ 1 & \cos\theta_2 & \sin\theta_2 & \cos 2\theta_2 & \sin 2\theta_2 \\ 1 & \cos\theta_3 & \sin\theta_3 & \cos 2\theta_3 & \sin 2\theta_3 \\ 1 & \cos\theta_4 & \sin\theta_4 & \cos 2\theta_4 & \sin 2\theta_4 \end{bmatrix} \begin{bmatrix} a_0 \\ a_1 \\ b_1 \\ a_2 \\ b_2 \end{bmatrix} \tag{6.47}$$

The above matrix Equation can be written as:

$$\mathbf{u} = \mathbf{a}\;\mathbf{q} \tag{6.48}$$

Where u is the radial displacement, $\mathbf{a}$ is the matrix containing angular positions of the radial spacers and $\theta_1, \theta_2, \cdots$ are the angular positions of the ribs along the circumference of the inner winding between core and winding as shown in Fig 6.5. $\mathbf{q}$ is the vector of generalized coordinates of the radial movement.

Hence the PE stored in the ribs between the inner ring and the core is

$$E^i_{p_{is}} = \frac{1}{2} \quad \mathbf{q}^T \mathbf{a}^T \quad \mathbf{K}_i \quad \mathbf{a}\,\mathbf{q} \tag{6.49}$$

$\mathbf{K}_i$ is the non-linear stiffness of the pressboard material for the radial spacers between core and inner ring. For the radial spacers between the inner and outer ring, the potential energy depends on the relative movement of the rings and is given by

$$E^o_{p_{is}} = \frac{1}{2}\sum_{i=1}^{n} K_j \;\; (U(\phi_j,t) - u(\phi_j,t))^2 \quad = \quad \frac{1}{2}\sum_{i=1}^{n} \mathbf{K}\triangle^T\triangle$$

Where u & U are the radial displacements of the inner and outer rings respectively and Δ is the difference between U & u and $\mathbf{K}$ is the stress-strain characteristics of the pressboard radial spacers or ribs.

Assuming 6 ribs between the inner and outer rings and three approximating functions for the outer winding, the radial displacement of the inner side of outer winding radial spacer (spring) '$\mathbf{U}_i$' can be represented in the matrix form as

$$\mathbf{U}_i \quad = \quad \begin{bmatrix} 1 & \cos\varphi_1 & \sin\varphi_1 & \cos 2\varphi_1 & \sin 2\varphi_1 & \cos 3\varphi_1 & \sin 3\varphi_1 \\ 1 & \cos\varphi_2 & \sin\varphi_2 & \cos 2\varphi_2 & \sin 2\varphi_2 & \cos 3\varphi_2 & \sin 3\varphi_2 \\ 1 & \cos\varphi_3 & \sin\varphi_3 & \cos 2\varphi_3 & \sin 2\varphi_3 & \cos 3\varphi_3 & \sin 3\varphi_3 \\ 1 & \cos\varphi_4 & \sin\varphi_4 & \cos 2\varphi_4 & \sin 2\varphi_4 & \cos 3\varphi_4 & \sin 3\varphi_4 \\ 1 & \cos\varphi_5 & \sin\varphi_5 & \cos 2\varphi_5 & \sin 2\varphi_5 & \cos 3\varphi_5 & \sin 3\varphi_5 \\ 1 & \cos\varphi_6 & \sin\varphi_6 & \cos 2\varphi_6 & \sin 2\varphi_6 & \cos 3\varphi_6 & \sin 3\varphi_6 \end{bmatrix} \begin{bmatrix} a_0 \\ a_1 \\ b_1 \\ a_2 \\ b_2 \\ a_3 \\ b_3 \end{bmatrix}$$

where $\varphi_1, \varphi_2, \varphi_3, \cdots$ are the angular positions of the ribs on outer side of the inner.

The above equation can be represented as

$$\mathbf{U}_i \quad = \quad \mathbf{P}_i\mathbf{q} = [\mathbf{P}_i \quad \mathrm{O}]\mathbf{Q} \tag{6.50}$$

Where $\mathbf{Q}$ is the generalized coordinates (function of time) of radial displacement for both inner and outer rings collectively. $\mathbf{P}_i$ is the matrix representing the positions of the radial spacers (between the inner and outer winding) on the inner ring. The circumferential positions of the radial spacers on the outer ring are same as $\mathbf{P}_i$. So the outer displacements of the outer radial spacers can be represented as

$$
\mathbf{U}_o = \begin{bmatrix} 1 & \cos\varphi_1 & \sin\varphi_1 & \cos 2\varphi_1 & \sin 2\varphi_1 & \cos 3\varphi_1 & \sin 3\varphi_1 \\ 1 & \cos\varphi_2 & \sin\varphi_2 & \cos 2\varphi_2 & \sin 2\varphi_2 & \cos 3\varphi_2 & \sin 3\varphi_2 \\ 1 & \cos\varphi_3 & \sin\varphi_3 & \cos 2\varphi_3 & \sin 2\varphi_3 & \cos 3\varphi_3 & \sin 3\varphi_3 \\ 1 & \cos\varphi_4 & \sin\varphi_4 & \cos 2\varphi_4 & \sin 2\varphi_4 & \cos 3\varphi_4 & \sin 3\varphi_4 \\ 1 & \cos\varphi_5 & \sin\varphi_5 & \cos 2\varphi_5 & \sin 2\varphi_5 & \cos 3\varphi_5 & \sin 3\varphi_5 \\ 1 & \cos\varphi_6 & \sin\varphi_6 & \cos 2\varphi_6 & \sin 2\varphi_6 & \cos 3\varphi_6 & \sin 3\varphi_6 \end{bmatrix} \begin{bmatrix} A_0 \\ A_1 \\ B_1 \\ A_2 \\ B_2 \\ A_3 \\ B_3 \end{bmatrix}
$$

$$\mathbf{U}_o \quad = \quad \mathbf{P}_i\mathbf{q} = [\mathrm{O} \quad \mathbf{P}_o]\mathbf{Q} \tag{6.51}$$

$$\triangle = (\mathbf{U}_o - \mathbf{U}_i) = [\mathrm{O} \quad \mathbf{P}_o]\mathbf{Q} - [\mathbf{P}_i \quad \mathrm{O}]\mathbf{Q} = \mathbf{G}\mathbf{Q} \tag{6.52}$$

Where $\mathbf{G}$ is an arbitrary variable and

$$\mathbf{G} = [\mathrm{O} \quad \mathbf{P}_o] - [\mathbf{P}_i \quad \mathrm{O}] \tag{6.53}$$

in expanded form

$$\mathbf{G} = \begin{bmatrix} -1 & -\cos\varphi_1 & -\sin\varphi_1 & -\cos 2\varphi_1 & -\sin 2\varphi_1 & -\cos 3\varphi_1 & -\sin 3\varphi_1 & 1 & \cos\varphi_1 & \sin\varphi_1 & \cos 2\varphi_1 & \sin 2\varphi_1 & \cos 3\varphi_1 & \sin 3\varphi_1 \\ -1 & -\cos\varphi_2 & -\sin\varphi_2 & -\cos 2\varphi_2 & -\sin 2\varphi_2 & -\cos 3\varphi_2 & -\sin 3\varphi_2 & 1 & \cos\varphi_2 & \sin\varphi_2 & \cos 2\varphi_2 & \sin 2\varphi_2 & \cos 3\varphi_2 & \sin 3\varphi_2 \\ -1 & -\cos\varphi_3 & -\sin\varphi_3 & -\cos 2\varphi_3 & -\sin 2\varphi_3 & -\cos 3\varphi_3 & -\sin 3\varphi_3 & 1 & \cos\varphi_3 & \sin\varphi_3 & \cos 2\varphi_3 & \sin 2\varphi_3 & \cos 3\varphi_3 & \sin 3\varphi_3 \\ -1 & -\cos\varphi_4 & -\sin\varphi_4 & -\cos 2\varphi_4 & -\sin 2\varphi_4 & -\cos 3\varphi_4 & -\sin 3\varphi_4 & 1 & \cos\varphi_4 & \sin\varphi_4 & \cos 2\varphi_4 & \sin 2\varphi_4 & \cos 3\varphi_4 & \sin 3\varphi_4 \\ -1 & -\cos\varphi_5 & -\sin\varphi_5 & -\cos 2\varphi_5 & -\sin 2\varphi_5 & -\cos 3\varphi_5 & -\sin 3\varphi_5 & 1 & \cos\varphi_5 & \sin\varphi_5 & \cos 2\varphi_5 & \sin 2\varphi_5 & \cos 3\varphi_5 & \sin 3\varphi_5 \\ -1 & -\cos\varphi_6 & -\sin\varphi_6 & -\cos 2\varphi_6 & -\sin 2\varphi_6 & -\cos 3\varphi_6 & -\sin 3\varphi_6 & 1 & \cos\varphi_6 & \sin\varphi_6 & \cos 2\varphi_6 & \sin 2\varphi_6 & \cos 3\varphi_6 & \sin 3\varphi_6 \end{bmatrix} \tag{6.54}$$

Therefore the expression for $\triangle^T\triangle$ can be written as

$$\triangle^T\triangle = \mathbf{Q}^T\ \mathbf{G}^T\mathbf{G}\ \mathbf{Q} \tag{6.55}$$

The value of $\triangle^T\triangle$ is a matrix of size of $\mathbf{G}^T\mathbf{G}$.

The potential energy of radial spacers for the outer winding will be similar to the PE of spacers for the inner winding and given in Equation 6.42.

$$E^o_{Pins} = \frac{1}{2}\ \mathbf{Q}^T\ \mathbf{G}^T\mathbf{K}_o\mathbf{G}\ \mathbf{Q} \tag{6.56}$$

The total potential energy is the sum of elastic potential energies of the copper winding and potential energy of the insulation components and is shown as

$$E_P = \underbrace{E^i_{P_{el}} + E^o_{P_{el}}}_{E_{P_{el}}} + \underbrace{E^i_{P_{ins}} + E^o_{P_{ins}}}_{E_{P_{ins}}} \tag{6.57}$$

Hence 'E_P' can be represented as

$$E_P = \frac{1}{2}\ \mathbf{q}^T\left(\frac{\varepsilon I_i}{r^3}\mathbf{K}^{el}_i\right)\mathbf{q} + \frac{1}{2}\ \mathbf{Q}^T\left(\frac{\varepsilon I_o}{R^3}\mathbf{K}^{el}_o\right)\mathbf{Q} + \frac{1}{2}\ \mathbf{q}^T\left(\mathbf{a}^T\mathbf{K}_i\mathbf{a}\right)\mathbf{q} + \frac{1}{2}\ \mathbf{Q}^T\left(\mathbf{G}^T\mathbf{K}_o\mathbf{G}\right)\mathbf{Q} \tag{6.58}$$

The stiffness matrix of the radial behaviour can be extracted from the above equation and is shown in the following expression.

$$\mathbf{K}_r = \left(\frac{\varepsilon I_i}{r^3}\mathbf{K}^{el}_i\right) + \left(\frac{\varepsilon I_o}{R^3}\mathbf{K}^{el}_o\right) + \left(\ \mathbf{a}^T\mathbf{K}_i\ \mathbf{a}\right) + \left(\ \mathbf{G}^T\mathbf{K}_o\mathbf{G}\right) \tag{6.59}$$

The matrix $\mathbf{K}_r$ represents the stiffness of the two coupled rings in the radial direction. The stiffness of the system is dependent on the stiffness of the copper rings and the stress-strain characteristics of the pressboard radial spacers. This stiffness matrix will be further used for calculation of natural frequencies and in the dynamic SIMULINK® model in Chapter 8.

6.6 Generalized forces in radial direction

The applied electromagnetic forces in the radial direction need to be resolved according to the approximating functions used in the system of equations for the radial behaviour. These are calculated by considering the virtual work done by the electromagnetic forces.

If u and U are displacements and r and R are radii of the inner and outer winding disks respectively, the virtual work can be represented as

$$\delta w = \int_0^{2\pi} f^i(\theta,t)\ \delta u(\theta,t) r d\theta + \int_0^{2\pi} f^o(\theta,t)\ \delta u(\phi,t) R d\phi \tag{6.60}$$

by substituting the values of $\delta u\ \delta U$ with the approximating functions, the generalized forces for the inner winding can be represented as

$$\begin{aligned}
F_0^i(t) &= \int_0^{2\pi} f_r^i(\theta,t) r d\theta \\
F_1^i(t) &= \int_0^{2\pi} f_r^i(\theta,t) \cos\theta\ r d\theta \\
F_2^i(t) &= \int_0^{2\pi} f_r^i(\theta,t) \sin\theta\ r d\theta \\
&\vdots
\end{aligned}$$

and for the outer winding

$$\begin{aligned}
F_0^o(t) &= \int_0^{2\pi} f_r^o(\phi,t)\ R d\phi \\
F_1^o(t) &= \int_0^{2\pi} f_r^o(\phi,t) \cos\phi\ R d\phi \\
F_2^o(t) &= \int_0^{2\pi} f_r^o(\phi,t) \sin\phi\ R d\phi \\
&\vdots
\end{aligned}$$

Consequently

$$\mathbf{F}_r = \begin{bmatrix} f_r^i \\ 0 \\ 0 \\ 0 \\ \vdots \\ f_r^o \\ 0 \\ 0 \\ 0 \\ \vdots \end{bmatrix} \tag{6.61}$$

The equation of motion for the radial behaviour becomes,

$$\mathbf{M}_r \ddot{\mathbf{Q}} + \mathbf{C}_r \dot{\mathbf{Q}} + \mathbf{K}_r \mathbf{Q} = \mathbf{F}_r \tag{6.62}$$

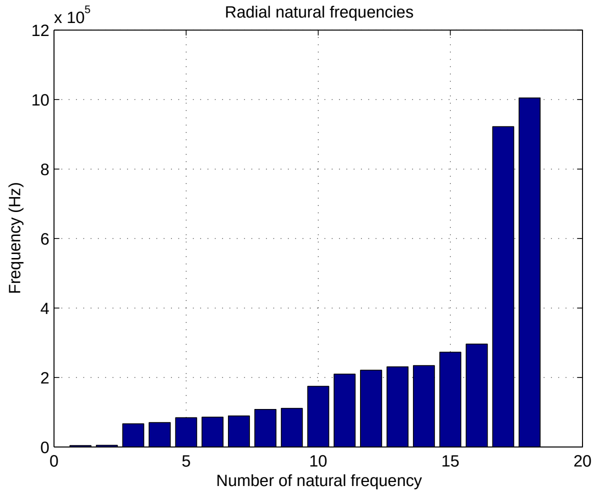

Figure 6.6: The natural frequencies of radial behaviour of test transformer

Where

$\mathbf{M}_r$	=	Mass matrix for radial behaviour
$\mathbf{C}_r$	=	Damping coefficient of insulation (pressboard ribs)
$\mathbf{K}_r$	=	Stiffness matrix including cooper and ribs (pressboard) stiffness
$\mathbf{Q}$	=	Displacement coordinates as function of time
f_r^i	=	Radial force on the inner winding ring as a function of time
f_r^o	=	Radial force on the outer winding ring as a function of time
$\mathbf{F}_r$	=	Radial force as a function of time

6.7 Modeling

A MATLAB™ code was written which is given in Appendix A. The code can predict the natural frequencies of the transformer in the radial direction and calculates the input variables for the dynamic models both in the radial and axial direction (Appendix B). The calculated natural frequencies of radial behaviour are shown in Figure 6.6.

6.8 Conclusion

The radial model is capable of calculating natural frequencies of transformer windings which gives insight of the dynamic behaviour and highlights possible resonances.

The model is intended to provide data for input to the axial, radial and combined SIMULINK® models of the transformer.

Chapter 7

Physical properties of pressboard under varying pre-stress

7.1 Introduction

Transformer board used in modern transformers has improved in density and insulation properties. It is not only used as insulation but the structural integrity of the large power transformer also depends on its mechanical properties. The board used should possess superior compressibility and stiffness properties as it is the major insulation and support structure in the inter-disk and end insulation.

Secondly, a pre-stress is applied on the transformer windings which compresses the structural pressboard to remove the sponginess which can not cope with sudden compressive forces that are applied during a short circuit or through fault condition.

The stress-strain properties of pressboard have been measured before by Patel [Patel, 1972]. However, they were measured under static load. It is believed that the properties of the pressboard under dynamic loading are different from the static characteristics [Swihart and McCormick, 1980]. During dynamic loading the material is repeatedly subjected to a compressive force. The time constant of the loading should have an effect on the stress-strain characteristics as the oil squeezed out of the material under load and will not return before the next loading cycle. The dynamic properties of the pressboard measured by Swihart and Wright [1976] and Swihart and McCormick [1980] showed a non-linear behaviour and considerable damping. However their model of the oil impregnated pressboard is complex and not user friendly. Also the full information of the model is not available due to the fact that the research was not published in the public domain.

The following procedure of measurement of stress-strain characteristics is similar to the one published by Swihart and Wright [1976] with the difference of two pressboard stacks instead of one. The advantage of this method is it is closer to the actual arrangement in practical transformer and the results obtained can be easily used in the dynamic model of a full transformer winding.

7.2 Physical properties of transformer board

To model the dynamic behaviour of a large transformer, it is mandatory to have the dynamic properties of the structural elements. In large power transformers the main structural element, which also insulates the windings from the core and ground, is the pressboard. To evaluate the dynamic stress-strain characteristics, two sections of pressboard were used in the apparatus of Fig 7.1. It is known that the properties of the transformer board are highly nonlinear. Under static loading, it shows a high strain in the beginning and as the load increases, strain decreases and the material shows higher stiffness and somewhat linear stress-strain characteristics. However, under dynamic conditions, the stiffness not only depends on the loading but also on the time duration of the loading as it will squeeze the oil in and out of the material, which influences the stiffness.

7.3 Dynamic stress-strain test apparatus

The apparatus of Fig 7.2 was used to test the dynamic properties of high density transformer board. This apparatus uses a similar technique to that used by Swihart and McCormick [1980] to measure the stress-strain characteristics. In Swihart's [Swihart and McCormick, 1980] apparatus, only one stack of the pressboard material was used and a perfectly elastic spring of known characteristics (very high stiffness) was used as a second spring. The stress-strain characteristics of the pressboard were then obtained by excluding the effects of the elastic spring in the model.

The apparatus shown in Fig 7.2 also works as a one-mass-two-spring system. It consists of a mass 'M' supported between two stacks of pressboard material (springs) connected to rigid supports at the top and the bottom. The detailed drawing of the apparatus is given in Figure 7.3. This setup is close to the reality of a large power transformers where only the pressboard is used as support material in the winding disks/turns wound with copper conductors.

The apparatus is mounted on a large damping mass and mechanically isolated from the floor by a 30 mm thick rubber cushion. A large range of pre-stresses can be applied to the material under test by the pre-stress adjuster. The value of the pre-stress can be varied from zero to a practical pre-stress value used in large power transformers. The force impulse is applied with a soft faced hammer to avoid triggering of the higher order frequencies. The dynamic force is measured with the force sensor and the displacement sensor measures the resulting displacement in the vertical direction. The apparatus is capable of measuring the stress-strain characteristics of both linear and non-linear materials.

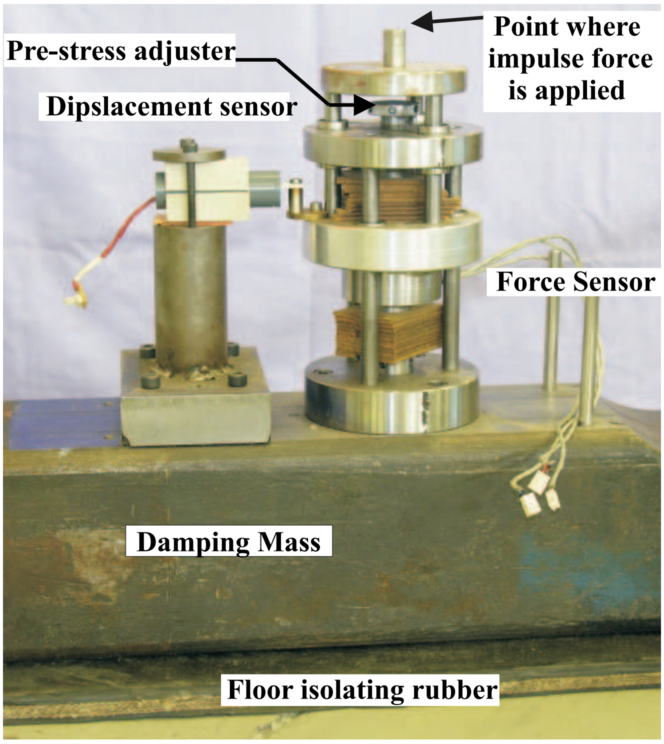

Figure 7.1: The picture of the dynamic stress-strain tester

7.3.1 Displacement and force sensors

The displacement and force sensors used in the stress-strain apparatus are shown in Figures 7.4 and 7.5.

The displacement sensor is a beam type sensor made of PVC strip of 2.5mm thickness. The other dimensions of the sensor are given in Figure 7.4. Two strain gauges (top and bottom) were used to detect the deflection of the PVC strip. The strain gauges were connected in the opposite arms of a Wheatstone Bridge. The output of

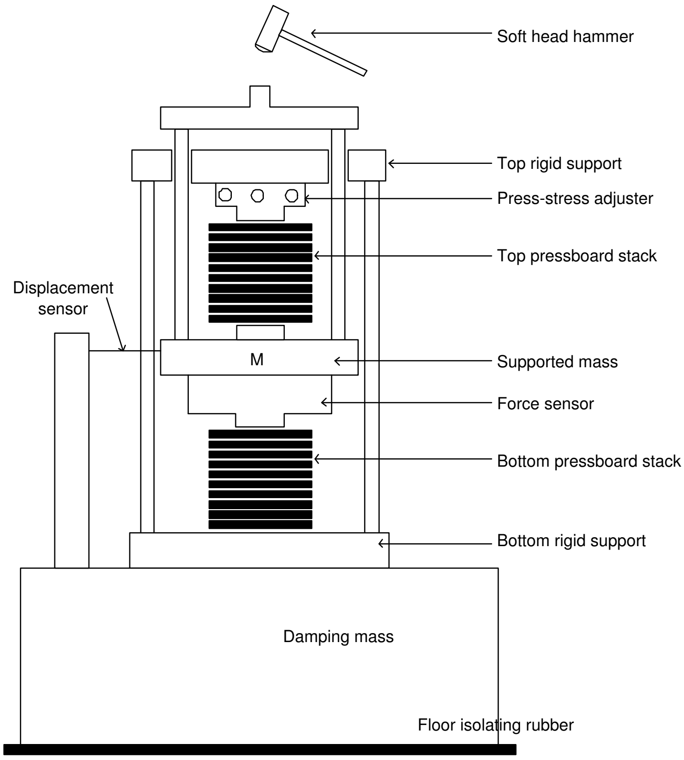

Figure 7.2: The model of the apparatus used to measure the physical properties of pressboard

the bridge was fed to an instrument amplifier which is capable of adjustable amplification of 10, 100 and 1000 times. The length of the PVC strip was kept as short as possible to avoid unwanted vibration. The active part of the sensor was housed in a PVC tube (shown in Figure 7.4) which was filled with silicone jelly to avoid high frequency vibration of the active part of the sensor. The sensor was calibrated for dynamic displacements.

The force sensor uses a simple approach of membrane deflection to measure the force. The deflection of the 3mm thick circular steel plate produces signal in each of four strain gauges (2 at top and two at bottom). The strain gauges are connected in opposite arms of the Wheatstone Bridge circuit and the resulting differential signal is fed to an instrument amplifier. The amplifier gain can be adjusted to 10, 100 or 1000 times. The force sensor was designed to be stiff so that its natural frequency is much higher than 100Hz, which is the frequency of the applied electromagnetic force in the transformer.

The reason for using strain gauge type instruments was due to the inherent properties of strain gauges to cancel magnetic field effects. The element of the strain gauge, is a conductor placed next to each other carrying opposite currents. This construction of a zigzag conductor with close spacing between its segments ensures that segments carry current in opposite directions cancelling magnetic field effects (Figure 7.4).

The use of an instrument which is not effected by the magnetic field is necessary as under short circuit conditions, the leakage magnetic field becomes stronger and can induce noise in the measured signal.

7.4 Experimental procedure

To measure the stress-strain characteristics of the high density transformer board (pressboard), 3mm thick, 50×50mm pieces of pressboard were stacked to achieve the thickness of 30mm. Figure 7.1 shows the apparatus loaded with the pressboard material.

To evaluate the properties of the material, it was dried under vacuum and impregnated with oil at 70 ^{o}C before it was fitted into the stress-strain tester. To eliminate the effects of initial thickness loss, the material was compressed three times to a load higher than the practical pre-stress values (10 N/mm^2) which will be applied during the testing. A similar prestressing process is used in industry to reduce the initial hysteresis from the material by applying a static load more than 100% of the pre-stress value. This was done to avoid the thickness loss (resulting from outward flow of oil) and to remove the permanent thickness reduction which is experienced after a drying cycle. Otherwise, the material loses its thickness during testing and the applied pre-stress reduces and sometimes disappears.

The measurement was performed at room temperature. Only one force sensor was used to record the applied force and the reaction force. The force applied to the material and displacement were recorded at different pre-stresses shown in Table 7.1 and the recorded waveforms are given in Figures 7.6 to 7.11.

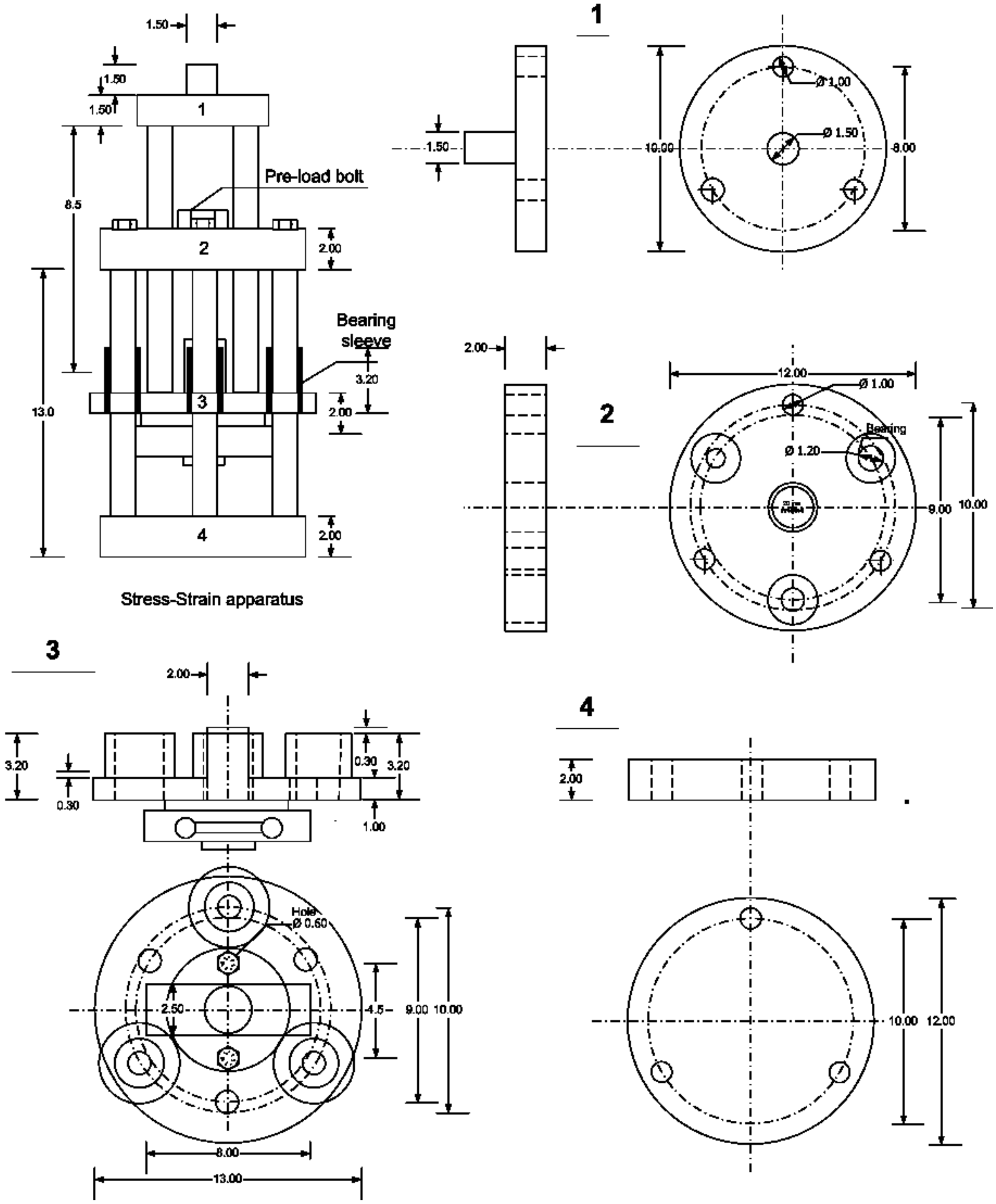

Figure 7.3: Detail drawing of Stress-strain apparatus

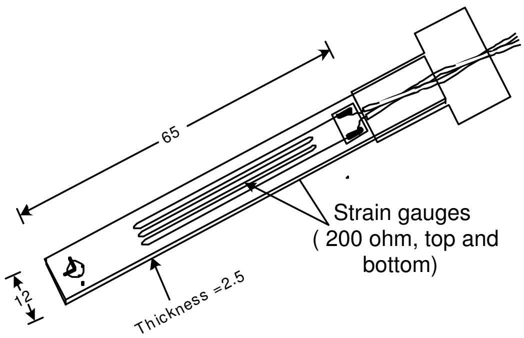

a. The detailed diagram of displacement sensor with dimensions in mm

b. photograph of the displacement sensor

Figure 7.4: Displacement sensor construction

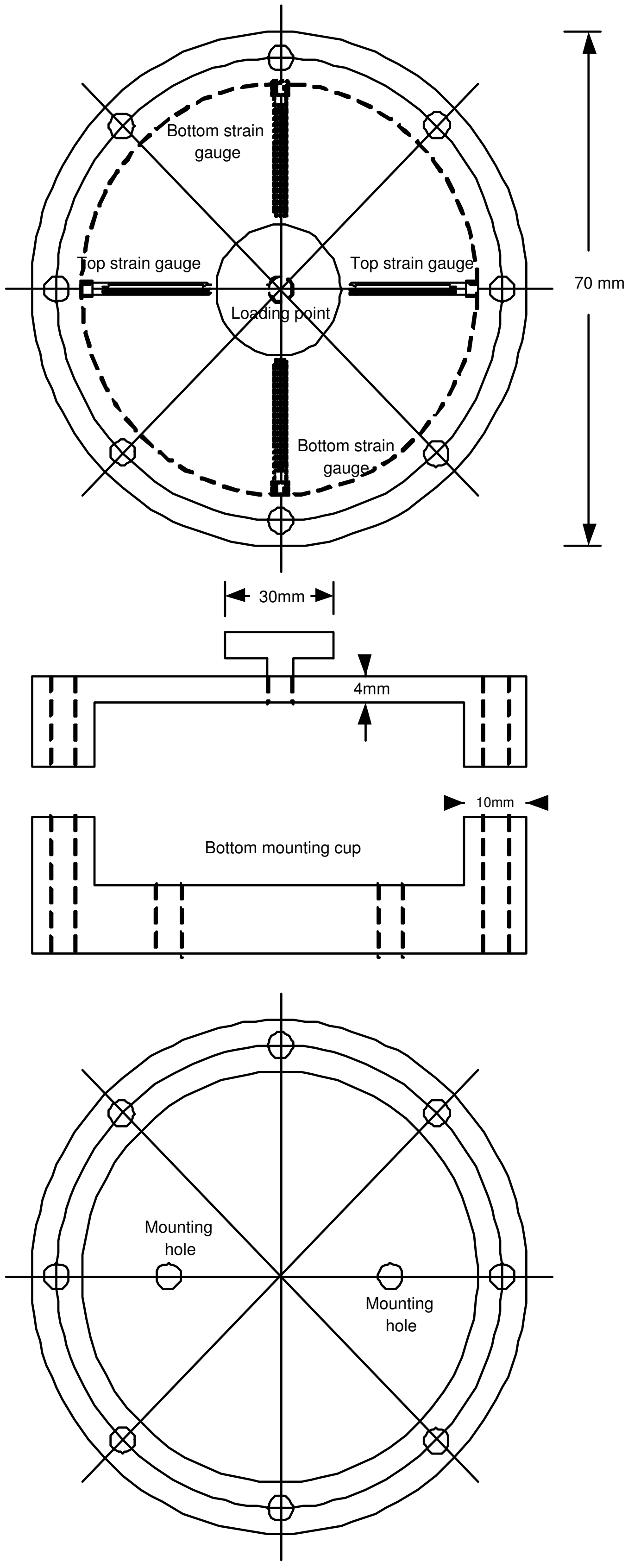

Figure 7.5: Force sensor construction detail

Diameter of contact surface (mm)	Force (kN)	Stress (kPa or N/mm^2)
30	0	0
30	1	1.42
30	3	4.3
30	5	7.1
30	7	10
30	10	14

Table 7.1: Applied pre-stress values.

The impact force waveshapes of Figures 7.6 to 7.11 were applied with a soft faced hammer. The soft faced hammer was used to avoid high frequency resonances. The resulting oscillating force and displacements were recorded with force and displacement sensors in the time domain. This measurement gave results of stress-strain characteristics of pressboard under dynamic conditions. The results of the tests at different pre-stress levels are given in Figures 7.6 to 7.11.

7.5 Results

The measured results are shown in Figures 7.6 to 7.11. The results of the stress-strain measurements confirm that the high density pressboard is not only non-linear but also possess significant hysteresis. The structure of the material and the effect of the oil impregnation has been discussed by [Patel, 1973b,a] under 'Visco-elastic' model of the pressboard.

7.5.1 Stress-Strain properties at zero pre-stress

Figure 7.6 shows the measured results of the pressboard material when no pre-stress was applied. Figure 7.6-b shows that the stiffness of the material was the highest during the first half cycle of the response and became lesser and lesser in the subsequent cycles indicated by the longer time period of the half cycles. The negative half cycles of the force are almost zero indicating separation of the pressboard stack from the mass (force sensor is a part of the mass). The negative peaks of force are very low compared to the positive peaks indicating that the expansion of the material is almost non existent. Also the negative peaks of the force half cycles are almost zero and the displacement peaks are bigger, showing that the expansion of the material happens under no force (very small interfacial tension). Actually this happens when the mass leaves the pressboard and separation of the mass and pressboard occurred. Figure 7.6-c confirmed the reduction in the stiffness in the subsequent cycles as the loop became flatter.

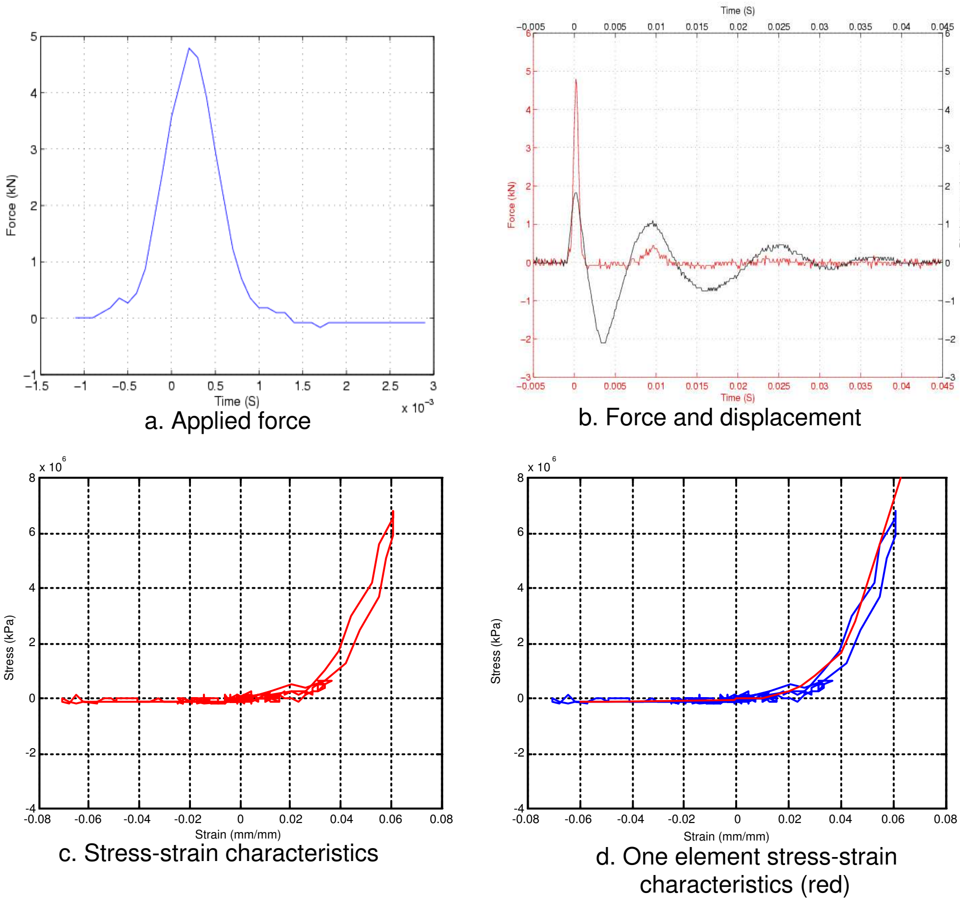

Figure 7.6: Applied force, reaction force, resulting displacement, measured stress strain characteristics and fitted stress-strain curve used in 1-mass model calibration at pre-stress value of 0 N/mm^2

7.5.2 Stress-Strain properties at low pre-stress (1.42 N/mm^2)

The results of the measurement are shown in Fig 7.7 a, b and c. In Fig b, the response of the material is different than the zero pre-stress case. The material in this case, offers relatively higher stiffness but like the previous case of Fig 7.6, the stiffness reduces in the following cycles indicated by the time period increase. Also the material is stiffer in the positive half cycles indicated by the steeper and high peaks of the force compared to the more flatter peaks in the negative half cycles.

Figure 7.7-c shows similar characteristics as Figure 7.6-c with a difference in the expansion region, where the negative force is now slightly higher. The separation is still there but it is smaller.

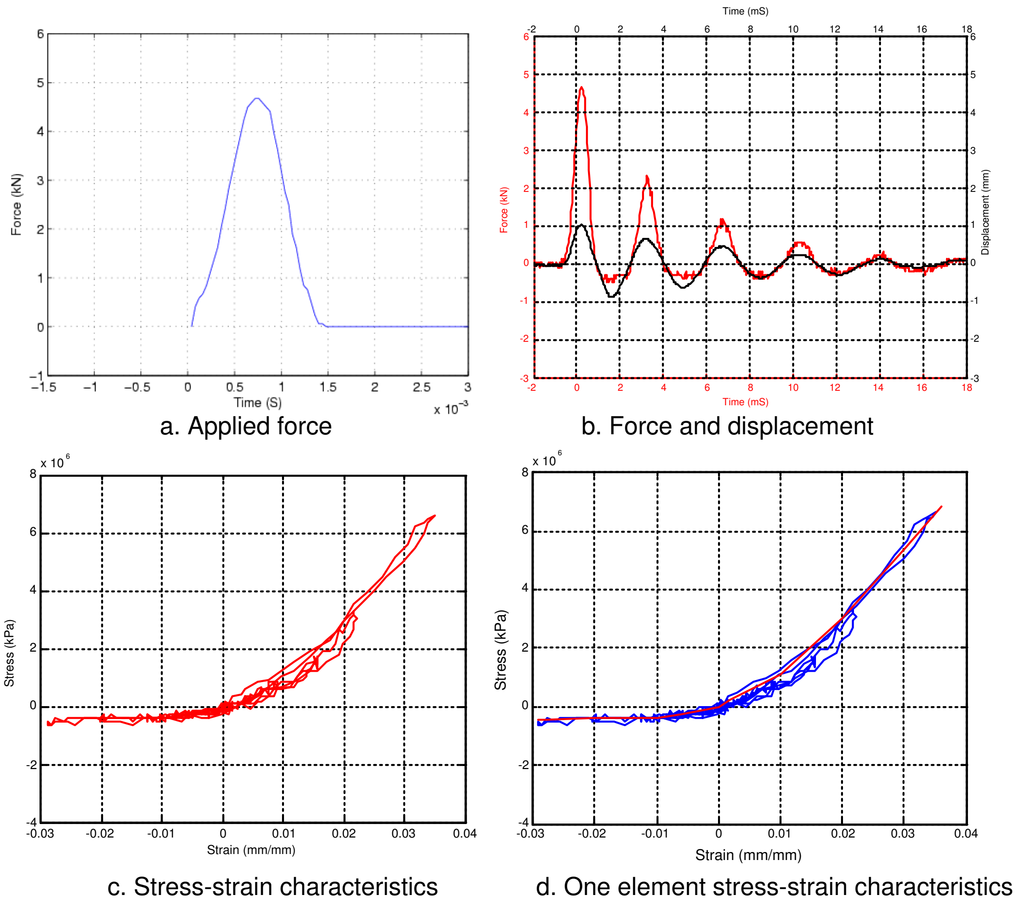

Figure 7.7: Applied force, reaction force, resulting displacement, measured stress strain characteristics and fitted stress-strain curve used in 1-mass model calibration at pre-stress value of 1.42 N/mm^2

7.5.3 Stress-Strain properties at low to medium pre-stress (4.3 N/mm^2)

Figure 7.8 shows the results of the force vs displacement and stress-strain characteristics at a pre-stress of 4.3 N/mm^2. Figure 7.8-b shows a change in the stress-strain characteristics towards relatively more linear characteristics. However, there is a slight separation below -1.2kN. Also the material offers a higher stiffness than previous cases. The material still shows similar characteristics to the previous cases, a lower stiffness in the negative half cycles compared to the positive half cycles.

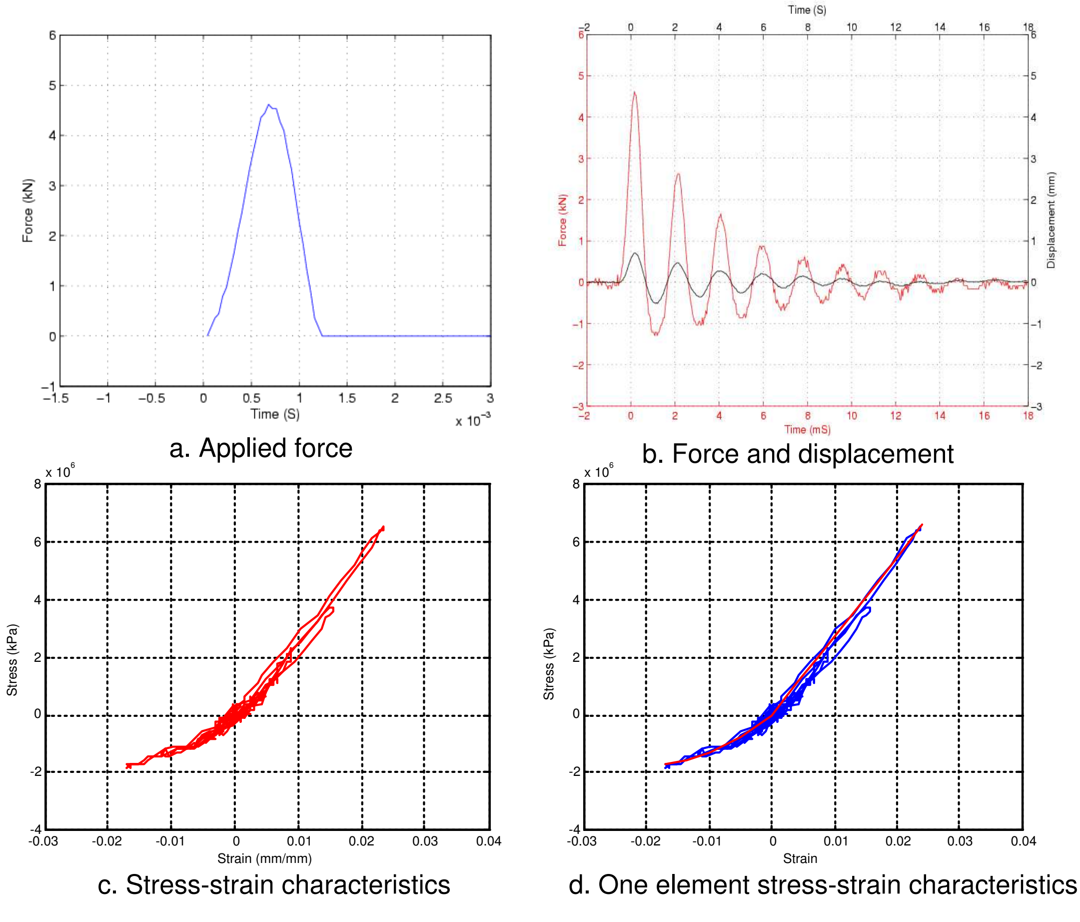

Figure 7.8: Applied force, reaction force, resulting displacement, measured stress strain characteristics and fitted stress-strain curve used in 1-mass model calibration at pre-stress of 4.3 N/mm^2

7.5.4 Stress-Strain properties at medium pre-stress (7.1N/mm^2)

Figure 7.9 shows that under the medium values of pre-stress, the material possesses a higher stiffness than the previous case. The separation is reduced and the material is very close to linear in terms of stress-strain properties. Also the higher frequency of the vibration is indicative of higher stiffness and the displacement under the same force is smaller.

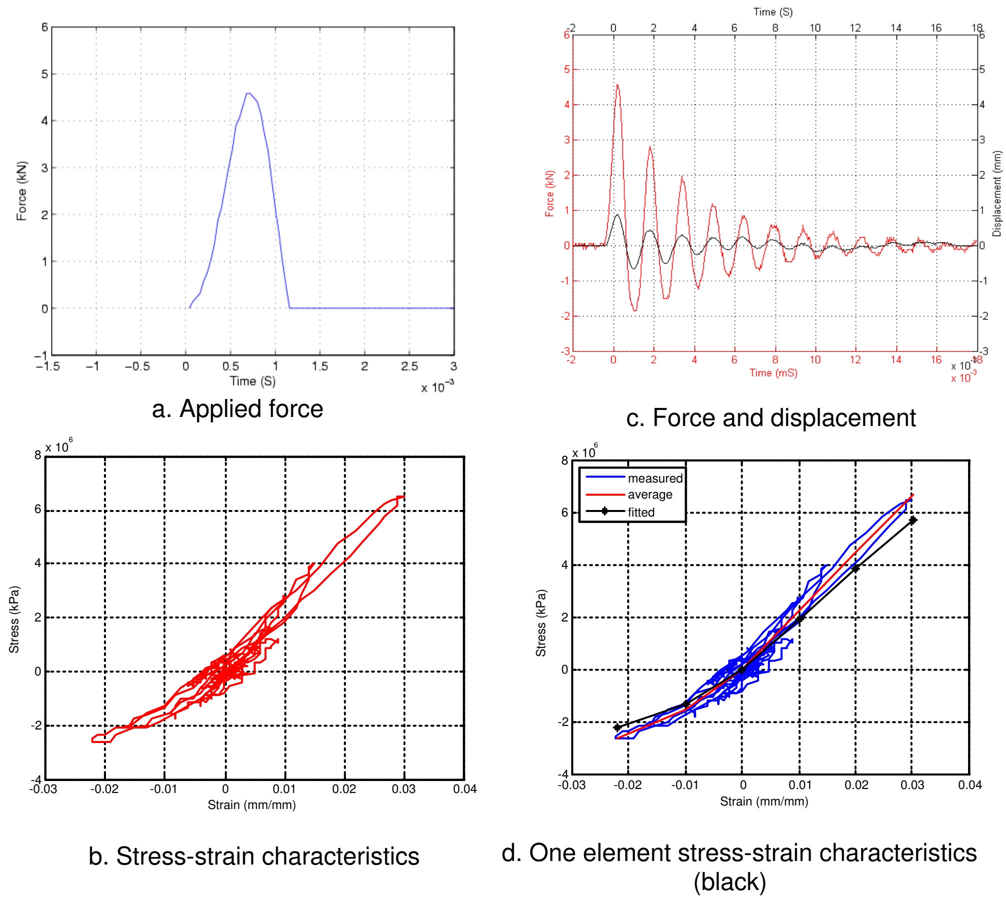

Figure 7.9: Applied force, reaction force, resulting displacement, measured stress strain characteristics and fitted stress-strain curve used in 1-mass model calibration at pre-stress of 7.1 N/mm^2

7.5.5 Stress-Strain properties at medium-high pre-stress (10 N/mm^2)

Figure 7.10 shows the material under this pre-stress of $10N/mm^2$ behaves almost like a linear spring with hysteresis. The peak values of displacement in positive and negative half cycles are still not similar but the difference is not as large as in the previous cases. The stiffness still decreases with time.

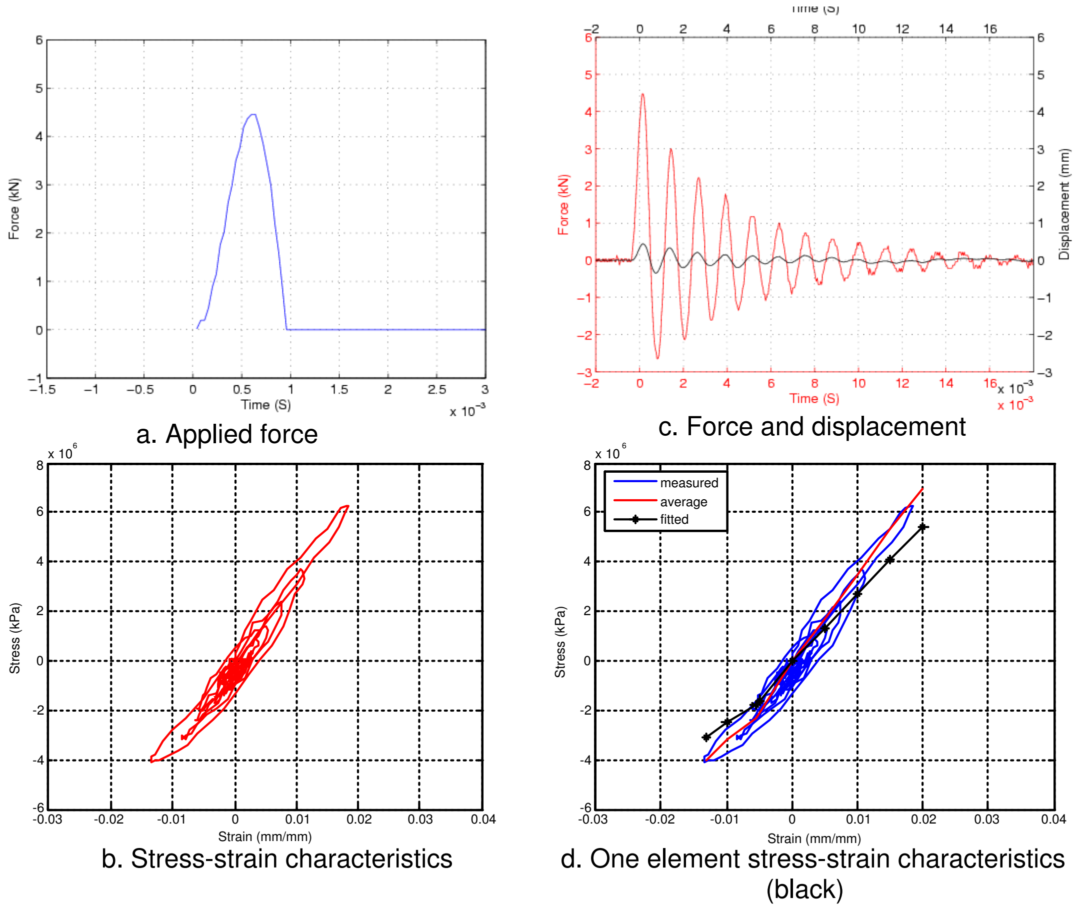

Figure 7.10: Applied force, reaction force, resulting displacement, measured stress strain characteristics and fitted stress-strain curve used in 1-mass model calibration at pre-stress of 10 N/mm^2

7.5.6 Stress-Strain properties at high pre-stress (14 N/mm^2)

Figure 7.11 represents the behaviour of the material at the maximum pre-stress applied to the samples. The resulting stress-strain characteristics are close to the desirable values. There is no separation and the average stress-strain curve of the material is almost linear (if hysteresis is omitted). The material offers the highest stiffness both in the positive and negative half cycles.

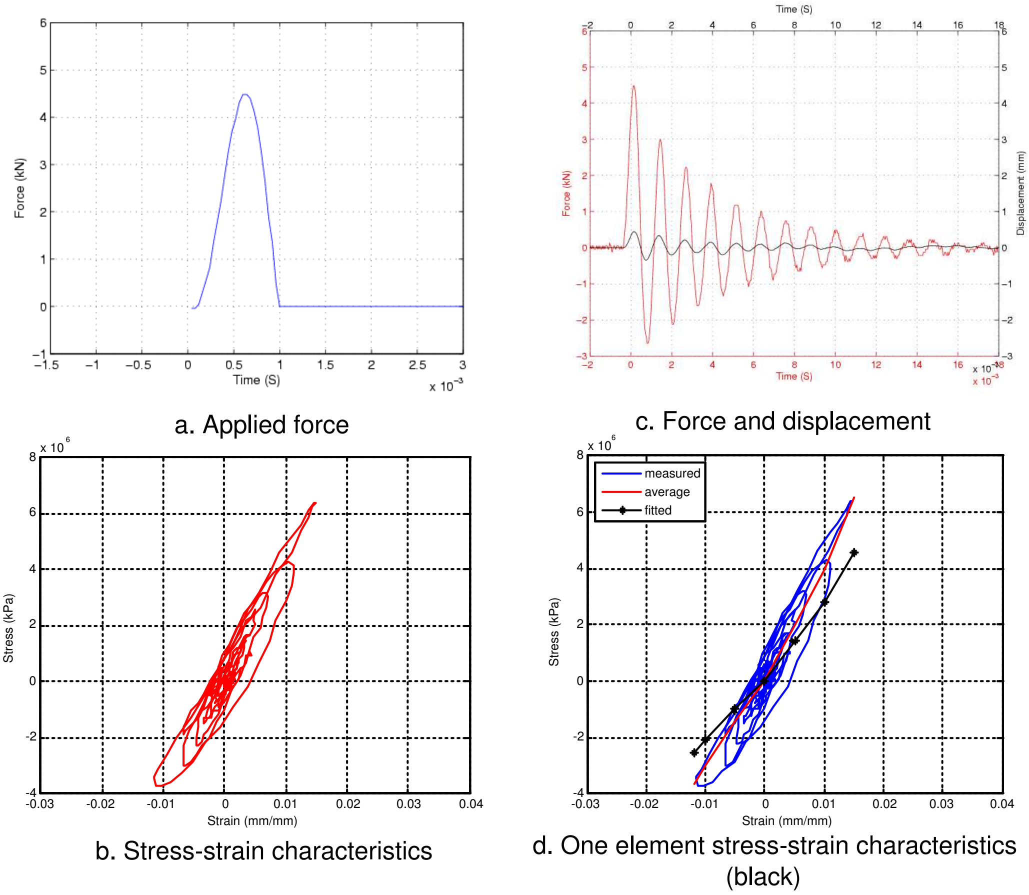

a. Applied force

b. Stress-strain characteristics

c. Force and displacement

d. One element stress-strain characteristics (black)

Figure 7.11: Applied force, reaction force, resulting displacement and measured stress strain characteristics at pre-stress value of 14 N/mm^2

7.6 Modeling of experimental set up as spring-mass system

The dynamic stress-strain measurement can be modeled by the spring mass model of Figure 7.12-b with two linear springs supporting a mass and being attached to a rigid structure. In reality, the pressboard material represented as springs is non-linear. It has non-linear stress-strain characteristics and a complex damping behaviour. The objective of this modeling is to separate the stress-strain properties and the damping coefficient from the measured data of the previous section which will be used in further models of full transformer.

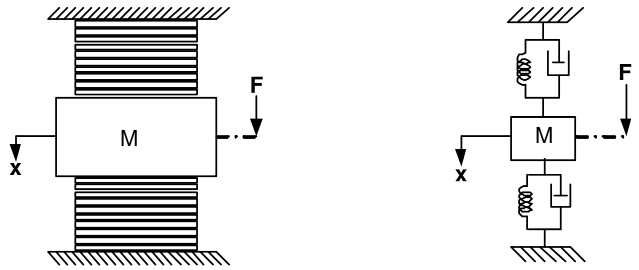

a. Simplified apparatus representation   b. Equivalent spring-mass system

Figure 7.12: Experimental setup represented as spring-mass system

7.6.1 Mathematical model

The results of the measurements presented in Section 7.5 are the stress-strain properties of the whole system consisted of two stacks of pressboard (non-linear springs with damping) and a mass between them. The simplified equivalent diagram of the system is given in Figure 7.12-b. The equation of motion for the spring mass system can be written as:

$$M\ \ddot{x} + C\ \dot{x} + g(x)\ x = F(t) \tag{7.1}$$

Where:
M = mass,
C = damping coefficient
$g(x)$ = stress-strain characteristics of pressboard
$F(t)$= force as a function of time
In Equation 7.1, $g(x)$ represents the stress-strain characteristics of the non linear pressboard and was determined by a lookup table.

The stress-strain characteristics of the pressboard at different pre-stresses measured in Section 7.5 are available in the form of loops due to the hysteresis of the material which makes the model very complex.

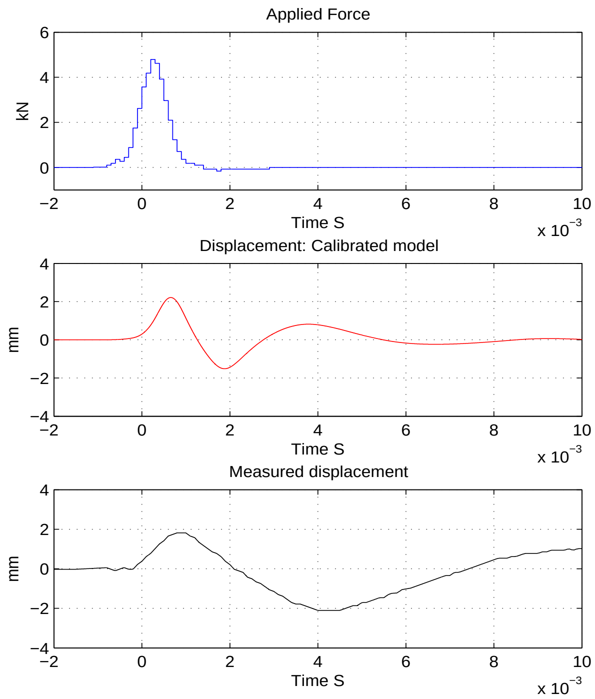

Figure 7.13: Comparison of measured and calibrated results from the model at pre-stress of 0 N/mm^2

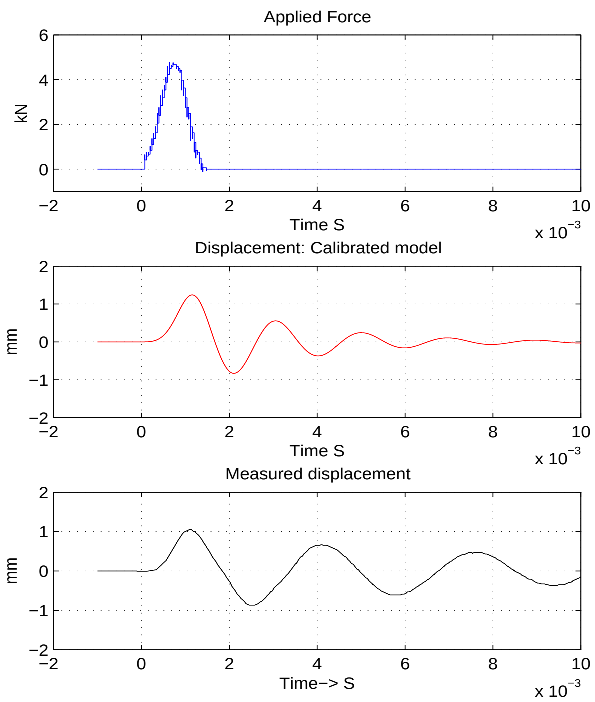

Figure 7.14: Comparison of measured and calibrated results from the model at pre-stress of 1.42 N/mm^2

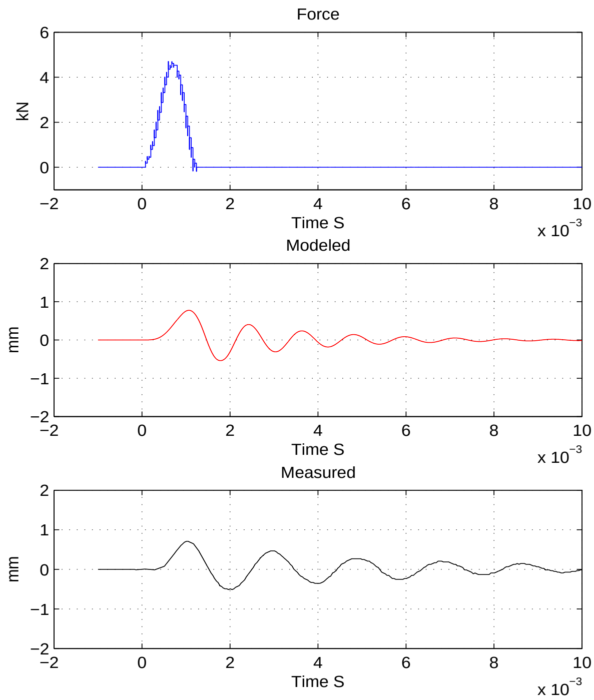

Figure 7.15: Comparison of measured and calibrated results from the model at pre-stress of 4.3 N/mm^2

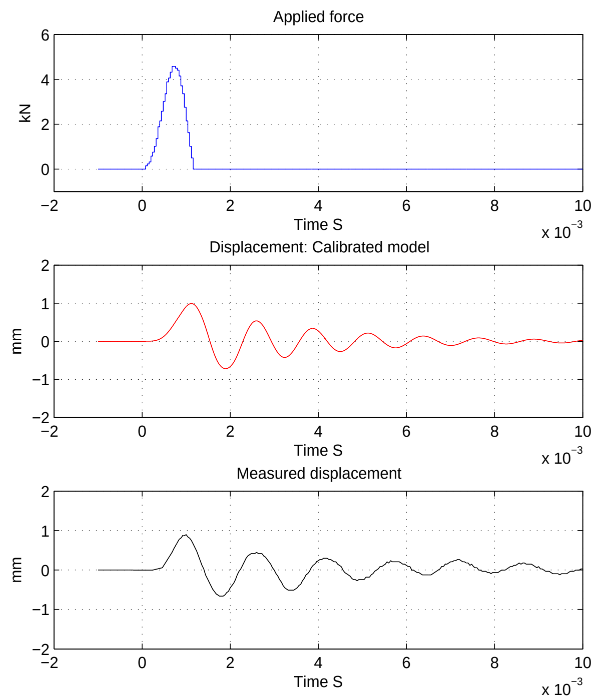

Figure 7.16: Comparison of measured and calibrated results from the model at pre-stress of 7.1 N/mm^2

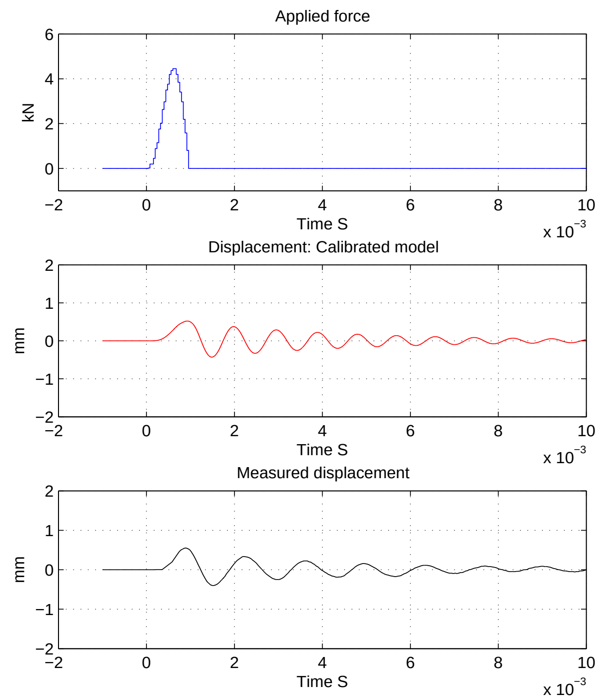

Figure 7.17: Comparison of measured and calibrated results from the model at pre-stress of 10 N/mm^2

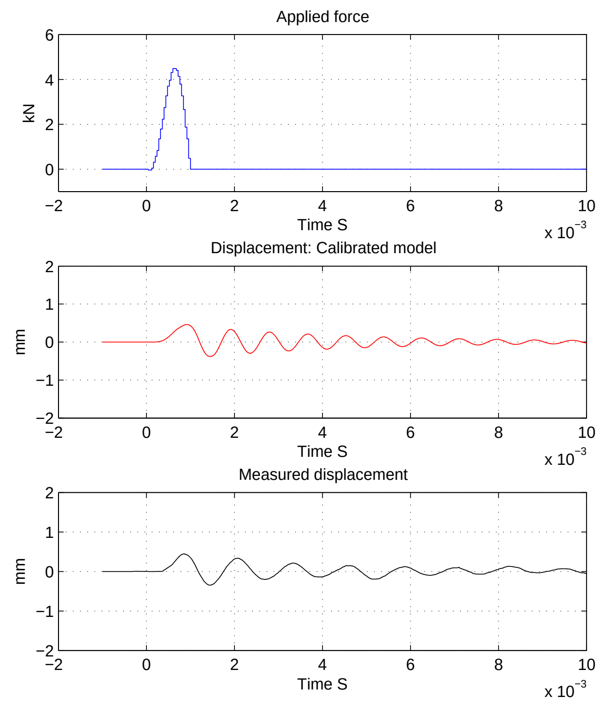

Figure 7.18: Comparison of measured and calibrated results from the model at press-stress of 14 N/mm^2

It is been established in the literature and here in the results of the measurements that the properties of the pressboard not only vary under different stress but have a significant hysteresis [Swihart and McCormick, 1980]. In this work, to simplify the problem, the hysteresis was neglected and an average curve (as shown in the sub-figures d of Figures 7.6 to 7.11) passing through the hysteresis loop was used for further calculations. This was not a big limitation as the difference in response only becomes significant later on in time. In reality, the first few peaks of the displacement are off interest (under transient conditions). After the first few peaks, the current transient and resulting forces become smaller and are not as destructive. Also, it is believed that the peak of the first half cycle is the highest peak and is the main cause of winding failures in power transformers [IEC 60076, 1992].

The nonlinear springs of Figure 7.12 are directional springs and have different characteristics under compression and expansion. In the model, the two springs are connected to the mass and can be considered as back to back. When the impulse load is applied to the mass, the bottom spring gets compressed while the top spring expands. Similarly when the bottom spring relaxes the top spring goes into axial contraction. A schematic representation of the collective response of both of the springs is of a push-pull type. The simplified stress-strain characteristics of the system of springs are given in Figure 7.19. The stress-strain characteristics measured in Section 7.5 is the combined effect of the two springs. Therefore the properties of a single spring are required for simulation. Due to the nonlinear behaviour of the material there is no easy way to extract the stress-strain properties of a single spring from the measured data. Also the properties of the material change with different pre-stress, which makes the problem more complicated and no single technique was sufficient to extract the properties of a single spring. Hence the model approach was adopted. The model was calibrated to the measured response to determine the stress-strain characteristics and damping coefficient for a single spring. It is an adaptive model.

During the model adaptation process, curves were fitted and the properties of one spring were extracted. Figures d in Figures 7.6 to 7.11 show the stress-strain characteristics required to produce a curve similar to the measured one.

As a result of simplifications made in the model, there is a large discrepancy in frequency between predicted and measured frequency of oscillation particularly, when pre-stress is absent or very low. However, the objective of this work is to predict the maximum displacement which is the first peak and subsequent peaks are of secondary importance. For all values of pre-stress, the co-relation between measured and predicted maximum displacement is good.

In the cases of pre-stress of 0, 1.42 and 4.3 N/mm^2, only one side of the pressboard stacks shows stiffness. The expanding spring has negligible or no contribution to the oscillatory motion. Hence the stress-strain curve (of a single pressboard component 'spring') for these pre-stresses is the average curve without the hysteresis. As the pre-stress increases, the expansion of the so-called springs becomes a reaction force. In the case of pre-stress of 7.1 N/mm^2, the force contribution of the expanding pressboard part becomes about 15% of the measured curve, the lower curve of Figure 7.9. An expansion effect of 30 % of the measured stress-strain characteristics came from the expanding pressboard component at a pre-stress of 10 kN and 14 kN/mm^2. At these pre-stress values, the average curve of the measured stress-strain values is more linear.

In the measurement of the stress-strain characteristics in Section 7.5, the damping and the stiffness of the displacement sensor was neglected. It was noticed that when the displacement was large there was some extra stiffness in the system which could possibly be due to the displacement sensor. The flexible arm length of the displacement sensor was only 65mm which under larger displacements may create stiffness issues. Hence care was taken to ensure the sensor arm remained in a horizontal position before the load is applied. This means that the stress-strain characteristics may not have been measured with a high accuracy. However, the same sensors were used for the transformer experiment and the errors are likely to be consistent in both sets of measurements.

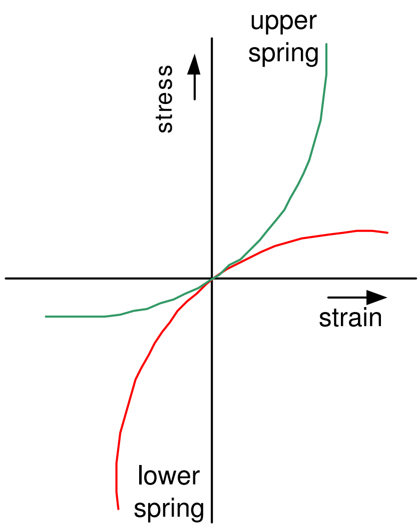

Figure 7.19: Schematic representation of the stress-strain properties of two nonlinear springs in a back to back arrangement

Pre-stress N/mm^2	Damping coefficient $N.s/m$
1.42	170
4.3	170
7.1	125
10	90
14	90

Table 7.2: Damping coefficient at different pre-stress values

7.6.2 Damping

The results of the experimental work (Figures b of Figures 7.6 to 7.11) are shown as force and displacement curves. The results for displacement vs time indicate that the material has a significant damping. The damping is maximum in the first cycle and decreases gradually thereafter as illustrated in Table 7.2. This behaviour of the material can be attributed to the oil squeeze-out of the pressboard under the initial force impact. The inward flow of the oil has to happen under normal atmospheric pressure. This is either very little or almost non-existent in the short space of time before the second cycle of the transient starts, which again removes the major portion of the remaining oil. The evaluation of this non-linear damping, coupled with the hysteretic damping (as the material has hysteresis) is difficult and no simple method can be used for the prediction of damping. The damping coefficient was needed to fit the behaviour under different pre-stress values. Therefore, the model calibration approach for the prediction of the damping coefficient was used. The damping coefficient is larger at low pre-stress compared to the higher pre-stress value. It must be noted that the viscus damping of the oil, in which the windings move, is neglected in this work.

The mathematical model of the spring-mass system was implemented in SIMULINK® as shown in Figure 7.20. The results obtained after the calibration of the model are presented in Figures 7.13 to 7.18. The stress-strain curves to be used in the further simulations are given in part-d of Figures 7.6 to 7.11. The stress-strain characteristics (fitted waveform part-d Figures 7.6 to 7.11) and damping coefficient values obtained from the calibrated model will be used in the modeling of an actual transformer.

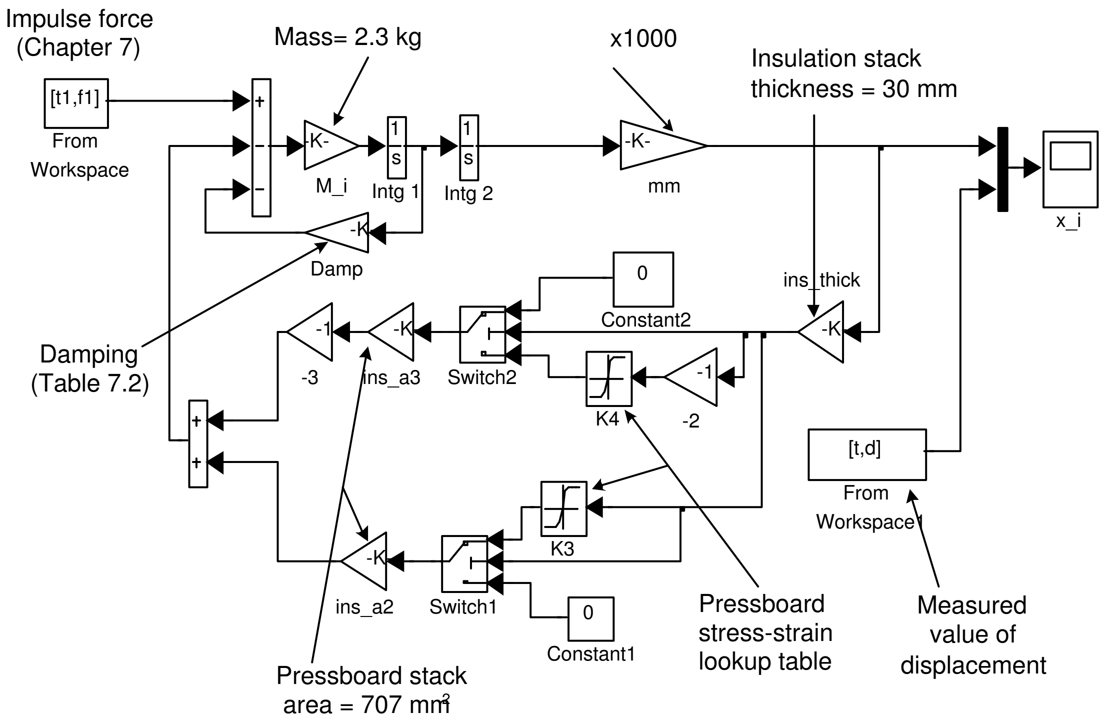

Figure 7.20: Simulink model of mass-spring system

7.7 Discussion

The experimental measurements shown in Section 7.5 indicate that high density pressboard possesses non-linear properties with hysteresis and complex damping. However, the linear approximation of damping is appropriate for initial cycles.

It is noted that the material shows an initial higher stiffness under dynamic loading which can be attributed to the squeezing out of oil as mentioned by Patel [1972]. Subsequently, the material shows lower stiffness and consequently a lower frequency of vibration with time.

The properties appear in their most complex form in the first case where there is no pre-stress. The time period of the first half cycle is much smaller than the later ones. This is due to a considerable change in stiffness which is attributed to the outward oil flow from the pressboard material. Once the oil is out, the material has a very low stiffness and low frequency of vibration compared to the oil saturated situation in the first half cycle.

As the pre-stress increases the non-linearity of the material decreases (Figures 7.6 to 7.11). This is evident from Fig c of Figure 7.6 where there is no negative force and the highest negative force is observed in Fig 7.11.

The reaction effect of the expanding pressboard section increases with the pre-stress. This is evident from the measured stress-strain characteristics because the pressboard non-linearity reduces with the increase of pre-stress. This is the reason for the declining slope of the average stress-strain curve representing each cycle of vibration as seen in the Figure-c of Figures 7.6-7.11.

Due to the inaccuracies and limitations of the sensors, the curve fitting was not very accurate in cases of larger displacements. This could be prevented in future work by choosing non-contact type sensors for displacement.

To simplify the model, damping has been considered as constant for each value of pre-stress rather than using a function dependant on stress, time and degree of oil impregnation. The simplification has still permitted a reasonable prediction of the first and highest displacement peak.

7.8 Conclusions

1. The pressboard material is highly non-linear under low pre-stress. As the pre-stress increases the material becomes more and more linear. This is due to the changed degree of oil impregnation of the pressboard.

2. The oil contained in oil impregnated pressboard is removed by impulse or loading and the material becomes softer. However, the oil can move back into the pressboard and restore the stiffness if sufficient time is allowed.

3. It was not easy to have a simple equation for predicting stress-strain characteristics of one spring. Hence the technique of model calibration is suggested.

4. The oil impregnated pressboard possesses a complex damping. The damping coefficient was predicted by the model calibration.

5. The damping properties of the oil impregnated pressboard decrease with increase of pre-stress.

6. The reaction effect of the expanding pressboard (non-linear spring) increases with the increase in the pre-stress.

7. Non-contact type sensors should be used for more accurate measurements.

8. This work shows that a sufficient amount of pre-stress is necessary in a transformer if a 'near linear' mechanical behaviour of pressboard is desired.

Chapter 8

Combined transformer model

8.1 Introduction

In the past, researchers have investigated the axial and radial models separately. In a real transformer, these behaviours are coupled and believed to have an effect on each other. The electromagnetic forces in a transformer have radial and axial components due to the positions of the turns in the winding. During a short circuit, the winding movements result in a change in relative position of the turns. This results in change in the forces. In this work, the movement of the windings are assumed very small. Hence the forces will remain same throughout the dynamic phenomenon.

The dynamic radial forces can vary due to the axial movement and vice versa. The movement of the windings in axial direction winding may be limited due to the friction offered by the structure of the windings and core.

The implementation of a combined transformer model is discussed in this chapter. The radial and axial models developed in previous Chapters 5 and 6 are combined to assess the behaviour of the transformer winding when subjected to pulsatory forces produced by the short circuit currents. The method of combining of the models is also presented in this chapter. The combined model was implemented in SIMULINK®. The detail of the implementation of the model is given in appendix B. This work is limited to helical and disk type windings where the pressboard axial spacers are used as inter-disk insulation. The helical and disk type windings are the most common windings in large power transformers.

8.2 Components of the model

The active part of a power transformer consists of a number of components like core, yoke, clamping structure, axial and radial insulation, copper conductors and the winding end insulation. The core and yokes consist of steel laminations stacked together. The core and yoke are made of magnetic material to cage the main flux. The clamping structure of the windings consists of core clamps and tie bars. They are made of either magnetic or non-magnetic steel of high tensile strength. During short circuits, deformation in the clamping structure is rare. The weakest part in the winding is the axial and radial insulation (pressboard), which provides most of the flexibility and damping under the influence of the compressive forces during the fault conditions especially for helical and disk type windings. The mechanical representation of the insulation and winding conductors is discussed in the following sections.

8.2.1 Axial spacers (pressboard)

The axial spacer is used in the winding to maintain the winding structure and for inter-disk insulation. In this work, the axial, radial and end insulation is represented as a non-liner directional spring connected to a dashpot in parallel as shown in Fig 8.1 (a). The oil impregnated pressboard insulation has non-linear characteristics under dynamic load conditions which has been discussed in detail in Chapter 7.

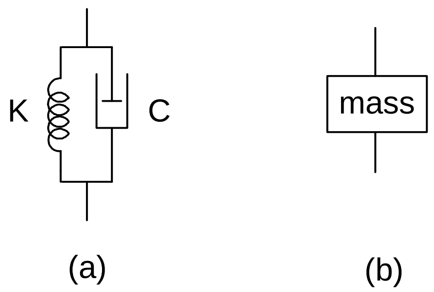

Figure 8.1: Components of mechanical model of a transformer

8.2.2 Lumped masses, springs and dashpots

The mass of the whole winding can be lumped into several smaller portions to reduce the degrees of freedom of the system. The lumped parameters should be close to the actual structure so that the dynamic behaviour predicted by the lumped mass model is sufficiently close to the actual behaviour. The idea is to reduce the computational time and to make the model more manageable. The similar techniques have been adopted in literature [Tournier et al., 1964, 1962a,b; Patel, 1972, 1973b]. The authors in their models lumped few disks of the disk type winding as one mass to make the problem simpler for the computational process. However, in this study each disk is represented as a separate mass which is more realistic and comparable with the actual large power transformer where each disk of the winding is connected to the next disk with the axial spacer (pressboard). Similar technique is followed for the lumped non-linear springs and one set of axial spacers (pressboard) between two disks is treated as one spring. The same rule applies to the damping effect of the vertical spacer.

8.3 Combined model of a transformer winding

To establish a combined model of a winding, the following components/steps are required:

- electromagnetic forces calculation to predict
  - axial forces
  - radial electromagnetic forces
- dynamic models
  - dynamic axial model
  - dynamic radial model
- combined model

The prediction of the electromagnetic forces, the factors influencing them and methods of calculation are discussed in Chapters 3 and 4. A MATLAB™ code was written to calculate these forces is given in Appendix A. The code generates a time varying waveform which was further used as the input to determine the response of the dynamic model. The dynamic model was implemented and simulated in SIMULINK®.

8.4 Axial and radial models

The arrangement of components and the mathematical representation of radial and axial models is given in Chapters 5 and 6 respectively. The models are built with the components discussed in the Section 8.2.2.

8.5 Coupled dynamic model

The suggested coupled dynamic model of a transformer is discussed here along with coupling technique. Figure 8.2 shows the components of the coupled two-winding transformer model including the friction with core which may retard the axial motion.

In a perfectly designed and manufactured transformer, the windings are always under compressive forces even during short-circuits. During the dynamic phenomenon (under short circuits) the axial forces will become different from the applied pre-stress and may not remain the same for the whole winding especially when the windings are of different heights or in the event of geometric mismatch of their centers. This could result in magnetic unbalance resulting in unbalanced forces in the upward or downward directions. The forces which are working against the pre-stress will produce a very high or no pressure in the magnetically unbalanced regions of the winding. The areas where the pressure is higher than the pre-stress the radial movement will be impeded due to the increased friction on the surface of the vertical spacer surfaces as shown in Figure 8.4. However, the forces on the unsupported length of the conductors will remain same as the electromagnetic force. On the other hand, the movement of the inner winding towards the core limb (inward), will produce enhanced friction and resistance to the axial movement (Fig 8.5). This phenomenon is only applicable to the inner winding provided there is no permanent deformation during the short circuit. The flow chart of Figure 8.3 shows the coupling technique used to couple the axial and radial models in SIMULINK®. The friction between the core and the inner winding can be regarded as Coulomb damping. Patel [1972] has suggested a method to determine the coefficient of friction experimentally. In this work the friction coefficient determined by Patel was used.

8.6 Test transformer

For model response validation, a single phase, two-winding test transformer was built and is shown in Figure C.1. The diagram of the core section and winding detail is given in Figure 8.6 and 8.7. The detail of the design of the test transformer is given in Appendix C. The transformer has a 1:1 ratio. Both inner and outer windings were of the disk type having 6 disks each with 5 turns in each disk. The inter-disk insulation (clacks or vertical spacer thickness) is 10 mm. A larger thickness of 10 mm was used to reduce the stiffness in the axial direction and was not due to the voltage between the disks which are not more than 20V under normal operating conditions. The other advantage of identical windings was to ensure zero initial displacement

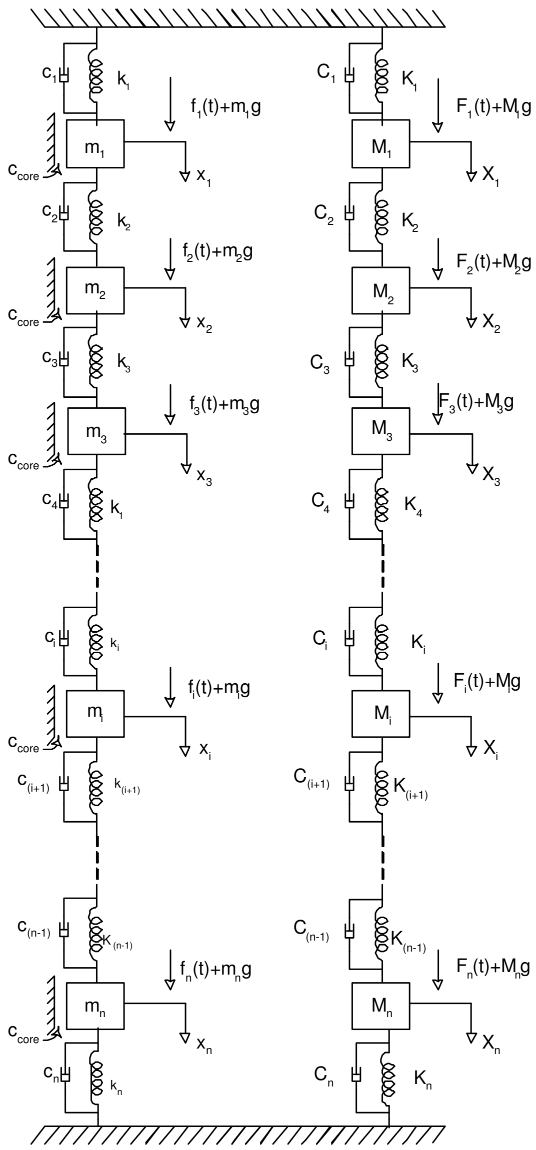

Figure 8.2: Proposed two-winding dynamic axial model

which could have produced unexpected forces. The disadvantage of the disk type windings is its stiffness (in radial direction) which is very high and results in a very small radial displacement.

The inner winding of the transformer was permanently short circuited and the current was injected in the outer winding.

8.7 Test setup and procedure

The circuit diagram of the test setup is given in Figure 8.10. A three phase alternator was used to supply the single phase current. The alternator was rated 450kVA and was driven by a forced air cooled motor. The terminal of the voltage of the alternator

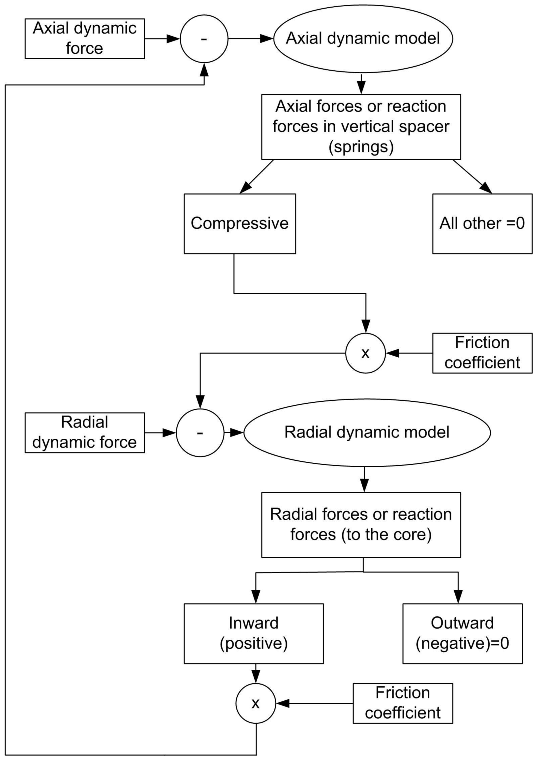

Figure 8.3: Dynamic axial and radial models combining technique

could be controlled manually and was used to control the current. A maximum short circuit current of 4kA could be drawn from the alternator at a voltage of 130V.

An electronically controlled dc powered switch was used to energize the short-circuited transformer. The current switching mechanism was able to operate around 100 μ s of zero crossing of the voltage waveform. It was necessary to close the switch at the zero crossing for a steady increase of first half cycle of the current giving the maximum displacement in the transformer windings. The current was injected into the transformer using a break-before-make mechanism where the supply of the motor driving the alternator was 'Switched Off' before applying the short circuit on the terminals of the alternator. The maximum peak current injected was under 4kA. Current higher than 4kA was not possible due to the susceptibility of malfunctioning of the electronic switch as the higher terminal voltage was required for higher current but the zero crossing switch was not capable of handling the electromagnetic noise generated at higher voltages.

The test transformer was equipped with two displacement sensors (Chapter 7). The first was used to measure the axial movement at the lower most disk of the outer winding. The second displacement sensor was used to pick up the radial displacement of the same disk.

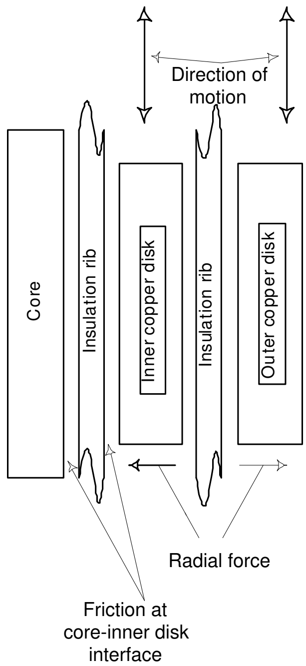

Figure 8.4: The effects of friction on axial motion

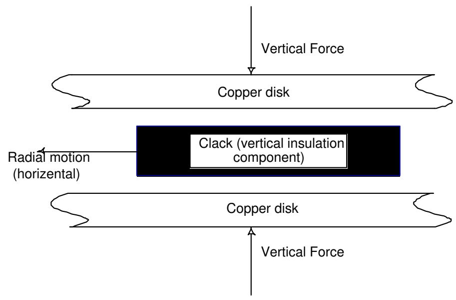

Figure 8.5: The effects of friction on radial motion

8.8 Simulated and measured results

Figures 8.11 and 8.13 show the simulated and measured results of axial displacement of the bottom disk of the test transformer at a medium pre-stress of 7.1 N/mm^2 and a high pre-stress of 14 N/mm^2. The results qualitatively co-relate with the simulated results. However, quantitatively the measured displacement is 20%-30% larger than the simulated values.

Figures 8.12 and 8.14 show the measured and simulated displacements in radial direction. The measured displacements are significantly larger than the simulated radial displacements. The larger displacement is due to the difficulty in separating the in-phase larger axial displacement from the very small radial displacement.

Another important observation was, that the interaction between the radial and axial

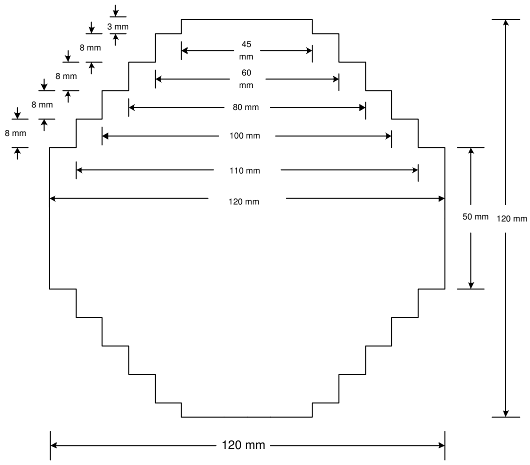

Figure 8.6: The cross-section of the core of the test transformer

forces was negligible. During the period of forced vibration, there is no significant difference between the axial displacements of the combined and stand-alone models as illustrated in Figure 8.9. However, during free vibration, the combined model shows a higher damping and a rapid decay of vibration which is also clearly obvious from Figure 8.9. This is due to the axial friction which is modeled in the combined model but neglected in the stand-alone axial model.

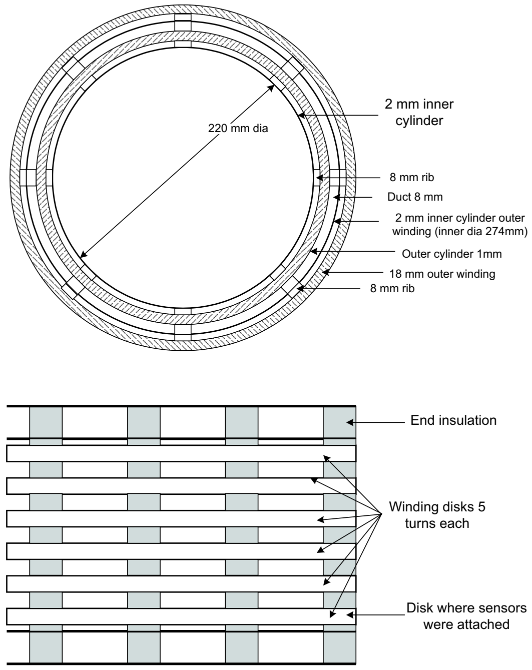

Figure 8.7: The detail of the winding configuration of the test transformer

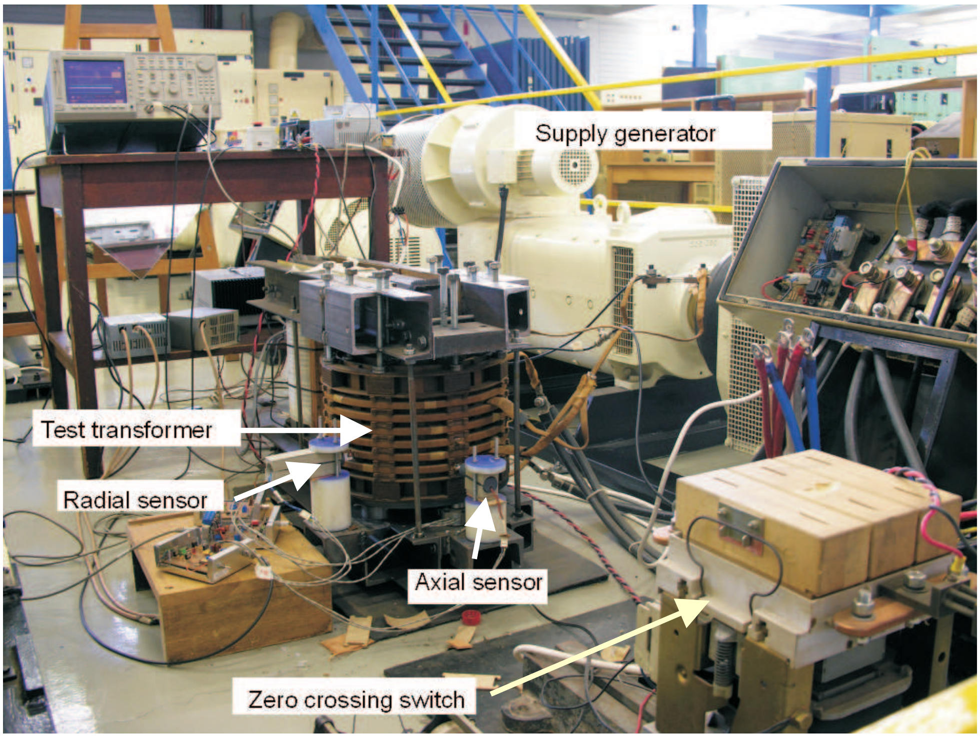

Figure 8.8: Single phase two-winding test transformer in experimental setup

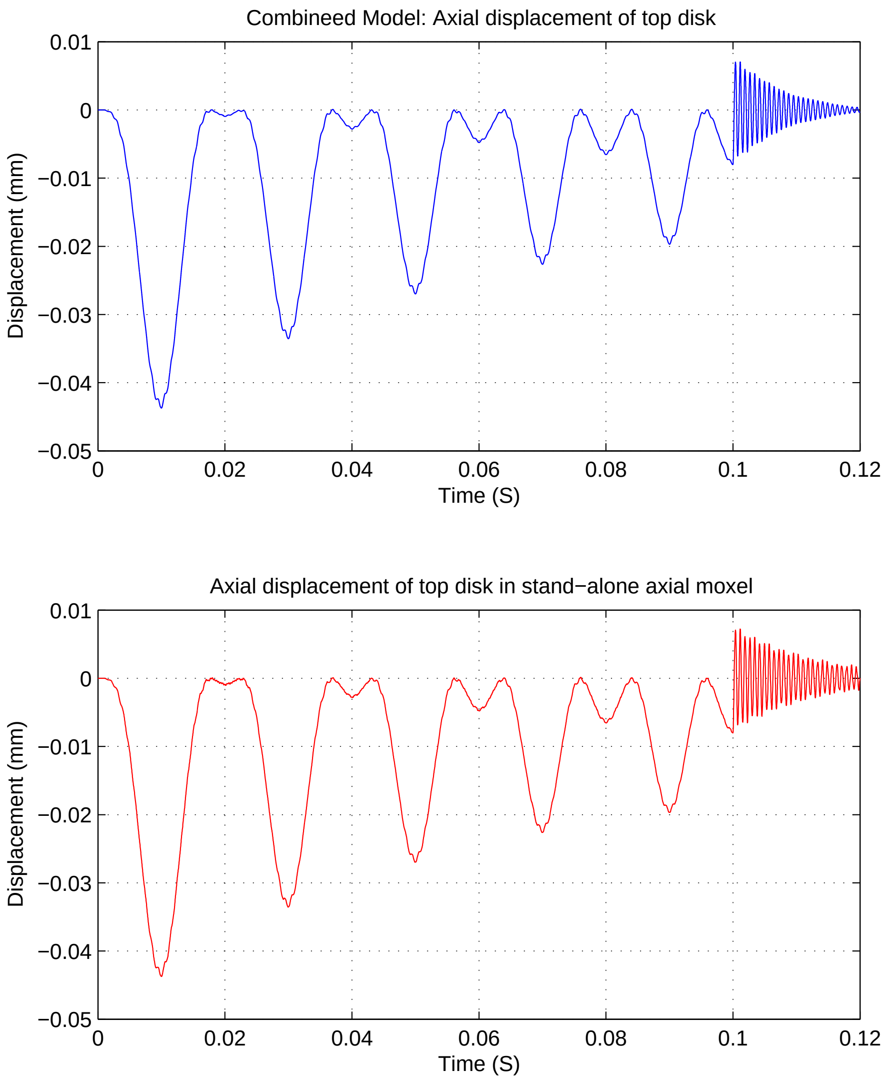

Figure 8.9: Comparison between stand-alone axial model and combined model of the test transformer

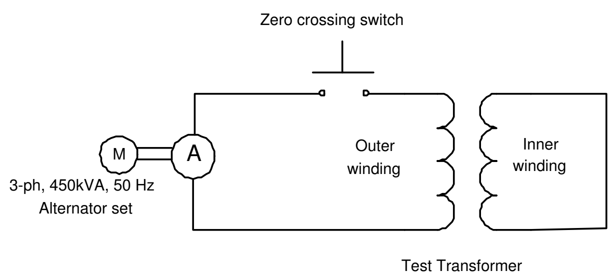

Figure 8.10: Single phase two-winding test transformer

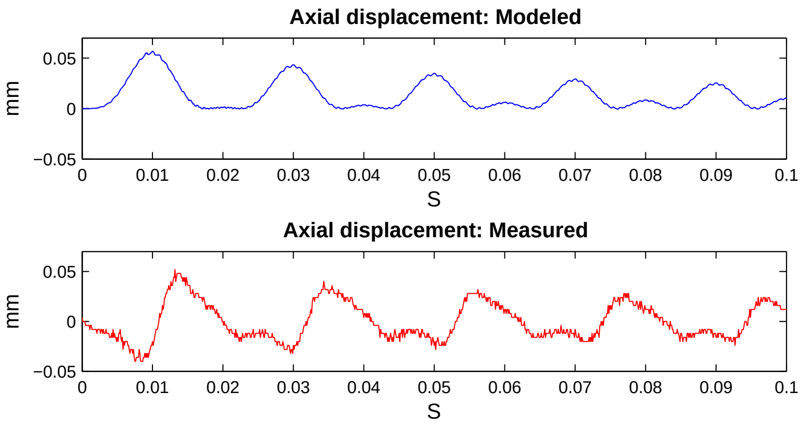

Figure 8.11: Simulated and measured results of axial displacement at a pre-stress of 7.1 N/mm^2

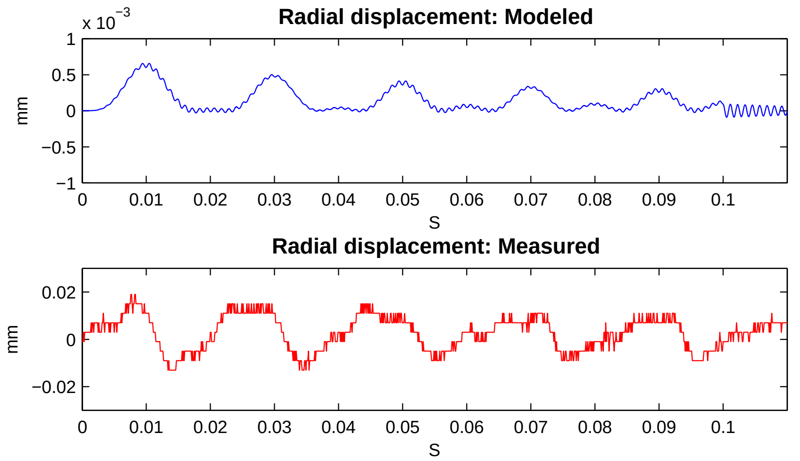

Figure 8.12: Simulated and measured results of radial displacement at a pre-stress of 7.1 N/mm^2

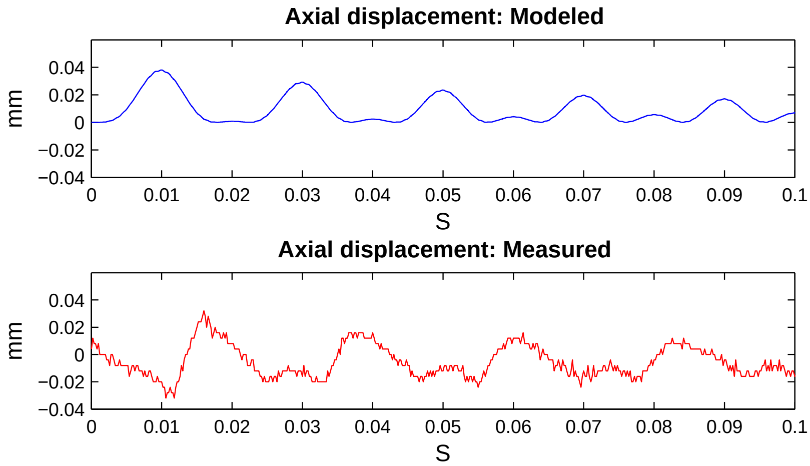

Figure 8.13: Simulated and measured results of axial displacement at a pre-stress of 14 N/mm^2

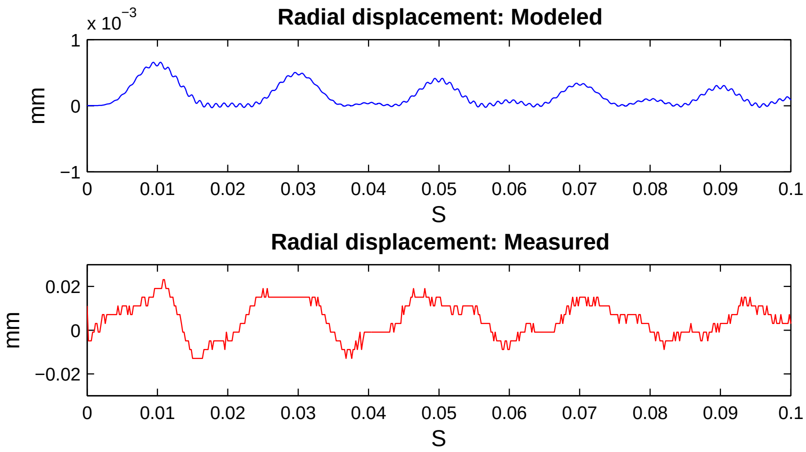

Figure 8.14: Simulated and measured results of radial displacement at a pre-stress of 14 N/mm^2

8.9 Discussion

There is no significant difference between the axial response of the combined and stand-alone models (Fig 8.9). This can be attributed to the stiffness of the transformer resulting in a very small displacement in the radial direction. The combined model of low stiffness designs and in larger transformers (where larger radial displacement are expected) can be different from stand-alone models due the axial friction forces between the core and the inner winding.

The modeling of hysteresis is approximate and the recovery time of the pressboard has not been included in the model, nor has the visco-elastic behaviour of the oil impregnated pressboard been comprehensively modeled. It is to be expected therefore, that there will be a discrepancy between measured and predicted displacements. Under the circumstances, a discrepancy of 20% to 30% can be taken as pointing to a reasonably representative model.

A loss in pre-stress was observed during the successive application of current. This shows that in-service, a transformer may lose its applied pre-stress, especially after the event of a short-circuit and become more susceptible to damage.

The measured axial displacement in Figures 8.11 and 8.13 is larger (20%-30%) than the simulated displacement. This could be due to the inaccuracy of measurement, hysteresis (which was neglected), disk profile, recovery time of pressboard and visco-elastic behaviour of impregnated pressboard.

Inaccuracy: The inaccuracy can be reduced by using more accurate instruments designed to record very small displacements. The interference from the leakage magnetic field in transformers may make these measurements more difficult.

Hysteresis: It has been established that the pressboard is a non-linear material and has significant hysteresis (Chapter 7). After the initial impact of force (during first half cycle), the pressboard between the disks is squeezed and reduced in thickness. The pressboard material does not return to its normal thickness before the second half cycle of the force but shows a longer time constant for recovery. This is evident from the recorded waveforms in Figures 8.11 and 8.13, where it is clear that the thickness is reduced and it is only restored to its original value after several cycles of oscillation.

Profile: The interface profile of the mass in the stress-strain measuring rig was smooth. Contrary to the test transformer's disk profile (the mass element) which was built by radially wound, paper covered coils of 5 conductors (2mm thick) as shown in the Figure 8.16. It is common practice that the edges of the conductors are made round to reduce the chances of high electric stresses. Hence the vertical spacer (pressboard), will exhibit a lower stiffness and a larger displacement, due to the profile of the disk

Time of recovery: The time of recovery of the pressboard material is also longer than the period of the applied forces. This in turn showed a reduction in the stiffness in the later cycles of the force and the recovery of the material dimensions was due to the decaying force. If the force peaks were of similar magnitude of the 1^{st} peak, the recovery of the pressboard material would have been even slower.

Visco-elastic behaviour: An impact force squeezes oil out of the impregnated pressboard. The process of oil returning back into the pressboard material is slow because it happens at a pressure close to the atmospheric pressure [Patel, 1972]. The oil squeeze-out reduces the stiffness of the material which recovers with inward flow of oil.

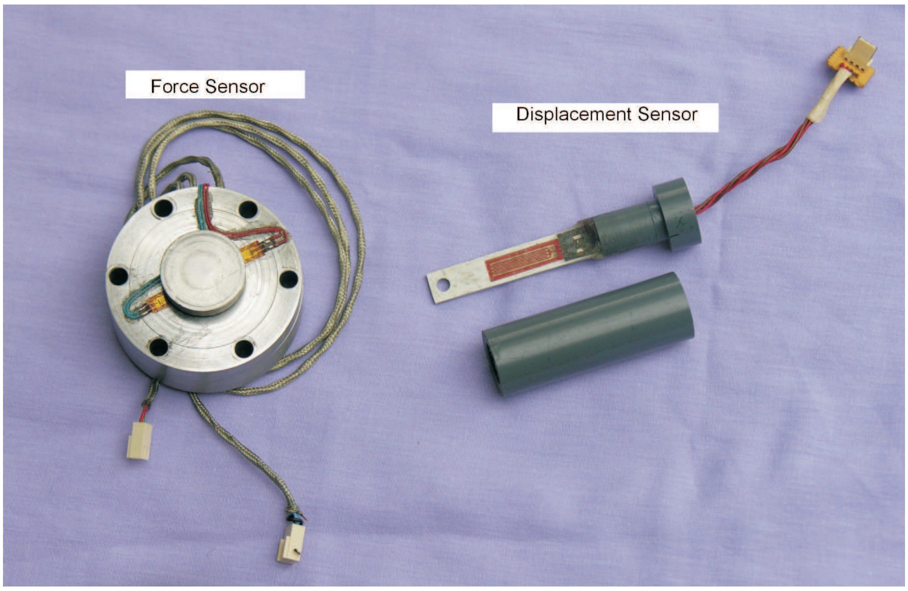

Figure 8.15: Construction of the force and displacement sensors. The force sensor was used to measure the pre-stress and the two displacement sensors were used for axial and radial displacement

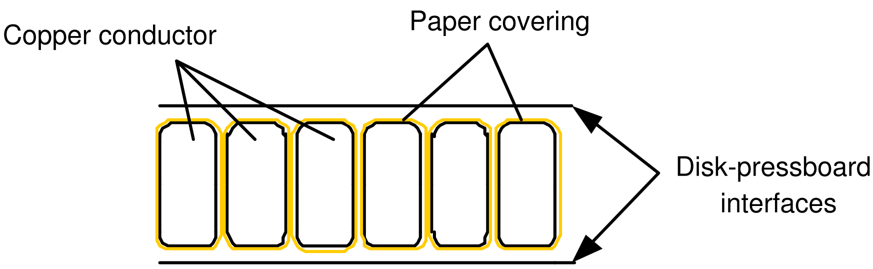

Figure 8.16: The cross-section of the transformer disk showing the profile of the area interfacing with the vertical spacers (pressboard)

The measured radial displacements are significantly larger than the simulated radial displacements. This was due to the complexity of coupled behaviour of the transformer and the inaccuracy of the instrumentation used. The radial displacement was expected to be a few μm, which is extremely difficult to measure with the type of instrumentation used.

The displacement sensor employed to measure the radial displacement was a strain gauge type and is shown in the Figure 7.4. The force sensor was also a strain gauge type. The sensors were used for their simplicity and inherited property of not being effected by the magnetic field. The sensors had the capability of picking up some effects of the axial movement which was in phase with the radial response. Qualitatively, the measured and modeled radial displacement show reasonable correlation.

The test transformer was of very high stiffness and had a high natural frequency. Also the injected current was not large enough to produce significant displacements, which was one of the reasons for the simulated displacement not going negative.

8.10 Conclusions

1. The difference between simulated and measured response is within 20%-30% for axial behaviour. In view of the complexity of the model and challenges in measurement, this discrepancy is to be expected.

2. Qualitatively, the measured radial response was similar to the simulated displacement. The difference between the measured and predicted radial responses is due to the complexity of measurement where it was difficult to separate the axial and radial movements. The larger measured radial displacement could also be due to the lose turns especially the outer turn of the disk where the displacement sensor was installed.

3. Bearing in mind the complexity of the mechanical system, predicted dynamic behaviour determined from the model, has been shown to be realistic and representative of the transformer.

4. There was no significant difference in response of the combined and stand-alone models of test the transformer. This can be attributed to the high stiffness of the test transformer where the predicted radial displacement was negligible. In low stiffness designs or in larger transformers, where radial displacements may be larger, the responses of the models may be significantly different.

5. Loss in pre-stress between the successive applications of current showed that, after a short circuit, a transformer may loose its applied pre-stress.

6. A significant hysteresis was shown by the pressboard material and the stiffness recovery time was long. This may lead to a failure if short circuits are frequent.

7. If a large number of approximating functions are used, the model may require greater computer resources to execute the model.

Chapter 9

Conclusion and recommendations

9.1 Conclusion

1. In terms of the objectives of this research,

   (a) It is been shown that the dynamic behaviour of a transformer winding is dependant on the dynamic characteristics of the oil impregnated pressboard and paper which form the electrical insulation system and the mechanical support system for the conductors in the coils of the winding.

   (b) These properties of the pressboard have been measured and after reasonable simplification have been incorporated in a comprehensive model in which the basic element is a single disk in a winding with axial and radial pressboard spacers.

   (c) The model has been tested experimentally and the discrepancy between the measured and predicted displacements range between 20% and 30%. Bearing in mind the complexity of the model and difficulties in the measurements, this discrepancy is to be expected. It can be assumed that with further refinements to the model and improvements in the measuring techniques, this discrepancy can be significantly reduced.

2. In addition the research has highlighted the following issues:

   (a) The axial movements of the windings produce much larger displacements than those in the radial direction. Although the radial forces are higher than the axial forces, the stiffness in the radial direction is also significantly higher than the axial stiffness, resulting in very small radial displacements.

   (b) Physically, the axial and radial behaviours are coupled but the high radial stiffness allows very small radial displacements and little or no extra friction to the axial movements. Hence, when the radial displacements are small, the radial and axial dynamic behaviours are independent of each other and can be studied separately. This statement is also valid for transformers where windings are designed as self supporting in the radial direction and likely to have very small radial displacements.

(c) The dynamic stress-strain characteristics show significant hysteresis, resulting in a slower recovery to the initial size and stiffness compared to the pulsating electromagnetic forces. Even with a very stable material (where the hysteresis is reduced to a much smaller value and the pre-stress is maintained), under a long duration fault, after first few cycles, the stiffness offered by the pressboard will reduce, resulting in larger displacements which could lead to a mechanical failure of the windings.

(d) Traditionally, the tripping time of the protection of power transformers is based on the heating effects of the conductors used in the windings. These have a longer time constant than the stiffness recovery time of the pressboard. Older transformers are even more susceptible to this type of failure due to the loss of pre-stress due to ageing [Krause, 2003]. Faster and intelligent tripping is required to avoid failures due to reduced stiffness and pre-stress.

9.2 Recommendations for further research

This work has explored the nonlinear mechanical behaviour of transformer pressborad and implemented it in a model of a complete transformer. Patel's model [Patel, 1972] has been significantly extended. There is now a solid base upon which further research can be conducted:

Dynamic properties of the pressboard

- Techniques need to be developed to determine the properties of the pressboard to a higher degree of accuracy under all representative values of pre-stress
- Special non-contact type displacement sensors will be needed to prevent interference with the behaviour of the pressboard
- The electromagnetic forces in a 50 Hz system have a frequency of 100 Hz. This necessitates the measurement of dynamic stress-strain characteristics at or close the frequency of 100 Hz to determine realistic parameters of modeling.

The separation of axial and radial movement

This could possibly be achieved by installing sensors at the axial geometrical center of the winding where little or no forced axial movement is expected. This applies when the windings are stiff in the axial direction, have no initial displacement and are of the same height. Special non-contact type sensors may provide the solution

The conditions under which the axial and radial behaviours can be studied independently need further investigation.

The extension of this work to include layer type winding needs to be studied.

References

C M Arturi. Force calculation in transformer windings under unbalanced MMFs by a non-linear finite element code. In *IEEE Transactions on Magnetics*, volume 28, pages 1363–1366, March 1992.

R E Ayres, G O Usry, M R Patel, and R B Steel. Dynamic measurement during short circuit testing of transformers, part 2- test results ans analysis. In *IEEE Trasactions on Power Apparatus and Systems*, volume PAS-94, pages 198–206, 1975.

E Billing. Mechanical stress in transformer windings. In *IEE Transactions*, pages 227–248, 1946.

Final Report: Cigré Working Group 12-04. Calculation of short-circuit forces in transformers. In *Electra*, number 67, pages 29–75. Cigré, 1979.

A C Franklin and D P Franklin. *The J & P Transformer Book*. Butterworth & Co. (Publishers) Ltd, England, 11th edition, 1983.

B Hague. *Electromagnetic Problems in Electrical Engineering*. Oxford University Press London: Humpherey Milford, 1929.

K Hiraishi. Mechanical strength of transformer winding under short-circuit conditions. In *IEEE Transactions on Power Apparatus and Systems*, pages 2381–2390, October 1971.

Y Hori and K Okuyama. Axial vibration analysis of transformer winding under short circuit conditions. pages 433–451. IEEE Transactions on Power Apparatus and Systems, March/April 1990.

IEC 60076. *Power Transformers - Ability of withstand Short-circuit*. IEC, 2nd edition, 1992. Part-5.

Y V Tournier J P Martin, J Wendling. Specifics of the short-circuit behavior of concentrically-wound transformers and autotransfromers. In *IEEE Transactions on Power Apparatus and Systems*, volume PAS-99, pages 2069–2077, Nov/Dec 1980.

C Krause. The variation of the clamping pressure of power transformers due to operational temperature cycles and loss of pressure with time. In *Cigré Study Committee A2 Transformers Colloquium, Merinda*. CIGRE, 2003.

A B Madin and J D Whitaker. The dynamic behaviour of transformer winding under axial short-circuit. In *IEE Proceedings*, volume 110, pages 535–550, March 1963a.

A B Madin and J D Whitaker. The dynamic behaviour of transformer winding under axial short-circuit forces. volume 110, pages 535–550, March 1963b.

E T Norris. Mechanical strength of power transformers in service. In *IEE Proceedings*, pages 289–300. IEE, Feb 1957.

M R Patel. *Dynamic response of transformer windings and clamps under axial short-circuit forces*. PhD thesis, Rensselaer Polytechnic Institute, Troy, New York, 1972.

M R Patel. Dynamic response of power transformers under axial short circuit forces part-1 winding and clamps as individual components. In *IEEE Transactions on Power Apparatus and Systems*, volume PAS-92, pages 1558–1566, 1973a.

M R Patel. Dynamic response of power transformers under axial short circuit forces part-II winding and clamps as a combined system. In *IEEE Trasactions on Power Apparatus and Systems*, volume PAS-92, pages 1567–1575, 1973b.

A Pichon and B Hochart. Problems concerning the behaviour of transformers on short-circuit. Technical Report 142, Cigré, 1958.

M R Saravolac, P A Vertigen, C A Sumner, and W H Siew. Design verification criteria for evaluating the short circuit withstand capability if transformer inner windings. In *Cigré 2000, paper 12-208*, 2000.

M G Say. *The Performance and design of Alternating Current Machines*. Sir Issak Pitman & Sons, Ltd, London, 3rd edition, 1958.

D O Swihart and L S McCormick. Short circuit vibration of shell form power transformer. In *IEEE Transactions on Power Apparatus and Systems*, volume PAS-99, pages 800–810, March/April 1980.

D O Swihart and D V Wright. Dynamic stiffness and damping of transformer pressboard during axial short-circuit vibration. In *IEEE Trasactions on Power Apparatus and Systems*, volume PAS-95, pages 721–728, March/April 1976.

S Timoshenko, DH Young, and W Weaver(JR). *Vibration Problems in Engineering*. John Wiley & Sons, Inc., 4th edition, 1974.

Y Tournier, G Ebersohl, A Ciniero, S Yakov, A B Madin, and J D Whitaker. A study of the dynamic behaviour of transformer windings under short-circuit conditions. In *Cigré Conférence Internationale des Grands Réseaux Électriques à Haute Tension*, number 143, 1962a.

Y Tournier, G Ebersohl, A Ciniero, S Yakov, A B Madin, and J D Whitaker. Supplement to paper 143. In *Cigré Conférence Internationale des Grands Réseaux Électriques à Haute Tension*, number 143a, 1962b.

Y Tournier, M Richard, A Ciniero, S Yakov, A B Madin, and J D Whitaker. A study of the dynamic behaviour of transformer windings under short-circuit conditions. In *Cigré Conférence Internationale des Grands Réseaux Électriques à Haute Tension*, number 134, 1964.

M Waters. The measurement and calculation of electromagnetic forces in concentric transformer windings. In *IEEE Transactions*, pages 35–46, 1953.

M Waters. *The Short-Circuit Strength of Power Transformers*. Macdonald & Co (Publishers) Ltd, Golf House, 2 Portman Street, London, W.1, 1966.

G B Watts. A mathematical treatment of dynamic behaviour of a power-transformer winding under axial short-circuit forces. In *IEE Proceedings*, volume 110, pages 551–560, 1963.

Appendix A

Matlab source codes

This code is where the model is defined and all input parameters are entered for electromagnetic forces, and dynamic calculation for input to the SIMULINK® models.

A.1 Input code

```
% Inputs for the programmes to calculate the electromagnetic forces,
% mechanical characteristics of the transformer in axial and radial
% direction and inputs to the simulink model.
% This file is formatted to be printed in the thesis (in latex)
clear
% Winding details (dimensions of winding)
% Total number of disks in inner winding
disks_in=5;
% Total number of disks in outer winding (Uniform disks assumed)
disks_ot=5;

% Number of turns in each disk of inner winding
turns_in=5;
% Number of turns in each disk of outer winding
turns_ot=5;

% Number of radial ribs of inner winding = number of clocks
ribs_in=  4;
% Axial thickness of each rib in inner winding.
ribs_t_in = 12*1e-3;    % m
% Radial width of each rib in inner winding
ribs_w_in = 12*1e-3;    % m

% Number of radial ribs of outer winding
ribs_ot = 6;
```

```
% Axial thickness of each rib of outer winding
ribs_t_ot = 12*1e-3;    % m
% Radial width of each rib of the outer winding
ribs_w_ot = 12*1e-3;    % m

% Axial insulation dimensions of inner winding
% Thickness of the inner clack
clack_t_in = 5 *1e-3;  % m
% Width of the inner clack
clack_w_in = 40 *1e-3; % m
% Length of the inner clack
clack_l_in = 60 *1e-3; % m

% Axial insulation dimensions of outer winding
% Thickness of the outer clack
clack_t_ot = 5 *1e-3;  % m
% Width of the outer clack
clack_w_ot = 40 *1e-3; % m
% Length of the outer clack
clack_l_ot = 60 *1e-3; % m

% Paper insulation thickness wrapped on the conductor
% Thickness of the paper insulation wrapped on the inner winding
t_ins_in = 0.3  *1e-3;          % m
% Thickness of the paper insulation wrapped on the outer winding
t_ins_ot = 0.3  *1e-3;          % m

% Winding conductor dimensions
% Width of inner winding conductor
w_in = 12    *1e-3;                      % m
% Thickness of outer winding conductor
t_in = 2     *1e-3;                      % m
% Total thickness of the inner conductor including insulation thickness
cond_in = w_in*t_in;
% Inner conductor area including paper insulation
in_cond_ar_p= cond_in*2*t_ins_in;

% Width of outer winding conductor
w_ot = 12    *1e-3;                      % m
% Thickness of outer winding conductor
t_ot = 2     *1e-3;                      % m
% Total thickness of inner winding conductor including insulation
cond_ot = w_ot*t_ot;
% Outer winding conductor area including paper insulation
```

```
ot_cond_ar_p= cond_in*2*t_ins_in;

% Total thickness of inner conductor if used in a bundle
% Number of conductors in the bundle in inner winding
cond_bundle_p = 1;
% Number of conductors in the bundle of outer winding
cond_bundle_s = 1;

% Core and insulation cylinder dimensions
% Effective diameter of core
core_dia = 120       *1e-3;        % m
% Thickness of inner winding cylinder
cyl_thick_in = 40   *1e-3;         % m
% Thickness of the outer winding cylinder
cyl_thick_ot = 40    *1e-3;        % m
% Insulation between core and inner winding
ins_corewind_in = 50*1e-3          % m

%Insulation dimensions on winding end insulation
% Inner winding insulation on top side of winding
ins_wind_tp_in = 60 *1e-3;         % m
% Inner winding insulation on the bottom side of window
ins_wind_bt_in = 60 *1e-3;         % m
% Outer winding insulation on the top of the winding
ins_wind_tp_ot = 60 *1e-3;         % m
% Outer winding insulation on the bottom of the winding
ins_wind_bt_ot = 60 *1e-3;         % m

%Inner radius of inner winding
r_wind_in_in = core_dia/2 + ins_corewind_in + cyl_thick_in + ribs_t_in;
% Outer radius of inner winding
r_wind_in_ot = r_wind_in_in + turns_in*(t_in + 2*t_ins_in);
% Inner radius of outer winding
r_wind_ot_in = r_wind_in_ot + cyl_thick_ot + ribs_t_ot;
% Outer radius of outer winding
r_wind_ot_ot = r_wind_ot_in + turns_ot*(t_ot + 2*t_ins_ot);
% Radial thickness of inner winding
wind_t_in = r_wind_in_ot - r_wind_in_in;
% Radial thickness of inner winding
wind_t_ot = r_wind_ot_ot - r_wind_ot_in;
% Mean radius of inner winding
mean_r_wind_in = 1/2*(r_wind_in_in + r_wind_in_ot);
% Mean radius of outer winding
mean_r_wind_ot = 1/2*(r_wind_ot_in + r_wind_ot_ot);
```

```
% Mean length of inner winding turn
mean_lengthofturn_in = mean_r_wind_in *2*pi;
% Mean length of outer winding turn
mean_lengthofturn_ot = mean_r_wind_ot *2*pi;
% Mean length of whole winding turn
mean_length_wind_turn = 1/2*(mean_lengthofturn_in +mean_lengthofturn_ot);

% Radial Model INPUT DATA%
% Number of approximating functions
approx_fun=4;
% Mass density of copper=8920 Kg/sq m
m_density=8920;
% Young's Modulus of copper (Elasticity of copper)
E=1.685e10;
% Stiffness of insulation (Patel's 100000 psi converted to N/sq m)
K=1e5 *4.45/(25.4/1000)^2;

% Interturn insulation in inner winding
ins_interturn_in = clack_t_in + 2*t_ins_in;
% Interturn insulation in outer winding
ins_interturn_ot = clack_t_ot + 2*t_ins_ot;

area_in= turns_in*cond_in        % x-section area of inner winding disk
area_ot= turns_ot*cond_ot;       % x-section area of outer winding disk

% Input for the Electromagnetic forces Code (em_force.m)
% for prediction of electromagnetic forces using method of Images

i_in = 1000;               % current in inner winding
i_ot = 1000;               % current of outer winding
i_ot = -i_ot;              % Changing sign of the current
                           %(winding polarity)
Taw=20;                    % Taw=L/R= X/(2.pi.R.f)
f=50;                      % Frequency of the supply (50 Hz)

%distance of primary winding from top yoke to the center of 1st conductor
d_in_tp = ins_wind_tp_in + 0.5*w_in + t_ins_in;
% distance of primary winding edge from bottom yoke
d_in_bt = ins_wind_bt_in + 0.5*w_in + t_ins_in;
% distance of secondary winding edge from top yoke
d_ot_tp = ins_wind_tp_ot + 0.5*w_ot + t_ins_ot;
% distance of secondary winding edge from bottom yoke
d_ot_bt = ins_wind_tp_ot + 0.5*w_ot + t_ins_ot;
n_image=5 ;                                              % no of images
```

```
omega=2*pi*f;                                          % omega

%CONSTANTS
C=2*10^-7;                                             % Constant of force

% FORCE ON PRIMARY DUE TO PRIMARY
% Under sinusoidal currents
F_inr=[];          % Force as time function on inner winding
F_otr=[];          % Force as function of time on outer winding
time=[];           % Time vector

for t=0: 0.001: 0.1;       % Duration of fault
    % Current as time function
    I_in =i_in*disks_in*(sin(omega*t-pi/2) + exp(-t/(Taw/omega)));
    % Current as time function
    I_ot =i_ot*disks_ot*(sin(omega*t-pi/2) + exp(-t/(Taw/omega)));
    time=[time t];      % Time matrix
em_force02;             % em force calculation code
% Adding force on each conductor due to all inner conductors
F_inr = [F_inr, F_in];
% Adding force on each conductor due to all outer conductors
F_otr = [F_otr, F_ot];
end
F_inr = F_inr';
F_otr = F_otr';
T = time';

ax_mech02  % Mechanical behaviour calculation code in axial direction
rd_mech03  % Mechanical behaviour calculation code in radial direction
ang_var    % Angle defining code along the circumference of the disk

sign =1

%Components for SIMULINK model
%Damping= damping coefficient * volume of the disk
d_in=175*0.03*area_in*mean_lengthofturn_in*1000%0;
d_ot=3;
d_r = 3;

% unit conversion
stress_strain;
stress=175* stress;
strain=strain;
q=1;
```

```
mu  =0.5;

%PLOTTING
subplot(2,3,1), plot(time, real(F_inr))
grid
xlabel('Time(S)')
ylabel('Force (N)')
title('Radial force on inner winding')

subplot(2,3,2), plot(time, imag(F_inr))
grid
xlabel('Time(S)')
ylabel('Force (N)')
title('Axial force on inner winding')

subplot(2,3,4), plot(time, real(F_otr))
grid
xlabel('Time(S)')
ylabel('Force (N)')
title('Radial force on outer winding')

subplot(2,3,5), plot(time, imag(F_otr))
grid
xlabel('Time(S)')
ylabel('Force (N)')
title('Axial force on outer winding')

subplot(2,3,3), bar(ax_nat_fre)
grid
xlabel('Number')
ylabel('Frequency (Hz)')
title('Axial natural frequencies')

subplot(2,3,6), bar(rd_nat_fre)
grid
xlabel('Number of natural frequency')
ylabel('Frequency (Hz)')
title('Radial natural frequencies')
```

A.2 Electromagnetic force

```
% em_force02.m
% This code calculates the value of the electromagnetic force applied on
% the each disk/conductor of winding in a two winding transformer. The
% input to this code comes from the inp_mod file

% % % %FORCE ON PRIMARY DUE TO PRIMARY
% overall axial thickness of inner winding disk including insulation (paper
% & clack)
wd_in = w_in + 2*t_ins_in + clack_t_in;
% overall axial thickness of outer winding disk including insulation (paper
% & clack)
wd_ot = w_ot + 2*t_ins_ot + clack_t_ot;
% total axial length of total no of disks (inner)
ln_in = wd_in *(disks_in -1);
% total axial length of total no of disks (outer)
ln_ot = wd_ot *(disks_ot -1);
%
% distance to the center of bottom disk (inner winding)
d_bt_in = -ln_in/2;
% distance to the center of the top disk (inner winding)
d_tp_in =  ln_in/2;
%
% distance to the center of bottom disk (outer winding)
d_bt_ot = -ln_ot/2;
% distance to the center of bottom disk (outer winding)
d_tp_ot =  ln_ot/2;
%Calculating height of window
l_window = d_in_tp + (ln_in + w_in + 2*t_ins_in) +d_in_bt;

% Position of inner winding
d_in(1:disks_in) = d_tp_in:-wd_in :d_bt_in;
% Position matrix of inner winding
pos_wind_in = mean_r_wind_in + d_in*j;

% Position of outer winding
d_ot(1:disks_ot) = d_tp_ot:-wd_ot :d_bt_ot;
pos_wind_ot = mean_r_wind_ot + d_ot*j;

c_in=C*mean_length_wind_turn*I_in^2;
c_ot=C*mean_length_wind_turn*I_ot^2;
c_in_ot=C*mean_length_wind_turn *I_in *I_ot;
```

```
F_in = zeros(disks_in ,1);                    % Force on the inner winding
F_ot = zeros(disks_ot ,1);                    % Force on the outer winding

%FORCE ON INNER WINDING DUE TO INNER WINDING%%%%

mat_1=pos_wind_in;
mat_2=pos_wind_in;
d_mtom;         % Calculating distance from matrix_1 to matrix_2
Cp=c_in;
f_mtom;         % Calculating the force on each inner winding turn (f_mtom)
F_in = Force;   % Total force on inner winding

% FORCE ON OUTER WINDING DUE TO OUTER WINDING %%%
%Distance {d_bt_ot} in mm to the center of the far most secondary
%conductor towards the bottom

mat_1=pos_wind_ot;
mat_2=pos_wind_ot;
d_mtom;
Cp=c_ot;
f_mtom;
    F_ot = Force;

% FORCE BETWEEN INNER AND OUTER %%%
%   On inner winding due to outer winding%%%
mat_1=pos_wind_in;
mat_2=pos_wind_ot;
d_mtom;
Cp=c_in_ot;
f_mtom;
    F_in=F_in + Force;    % Adding force to the total force

%%% On outer winding due to inner winding %%%
mat_1=pos_wind_ot;
mat_2=pos_wind_in;
Cp=c_in_ot;
d_mtom;
f_mtom;
    F_ot= F_ot + Force;    % Adding force to the total force

% FORCE ON THE INNER WINDING DUE TO ITS IMAGE POSITIONS %%%
%Force due to the images of top plane on inner winding
  mat_1=pos_wind_in;
```

```
  for a=1: n_image;
      mat_2=pos_wind_in+(-1)^(a+1)*(2*d_in_tp + ln_in+ (a-1)*2*l_window)*j;
      mat_n2=-1*real(mat_2)+j*imag (mat_2);

      %Calculations of forces on
      %inner winding
      %d_m_m;
      d_mtom;
      Cp=c_in;
      f_mtom;
         %F_in = F_in + conj(Force);
         F_in = F_in + Force;
         %Fup1 = Force;
      %force calculation in "-ve x" direction
      %d_mtonx;
      %d_m_nx;
      d_mtonx;
      f_mtom;
         %F_in = F_in + conj(Force);
         F_in = F_in + Force;
%          %Fup2=Force;
  end

% %Force due to images of bottom plane

  for a=1:n_image;
      mat_1=pos_wind_in;
      mat_2=pos_wind_in -(-1)^(a+1)*(2* d_in_bt +ln_in +(a-1)*2*l_window)*j;
      mat_n2=-1*real(mat_2)+j*imag (mat_2);
      d_mtom;
      %d_m_m;
      Cp=c_in;
      f_mtom;
           %F_in = F_in + conj(Force);
              F_in = F_in + Force;
              %Fdn1= Force;
      %force calculation in "-ve x" direction
      d_mtonx;
      %d_m_nx;
      f_mtom;
           %F_in= F_in + conj(Force);
           F_in = F_in + Force;
           %Fdn2 = Force;
  end
```

```
%%%%%Y AXIS IMAGES OF OUTER WINDING

    mat_1 = pos_wind_ot;

    for a= 1: n_image;
      mat_2 = pos_wind_ot +(-1)^(a+1)*(2*d_ot_tp + ln_ot+ (a-1)*2*l_window)*j;
      mat_n2=-1*real(mat_2)+j*imag (mat_2);

     %Calculations of forces due to images on
     %      secondary

     d_mtom;
     Cp=c_ot;
     f_mtom;
          F_ot = F_ot + Force;

     %force calculation in "-ve x" direction
     d_mtonx;
     %d_m_nx;
     f_mtom;
         F_ot = F_ot + Force;
     end

 %Force due to images of bottom plane
for a=1:n_image;
     mat_1=pos_wind_ot;
     mat_2=pos_wind_ot-(-1)^(a+1)*(2*d_ot_bt + ln_ot + (a-1)*2*l_window)*j;
     mat_n2= -1*real(mat_2)+j*imag (mat_2);
     %d_m_m;
     d_mtom;
     f_mtom;
         F_ot = F_ot + Force;

     %force calculation in "-ve x" direction
     d_mtonx;
     f_mtom;
         F_ot = F_ot + Force;
 end

 %Forces on primary due to secondary images
%Top images
    mat_1=pos_wind_in;
```

```
    % inner winding
  for a=1: n_image;
    mat_2=pos_wind_ot+(-1)^(a+1)*(2*d_ot_tp+ ln_ot + (a-1)*2*l_window)*j;
    mat_n2=-1*real(mat_2)+j*imag (mat_2);

    % outer winding
    d_mtom;
      Cp=c_in_ot;
    f_mtom;
        F_in = F_in + Force;
    %force calculation in "-ve x" direction
    d_mtonx;
    f_mtom;
        F_in = F_in + Force;
  end
% Bottom images
  for a=1:n_image;
    mat_1=pos_wind_in;
    mat_2=pos_wind_ot -(-1)^(a+1)*(2* d_ot_bt + ln_ot +(a-1)*2* l_window)*j;
    mat_n2= -1*real(mat_2)+j*imag (mat_2);
    d_mtom;
    f_mtom;
        F_in = F_in + Force;

  %%force calculation in "-ve x" direction
    d_mtonx;
    f_mtom;
        F_in = F_in + Force;
  end

%Forces on secondary due to primary images

  mat_1=pos_wind_ot;

  for a=1: n_image;
    mat_2=pos_wind_in + (-1)^(a+1)*(2*d_in_tp + ln_in+ (a-1)*2*l_window)*j;
    mat_n2=-1*real(mat_2)+j*imag (mat_2);

    %Calculations of
    %     primary
    %d_m_m;
    d_mtom;
    Cp=c_in_ot;
    f_mtom;
```

```
          F_ot = F_ot + Force;
      %force calculation in "-ve x" direction
      d_mtonx;
      %d_m_nx;
      f_mtom;
          F_ot = F_ot +Force;

  end

  % %Force on inner winding due to images of bottom plane

   for a=1:n_image;
      mat_1=pos_wind_ot;
      mat_2=pos_wind_in -(-1)^(a+1)*(2*d_in_bt+ ln_in +(a-1)*2*l_window)*j;
      mat_n2=-1*real(mat_2)+j*imag (mat_2);
      %d_m_m;
      d_mtom;
      Cp=c_in_ot;
      f_mtom;
         F_ot = F_ot + Force;

      %force calculation in "-ve x" direction
      %d_m_nx;
      d_mtonx;
      f_mtom;
         F_ot = F_ot + Force;
   end

% X-axis images
% Forces on inner winding due to its own images
 mat_1=pos_wind_in;
 mat_2=-1*real(pos_wind_in)+j* imag(pos_wind_in);

 %Calculations of forces on
 % on inner winding due to inner winding
      %d_m_m;
      d_mtom;
      Cp=c_in;
      f_mtom;
          F_in = F_in + Force;

% Force on inner winding due to outer winding
     mat_2=-1*real(pos_wind_ot)+j*imag(pos_wind_ot);
     %d_m_m;
```

```
    d_mtom;
    Cp=c_in_ot;
    f_mtom;
        F_in = F_in + Force;

% Force on outer winding due to inner winding
mat_1=pos_wind_ot;
    mat_2=-1*real(pos_wind_in)+j*imag(pos_wind_in);
    %d_m_m;
    d_mtom;
    Cp=c_in_ot;
    f_mtom;
        F_ot = F_ot + Force;

% Force on secondary due to secondary

    mat_2=-1*real(pos_wind_ot)+j*imag(pos_wind_ot);
    %d_m_m;
    d_mtom;
    Cp=c_ot;
    f_mtom;
        F_ot = F_ot + Force;
```

A.2.1 Smaller routines used in electromagnetic calculation

```
%d_mtom, routine to calculate distance

clear dist;
dist=zeros(length(mat_1), length(mat_2));
clear x; clear y;
for x=1: length(mat_1);
   for y=1: length(mat_2);
        dist(x,y)=mat_1(x)-mat_2(y);
   end
end
```

```
%d_mtonx:calculation of distance for "-x" side
dist=zeros(length(mat_1), length(mat_n2));
clear x; clear y;
for x=1: length(mat_1);
   for y=1: length(mat_n2);
        dist(x,y)=mat_1(x) - mat_n2(y);
   end
end
```

```
 %Forces between two windings

force=zeros(size(dist));

for x=1: length(mat_1);
   for y=1: length(mat_2);

          if dist(x,y)==0;
          force(x,y)=0;
          elseif dist(x,y)~=0;
       force(x,y)=-Cp/dist(x,y);
      end
          end
end
Force=sum(force,2);
```

A.3 Code related to axial dynamic behaviour

```
%%ax_mech02--Axial dynamic behaviour related code
%% Code for calculating the natural frequencies of primary and secondary
%% windings. Only two windings are analyzed. The code also generates the
%% output for simulink model.

% Disk mass (the mass of insulation is supposed to be 20% of copper mass)
mass_disk_in = 1.2*(mean_lengthofturn_in) * turns_in *cond_in *m_density;
mass_disk_ot = 1.2*(mean_lengthofturn_ot) * turns_ot *cond_ot *m_density;

% Axial insulation thickness (between the disks)
ax_ins_t_in = clack_t_in +2*t_ins_in;
ax_ins_t_ot = clack_t_ot +2*t_ins_ot;

% Area of the clack supporting inner winding, only those ribs are
% entered here which are used for clacks
% The area of clack (axial insulation) in contact with the winding
```

```
ax_ins_area_in = wind_t_in *clack_w_in *ribs_in;
ax_ins_area_ot = wind_t_ot *clack_w_ot *ribs_ot;

% Mass Matrix
diag_mass_in = [mass_disk_in *ones(1,disks_in)];
diag_mass_ot = [mass_disk_ot *ones(1,disks_ot)];
diag_mass_a = [diag_mass_in, diag_mass_ot]; % diagonal of axial mass matrix
mass_a = diag(diag_mass_a);                  % mass matrix (axial)

% Stiffness Matrix
% Thickness of insulation between disks
ins_thick_in=[ins_wind_tp_in,clack_t_in*ones(1,(disks_in -1))...
    ,ins_wind_bt_in];
ins_thick_ot=[ins_wind_tp_ot,clack_t_ot*ones(1,(disks_ot -1))...
    ,ins_wind_bt_ot];

% Diagonal of stiffness matrix for inner winding
% Equivalent stiffness = K* Area/Length of insulation
for a=1:disks_in+1
    ins_stiff_in(1,a) = K *ax_ins_area_in/ins_thick_in(1,a);
end

for a=1:disks_in;
    dia_stiff_in(1,a) = ins_stiff_in(1,a)+ins_stiff_in(1,a+1);
end

sub_dia_stiff_in = ins_stiff_in (2:disks_in);%sub_diameter of inner winding
stiff_in_ax = (diag(dia_stiff_in)...
   -diag(sub_dia_stiff_in,-1)-diag(sub_dia_stiff_in,1))

% Stiffness matrix of outer winding
for a=1:disks_ot +1
    ins_stiff_ot(1,a)= K *ax_ins_area_ot/ins_thick_ot(1,a);
end

for a=1:disks_ot;
    dia_stiff_ot(1,a)=ins_stiff_ot(1,a)+ins_stiff_ot(1,a+1);
end

dia_stiff = [dia_stiff_in, dia_stiff_ot];

sub_dia_stiff_ot = ins_stiff_ot(2:disks_ot);        % sub_diameter outer
stiff_ot_ax = (diag(dia_stiff_ot)-diag(sub_dia_stiff_ot, -1)...
   -diag(sub_dia_stiff_ot,1))
```

```
% Main diagonal of stiffness matrix
dia_stiff = [dia_stiff_in , dia_stiff_ot];
% Sub-diagonal of stiffness matrix
sub_dia_stiff =[sub_dia_stiff_in , 0,  sub_dia_stiff_ot];
stiff_ax= (diag(dia_stiff)-diag(sub_dia_stiff , -1)-diag(sub_dia_stiff ,1));

ax_omega=eig(stiff_ax/mass_a);
ax_nat_fre=sqrt(ax_omega)/(2*pi);
```

A.4 Code related to radial dynamic behaviour

```
% Radial model using expansion of rings
% The file is same as rd_mech03 but the mass and stiffness matrix are
% corrected

%%%%Radial Model Input Data %%%%

area_in= pi *mean_r_wind_in^2;     %radial area of inner winding disk
area_ot= pi *mean_r_wind_ot^2;     %radial area of outer winding disk

x_sec_in = turns_in *in_cond_ar_p; %cross-sectional area of inner winding
x_sec_ot = turns_ot *ot_cond_ar_p; %cross-sectional area of outer winding

% total area of each inner rib in contact with winding
rib_area_in = ribs_w_in *w_in;
% total area of each outer rib in contact with winding
rib_area_ot = ribs_w_ot *w_ot;

%%%Moment of Inertia of inner and outer disks
%%Inner disk
Ii = turns_in*w_in *t_in^3 /12;        % per conductor of inner winding
Io = turns_ot*w_ot *t_ot^3 /12;        % of outer winding

%%%Mass Matrix "inner winding"
%diagonal matrix
diag1=[2*pi];
for m=1:approx_fun;
    diag1=[diag1 ((1/m)^2+1)*pi]
    diag1=[diag1 ((1/m)^2+1)*pi]
end
% mass of inner ring
diag_m_in = m_density *x_sec_in *mean_r_wind_in * diag1;
% mass of outer ring
```

```
diag_m_ot = m_density *x_sec_ot *mean_r_wind_in *diag1;
dia_mass=[diag_m_in , diag_m_ot];
mass_r=diag(dia_mass);   % mass matrix (including inner and outer winding)

for x=1:length(dia_mass);
    mass_rad(x,x) = 1/dia_mass(x);
end

%%Potential energy
%Elastic Stiffness Matrix
%potential energy due to extension of inner ring
u1 = area_in *E *pi/mean_r_wind_in;
%potential energy due to extension of outer ring
U1 = area_ot *E *pi/mean_r_wind_ot;

 for x=1:approx_fun
     u2(x) = (x^2 -1)^2 *pi;
 end

diag2=[];
 for x=1:approx_fun
      diag2= [diag2,u2(1,x), u2(1,x)];              % diagonal of PE matrix
 end
 %dia_in = [u1, diag1];%diagonal of elastic stiffness matrix for inner ring
%%%%INNER RING
%%% Potential Energy due to copper component of winding
stiff_el_in = E *li/mean_r_wind_in^3 *diag2;
% P.E due to elastic behaviour of inner winding
stiff_el_in = [u1, stiff_el_in];
stiff_el_ot = E *lo/mean_r_wind_ot^3 *diag2;
% P.E due to elastic behaviour of our winding
stiff_el_ot = [U1, stiff_el_ot];
stiff_elast= [stiff_el_in , stiff_el_ot];

stiff_elast=diag(stiff_elast);      % Stiff due to elastic potential energy

%%% stiffness due to insulation (pressboard/paper)

stiff1=[];
for theta = 0:(2*pi/ribs_in):(2*pi-(2*pi/ribs_in))
    for x=1:approx_fun
        F1(1,x) =theta*x;
    end
```

```
    stiff0 =[];
    for y=1:approx_fun
        stiff0= [stiff0 ,cos(F1(1,y)), sin(F1(1,y))];
    end
    stiff1 =[stiff1;stiff0];
end

stiff_inner=stiff1;
u0 = ones(length(stiff_inner(:,1))+1,1);
u1 = zeros(1,length(stiff_inner(1,:)));
u1 = [u1;stiff_inner];
stiff_inner = [u0, u1];        %stiffness of insulation ribs of inner ring

u=stiff_inner;
% position matrix with zero entries(includes inner and outer winding)
pos_inr = [stiff_inner, zeros((ribs_in+1), (approx_fun*2+1))];
% pressboard ribs position inner winding
pos_in = pos_inr'*pos_inr;
% stiffness of the inner winding for natural frequencies
stiff_in = K *rib_area_in* ribs_in *1/ribs_t_in *pos_inr'*pos_inr;

%%%%OUTER RING

stiff1 =[];
for theta = 0:(2*pi/ribs_ot):(2*pi-(2*pi/ribs_ot));
    for x=1:approx_fun
        F1(1,x) =theta*x;
    end

    stiff0 =[];
    for y=1:approx_fun
        stiff0= [stiff0 ,cos(F1(1,y)), sin(F1(1,y))];
    end
    stiff1 =[stiff1;stiff0];
end
%col 1 of the ribs position matrix of outer ring
u0 = ones(length(stiff1(:,1))+1,1);
%(partial) row 1 of the ribs position matrix of outer ring
u1 = zeros(1,length(stiff1(1,:)));
stiff_otr = [u1;stiff1];
stiff_otr = [u0,stiff_otr];
% producing a matrix \delta containing the difference of displacement of
% outer ribs
stiff_otr = [-stiff1 , stiff1];
```

```
size0=zeros(ribs_ot , length(mass_r)-approx_fun*4);
stiff_ot=[size0 , stiff_otr];

%Position of ribs of outer winding
pos_otr = (stiff_ot)'*(stiff_ot);       % of spring position matrix^2
pos_ot = pos_otr;
% assumed linear stiffness of winding to calculate natural frequencies
stiff_ot = K *rib_area_ot* ribs_ot *1/ribs_t_ot *pos_otr;

stiff= stiff_in +stiff_ot +stiff_elast;
stiff_ins = stiff_in +stiff_ot;


%Radial position of insulation for simulink

pos_r = pos_in +pos_ot;

% Vectors u & v and U & V
angl = 0;
    for x=1:approx_fun
        angle(1,x) = angl*x;
    end
    angle_u =[1];
    angle_v =[1];
    for y=1:approx_fun
        angle_u = [angle_u ,cos(angle(1,y)), sin(angle(1,y))];
%           angle_v = [angle_v, 2/y*sin(angle(1,y)), 2/y*cos(angle(1,y))];
    end

%%%%OUTPUTS

size(mass_r);
size(stiff);
rd_omega = sqrt(eig(stiff/mass_r));
rd_nat_fre=sort(rd_omega/(2*pi))
bar(rd_nat_fre)

%%%************************************

f_in = (real(F_inr));
f_ot = (real(F_otr));

a0=zeros(approx_fun*2,length(real(f_in)));
a0=a0';
```

```
%Forces on disk 1
Fr1_in = [f_in(:,1),a0];
Fr1_ot = [f_ot(:,1),a0];
%Fr1_in = [f_in(1,:);a0];
%Fr1_ot = [f_in(1,:);a0];
F_r = [Fr1_in, Fr1_ot];
%Forces on disk 2
```

A.4.1 Code used in radial behaviour for position of displacement

```
% To produce matrix for position
%Inner ring positions where displacement is measured
%(in the middle oif axial spacers)

ang1=[];
%posn = 8
posn=approx_fun*2;
angle = 2*pi/posn;
for theta = 0:angle:(2*pi-angle)
    for x=1:approx_fun
        F1(1,x) = [theta*x];
    end

    ang0=[1];
    for y=1:approx_fun
        ang0= [ang0,cos(F1(1,y)), sin(F1(1,y))];
    end
    ang1=[ang1;ang0];
end
r1 = zeros(1,length(ang1));
r1(1,1) =1;
ang1=[r1;ang1];

%Outer ring positions where dosplacement is measured
ang2=[];
posn2 = 8
angle = 2*pi/posn2;
for theta = 0:angle:(2*pi-angle)
    for x=1:approx_fun
        F1(1,x) = [theta*x];
    end

    ang0=[1];
    for y=1:approx_fun
```

```
        ang0= [ang0,cos(F1(1,y)), sin(F1(1,y))];
    end
    ang2=[ang2;ang0];
end
ang2=[r1;ang2];
```

Appendix B

Simulink models

The models and their components (subsystems) are presented in this chapter.

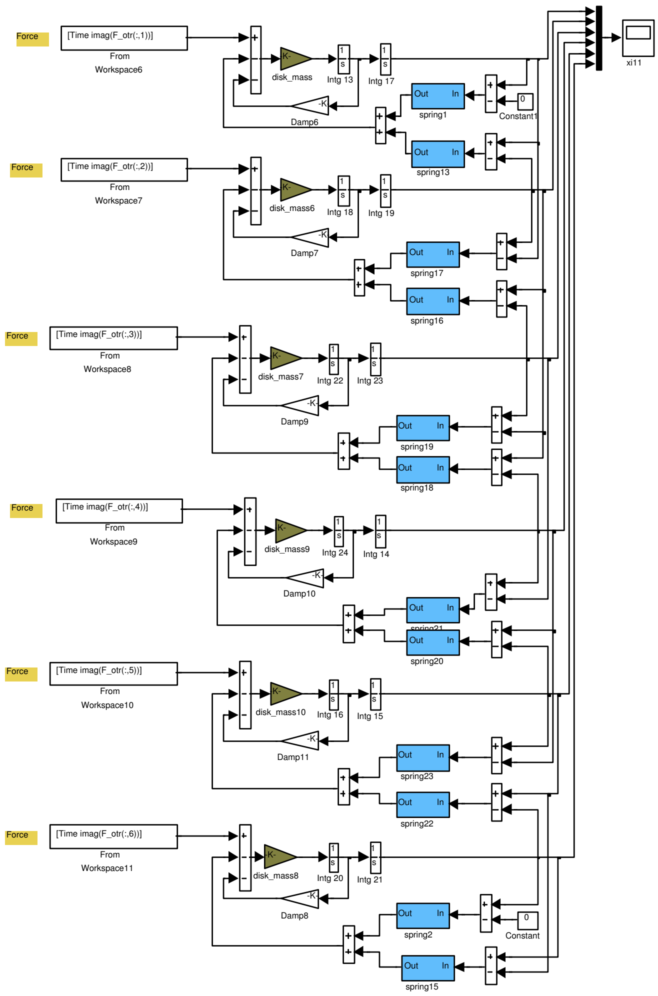

Figure B.1: Model to simulate axial behaviour of test test transformer implemented in Simulink

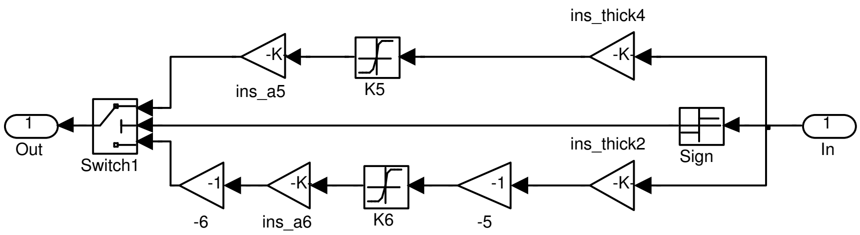

Figure B.2: Model of the spring used as subsystem in axial model of a winding (Fig B.1)

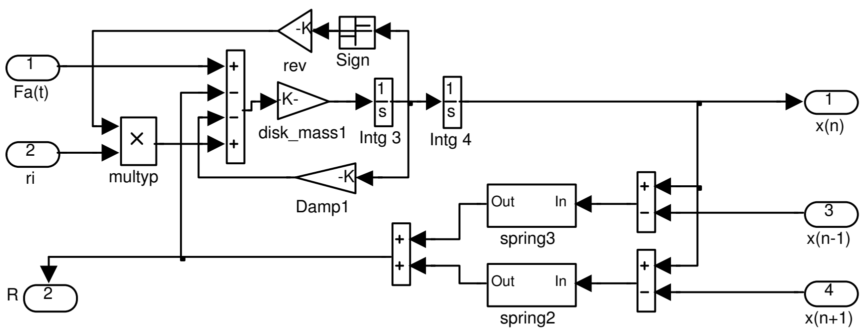

Figure B.3: Axial model of one disk used as a subsystem in the combined Simulink model (Fig B.4)

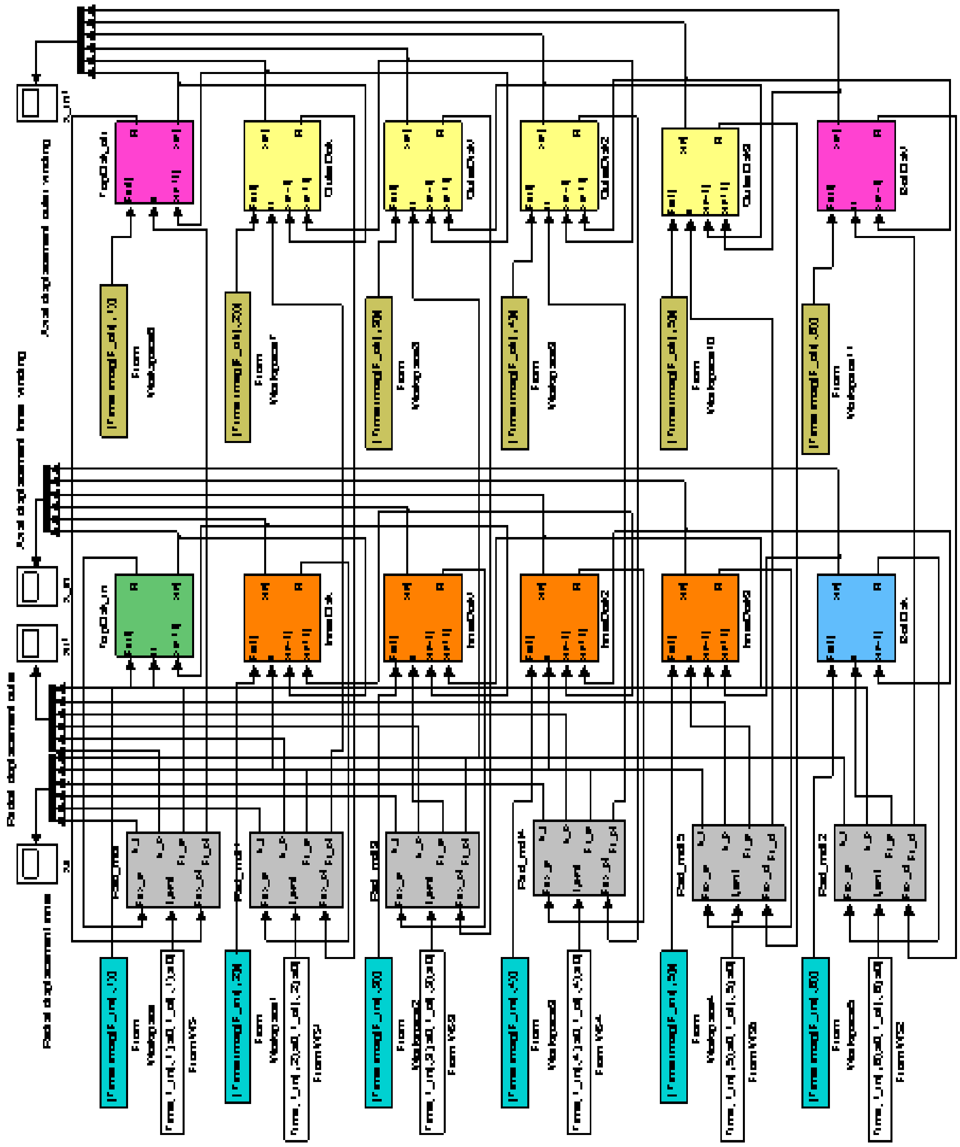

Figure B.4: The representation of the combined model of the test transformer implemented in simulink

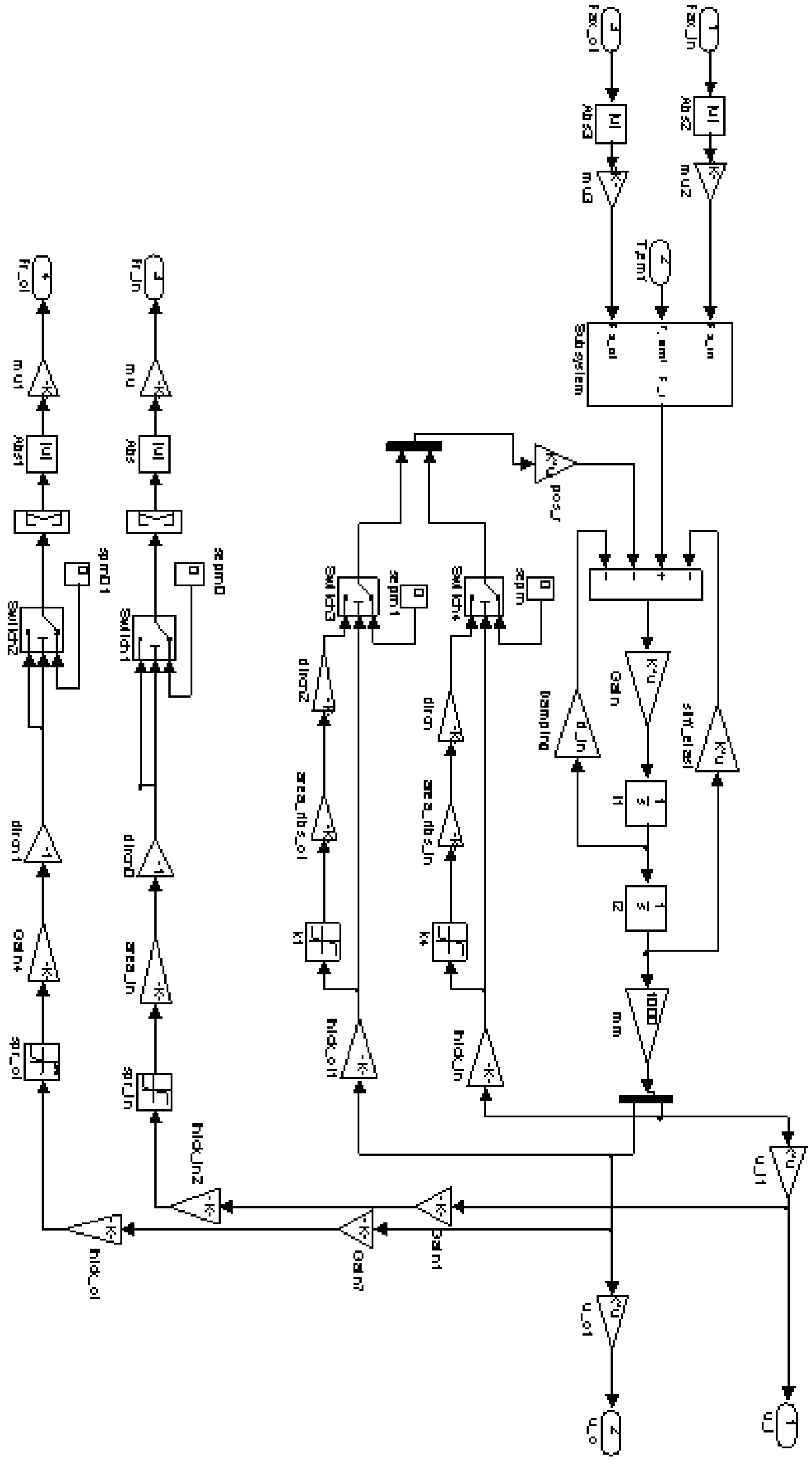

Figure B.5: Radial model of a set of inner and outer disks of the test transformer

Appendix C

Test transformer design and dimensions

C.1 Test transformer design details

The details of the core and winding design are given in this appendix. The Figure C.1. The winding winding design sheet is given in the Figure C.2 and the Figure C.3 is the winding sheet of outer winding.

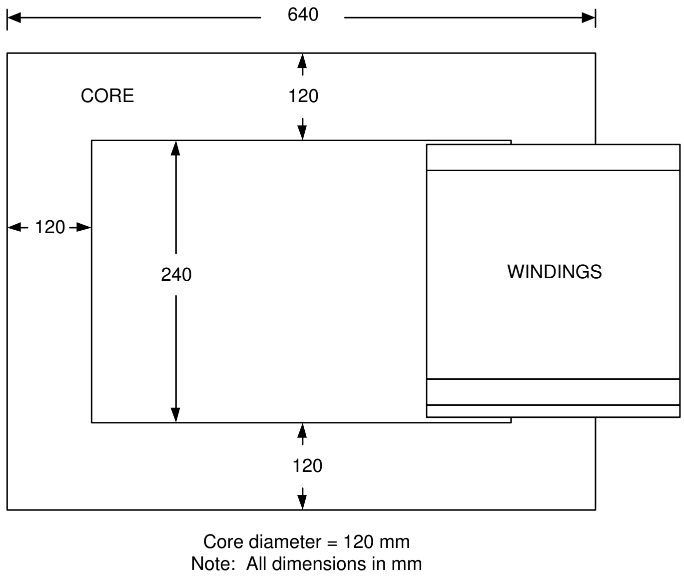

Figure C.1: Dimensions of the test transformer

Rotek Engineering A member of the Eskom Group	POWER DISTRIBUTION SERVICES WINDING SPEC SHEET PROJECT NO: ____________	Ref No.: ETCSF003 Rev No: 8.0 Date : 2003-11-28 Page : 1 of 1

SER No.		TRF MAKE	Rotek	FROM	WITS
DATE	2/20/2004	RATE MVA		ISSUED BY	A.T. Steyn
TYPE	A/W. CD.	kV		TURNS	30

INS DIST	102	TOP YOKE	51	BOT YOKE	51
WINDING HEIGHT	230				

COIL NO	1	6															
DIST		10															

- ADJUSTMENT						
+ ADJUSTMENT						
INS BETWEEN COILS	RIBS	8	CLACKS	10 x 38 x 18	THREADS	
COIL TYPE	CD 6					
COND BUNCH	11,4 X 2,0					
COIL NO	1					
COILS/TRF	1					
TURNS/COIL	5					
NUMBER LAYERS	5					

WAG DIMENSIONS					
FORMER	200 (628) 204 (642) x 230				
INNER	220 (T.Stick 8 mm.)				
AXIAL DIRECTION	128				
RADIAL DIRECTION	18				
CABLES/STRANDS NO x M/LIMB					
WOUND LIMBS x KG/LIMB					
COVERING No		YIELD POINT	Mpa 120	CLACK-BAND PITCH	N / A
WIND DIRECTION	Left	TRANSPORTATION	N /A	STRANDS IN COMM PAPER	N / A
OIL-GUILDING SHIELDS	INNER N /A				
	OUTER N /A				
COMPACTING FORCE	KN 30		ASSEMBLE FORCE	KN 20	

EXTRA TAPPINGS					
COIL No					
TURNS FROM START					
TURNS FROM BREAK					
MARKING					
VERIFIED		OEM		HISTORY	
REMARKS					
NAME	A.T. Steyn	SIGNATURE		DATE	2/20/2004

ORM RQ16D003.0

DISTRIBUTION: AS PER AUTHORISED LIST KEPT BY DOCUMENTATION CONTROL, PDS
THE REGISTERED RECIPIENT IS RESPONSIBLE FOR DESTROYING ALL SUPERSEDED DOCUMENTS.

Figure C.2: Design sheet of the inner winding of the test transformer

Rotek Engineering A member of the Eskom Group	POWER DISTRIBUTION SERVICES WINDING SPEC SHEET PROJECT NO: ______________	Ref No.: ETCSF003 Rev No: 8.0 Date : 2003-11-28 Page : 1 of 1

SER No.		TRF MAKE	Rotek	FROM	WITS
DATE	2/20/2004	RATE MVA		ISSUED BY	A.T. Steyn
TYPE	B/W. CD.	kV		TURNS	30

INS DIST	102	TOP YOKE	51	BOT YOKE	51
WINDING HEIGHT	230				
COIL NO	1	6			
DIST		10			

- ADJUSTMENT					
+ ADJUSTMENT					
INS BETWEEN COILS	RIBS	8	CLACKS 10 x 38 x 18	THREADS	
COIL TYPE	CD 6				
COND BUNCH	11,4 X 2,0				
COIL NO	1				
COILS/TRF	1				
TURNS/COIL	5				
NUMBER LAYERS	5				

WAG DIMENSIONS					
FORMER	274 (860) 278 (873) x 230				
INNER	294 (T.Stick 8 mm.)				
AXIAL DIRECTION	128				
RADIAL DIRECTION	18				
CABLES/STRANDS NO x M/LIMB					
WOUND LIMBS x KG/LIMB					
COVERING No	1,6 MM.	YIELD POINT	Mpa 120	CLACK-BAND PITCH	N / A
WIND DIRECTION	Left	TRANSPORTATION	N /A	STRANDS IN COMM PAPER	N / A
OIL-GUILDING SHIELDS	INNER N /A				
	OUTER N /A				
COMPACTING FORCE	KN 30	ASSEMBLE FORCE	KN 20		

EXTRA TAPPINGS					
COIL No	Tap One 5 tunns at bottom xo disc no 1 Tap 2 25 turns at bottom xo disc no 5				
TURNS FROM START					
TURNS FROM BREAK					
MARKING					
VERIFIED		OEM		HISTORY	
REMARKS					
NAME	A.T. Steyn	SIGNATURE		DATE	2/20/2004

ORM RQ16D003.0

DISTRIBUTION: AS PER AUTHORISED LIST KEPT BY DOCUMENTATION CONTROL, PDS
THE REGISTERED RECIPIENT IS RESPONSIBLE FOR DESTROYING ALL SUPERSEDED DOCUMENTS.

Figure C.3: Design sheet of the inner winding of the test transformer